Muon energy reconstruction in the Antarctic Muon And Neutrino Detector Array (AMANDA)

by

Predrag Miočinović

B.S. (Tennessee Technological University) 1996
M.A. (University of California at Berkeley) 1998

A dissertation submitted in partial satisfaction of the
requirements for the degree of
Doctor of Philosophy

in

Physics

in the

GRADUATE DIVISION
of the
UNIVERSITY of CALIFORNIA at BERKELEY

Committee in charge:

Professor P. Buford Price, Chair
Professor Hitoshi Murayama
Professor Donald C. Backer

Fall 2001

The dissertation of Predrag Miočinović is approved:

Chair Date

Date

Date

University of California at Berkeley

Fall 2001

Muon energy reconstruction in the Antarctic Muon And Neutrino Detector Array (AMANDA)

Abstract

Muon energy reconstruction in the
Antarctic Muon And Neutrino Detector Array
(AMANDA)

by

Predrag Miočinović
Doctor of Philosophy in Physics
University of California at Berkeley
Professor P. Buford Price, Chair

AMANDA is an optical Čerenkov detector designed for observation of high-energy neutrinos ($E \gtrsim 100$ GeV) and is located deep inside the South Polar ice cap. The neutrinos that undergo charged-current interaction in or near the detector can be observed by the telltale Čerenkov light generated by the resulting lepton and its secondaries. The presence of insoluble particulates in the ice increases the light scattering, which in turn increases the light containment inside the detector. This enhances the light collection efficiency, allowing for a calorimetry-like measurement of energy deposited by the neutrino-induced leptons.

In this work, I developed a probabilistic method for measuring the energy of non-

contained muons detected by AMANDA-B10 (1997 configuration). The knowledge of muon energy opens a large window of discovery since it helps to determine whether the parent neutrino has a terrestrial or extraterrestrial origin. The method is based on finding the muon energy that will most likely produce the observed detector response. The energy likelihood is generated by combining the average light-emission profiles of muons with different energies and the models of light distribution in ice and detector response to light. Event reconstruction results in an energy resolution of ~ 0.35 in $\log(E/\mathrm{GeV})$ over the 1 TeV – 1 PeV range. Below 1 TeV, the light produced is insufficient to reliably determine the muon energy, while above 1 PeV, the AMANDA-B10 response to energy saturates, due to the finite detector size and limitations in its hardware.

Stochastic variations in muon energy loss and photon propagation are the dominant sources that limit the reconstructed energy resolution. I showed that in such case, a Bayesian unfolding technique improves the reconstruction of the underlying muon energy spectrum. The unfolding also corrects for known systematic effects such as saturation, directional reconstruction bias, data "cleaning", and others.

My analysis of 1997 data shows that the energy spectrum of detected atmospheric neutrinos is consistent with its prediction. The atmospheric-neutrino energy spectrum supports the neutrino-flavor oscillation hypothesis as put forward by the Super-Kamiokande group. Based on the assumption of complete mixing ($\sin^2 2\theta = 1$) and using energy spectrum shape comparison, I find that the AMANDA preferred squared mass difference is $1.6 \cdot 10^{-4}\ \mathrm{eV}^2 \leq \Delta m^2 \leq 3.46 \cdot 10^{-3}\ \mathrm{eV}^2$.

The measurement of the atmospheric-muon energy spectrum shows a disagreement

with the prediction, possibly indicating an incomplete understanding of physics that is currently used to describe atmospheric muon flux.

The method presented here makes it possible to estimate energy an order of magnitude greater than was previously possible by AMANDA and it improves the resolution and accuracy over the currently used technique. It naturally scales for use in larger detectors like AMANDA-II and IceCube, and it can be easily extended for use in energy reconstruction of electron- and muon-neutrino contained events.

Professor P. Buford Price
Dissertation Committee Chair

To my parents,

for everything they did for me.

Thanks, Mom and Dad!

Mojim roditeljima,

za sve što su za mene učinili.

Hvala Mama i Tata!

Contents

List of Figures

List of Tables

Acknowledgements

The completion of this dissertation has been assisted by many people over the years, be it through their direct involvement with my work, education, and professional development or by coming in contact with broader aspects of my life. First and foremost I'd like to thank my Ph.D. advisor, Prof. Buford Price, for helping me along with support, suggestions, and invaluable discussions, and for showing me that very often it is the intangibles that really count.

For reaching this stage in my life as a physicist I have to thank Prof. Erna Šuštar for inspiring me to take this path, and Dr. Munther Hindi for insuring that I stick with it. Also, I would like to thank my thesis committee for making the final steps in completion of my degree painless ones.

This document would have never been possible without help, dedication, and hard work of numerous AMANDA collaborators (a.k.a. Amandroids). For useful discussions, clarification of mystical technicalities, and overall support I would in particular like to thank Tyce DeYoung, Stephan Hundertmark, Gary Hill, Christopher Wiebusch, Ole Streicher, Peter Nießen, Albrecht Karle, Carlos Pérez de los Heros, John Jacobsen, and especially Adam Bouchta. I shouldn't forget to mention our winter-overs who made sure we realize where in the world we stuck our detector; Steffen Richter, Robert Schwartz, and Darryn Schneider, among others.

Closer to the home front, I'd like to shout out thanks to my homies Ryan Bay and Kurt Woschnagg. It's been a real pleasure working with them and having fruitful discussions about physics, statistics, politics, women, existence of soul, and other assorted topics. Peace out! Thanks also go to all Price group members, Doug Lowder, Dima Chirkin, and others over the years, for their suggestions and contributions to my work.

Of course, none of this would be possible without the support of my loving family and dear friends. My parents, Ljiljana and Milan Miočinović, did an excellent job with their kids and I have learned a great deal about success in professional and personal life from them. A special thanks goes to Marie and Stanko Kulovich who were the only people able and willing to help me when I needed it the most. I wish you were here to see this finished.

Finally, a thanks goes out to *The Simpsons* for keeping me laughing throughout my higher education.

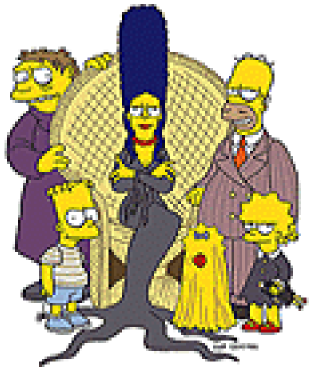

This research was supported by the following agencies:

U.S. National Science Foundation Office of Polar Programs

U.S. National Science Foundation Physics Division

University of Wisconsin Alumni Research Foundation

U.S. Department of Energy

U.S. National Energy Research Scientific Computing Center

Swedish Natural Science Research Council

Swedish Polar Research Secretariat

Knut and Alice Wallenberg Foundation (Sweden)

German Ministry of Education and Research.

Chapter 1

Introduction to AMANDA

"Oh, there's so much I don't know about astrophysics.
I wish I'd read that book by that wheelchair guy."
Homer Simpson, *The Simpsons,*
"Treehouse of Horror VI", **3F04**

The neutrino, the most elusive and ethereal particle in the Standard Model arsenal, could turn out to be the key that will unlock some of the deepest and darkest secrets of the Universe. With its existence postulated in 1930 by Pauli, it became and has remained one of the toughest experimental challenges to this day. An excellent review by Haxton and Holstein [1] summarizes the history and our present knowledge of neutrinos, with the exception of a possible detection of the tau neutrino [2].

1.1 Astrophysical information carriers

Observational astronomy and astrophysics rely solely on the detection of information carriers to determine any and all information about the objects of interest. At the present time, three types of information carriers are used: electromagnetic radiation, whose visible spectrum has been observed since antiquity; cosmic rays, since their detection in 1912 by Hess [3]; and neutrinos, since the pioneering work done on solar neutrinos by Davis in the mid 1960's [4]. Gravitational waves are another possible information carrier [5], although no direct gravitational wave detection has been reported so far.

Concentrating only on the very high-energy regime ($E > 10^{10}$ eV), the advantages and the disadvantages of these information carriers can be assessed (Figure 1.1).

Electromagnetic radiation

Photons are relatively easy to detect at any energy and they point directly back to their sources. This allows for simple source flux and energy spectrum measurements. However, photons can suffer from strong attenuation at their source and during propagation to the observer. An optically dense source obscures the flux and modifies the energy spectrum of high-energy photons generated at its center. Moreover, high-energy photons are affected by interactions with the microwave and infrared backgrounds (mostly through $\gamma\gamma \to e^+e^-$) as they traverse intergalactic distances. This limits the range of cosmological sources of interest that can be viewed by the highest energy photons (Figure 1.2) [6].

Cosmic rays

The detection of cosmic rays (energetic atomic nuclei) is more technically challenging than that of photons, but it is still straightforward. The terrestrial energy spectrum of cosmic rays has been well measured, but since they are charged they may have already interacted electromagnetically during their time spent in the interstellar medium. Their pointing accuracy is affected by the galactic magnetic field and their energy spectrum at

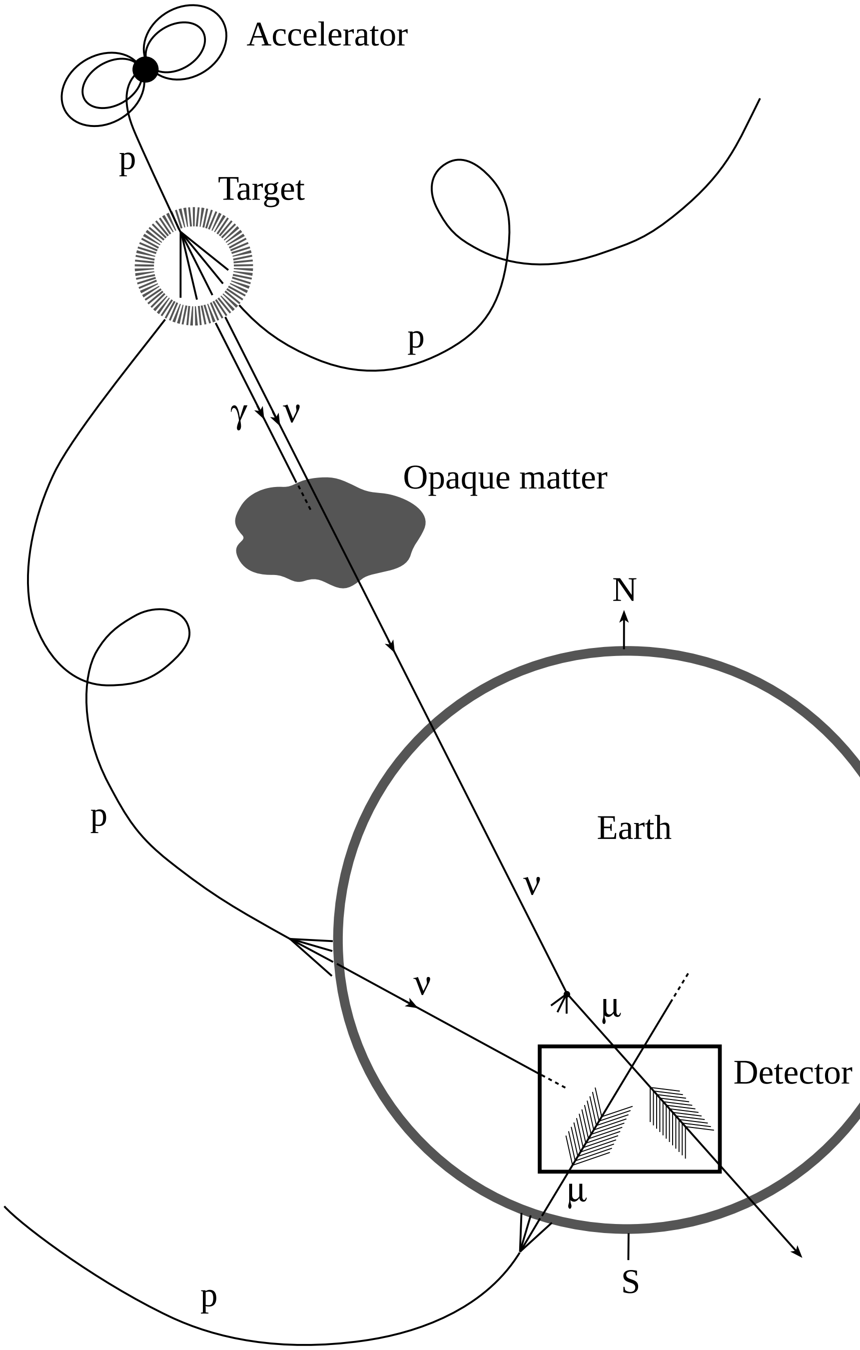

Figure 1.1: The comparison of high-energy information carriers.

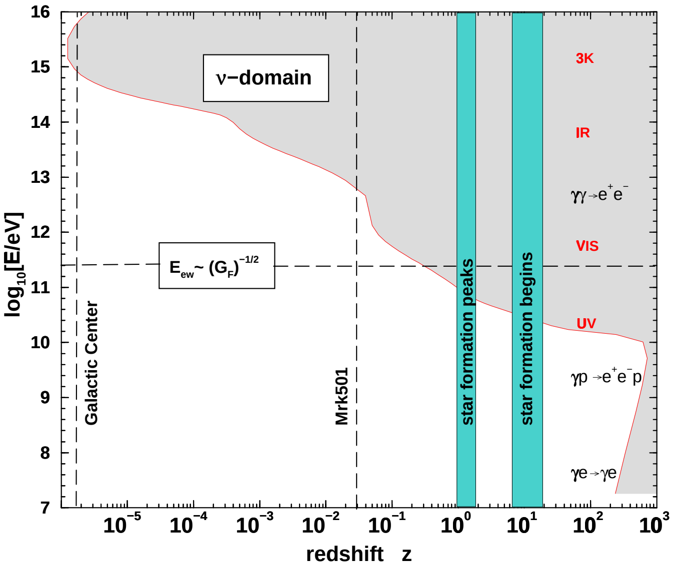

Figure 1.2: High-energy photon horizon; shaded area is invisible to gamma-ray astronomy. Figure taken from Ref. [7]

the source is distorted by ionization and other energy loss processes. Additionally, the highest-energy cosmic rays ($E \geq 5 \cdot 10^{19}$ eV) are expected to suffer strong attenuation due to interaction with the microwave background [8]. Thus, while cosmic rays carry some information about the energy distribution mechanisms at their sources, they cannot indicate directly where those sources are located.

Neutrinos

Neutrino directions are unaffected by magnetic fields, and their low interaction cross-section with matter ($\sigma_{\nu N} \sim G_F^2 E \sim 10^{-38} E$ cm^2 GeV^{-1} [9, 10]) makes them almost impervious to interactions at their source or during propagation to the observer. Thus, they reach us carrying the complete flux and energy spectrum information about their generation mechanism. Unfortunately, the same low cross-section that makes them ideal information carriers also makes them devilishly hard to detect. Very large detectors, long counting times, and sophisticated data analyses are therefore needed for measurements of high-energy extraterrestrial neutrino fluxes and spectra.

1.2 Neutrino astrophysics

The field of high-energy neutrino astrophysics was born with Greisen's 1960 review of cosmic ray showers [11] in which he discusses, among other things, a detector similar to the present prototypes of water Čerenkov detectors (BAIKAL [12], ANTARES [13], NESTOR [14]). Within a year, Markov and Zheleznykh [15] suggested the detection of neutrinos by means of upward or horizontally moving muons originating in the process

$$\nu_l(\overline{\nu}_l) + N \to l^{\mp} + \text{anything}, \tag{1.1}$$

where N is a nucleon of matter surrounding the detector and l is a charged lepton. At high energies, approximately half of the neutrino's energy will be carried away by the lepton. Due to relativistic boosting, their directions in the laboratory frame will be collinear with a mean deviation in the case of muon neutrino [16] of

$$\sqrt{\langle \theta^2_{\nu\mu} \rangle} \sim \sqrt{m_p/E_\nu}, \tag{1.2}$$

where m_p is the mass of a proton. For a 1 TeV muon neutrino this is about 1.75 degrees. As it propagates through the optically transparent detector medium, the highly energetic charged lepton will emit Čerenkov light [17] which can then be detected.

Due to the extraordinary technical challenges associated with high-energy neutrino detection (mainly in the form of construction and data collection technology), it was not until the 1990's that the first high-energy neutrino detectors or neutrino telescopes – BAIKAL [18] and AMANDA [19] – started collecting data, following the trail-blazing path of the now defunct DUMAND [20] experiment.

1.2.1 Neutrino production

Astrophysical neutrinos are produced in decays of mesons (predominately pions and kaons) which are in turn created in interactions of high-energy nucleons (N) with a target (A), which can be either matter or electromagnetic radiation;

$$\begin{array}{l} N + A \rightarrow \pi^{\pm} + X \\ \qquad\qquad\quad \hookrightarrow \mu^{\pm} + \nu_{\mu}(\overline{\nu}_{\mu}) \\ \qquad\qquad\qquad\quad \hookrightarrow e^{\pm} + \nu_{e}(\overline{\nu}_{e}) + \overline{\nu}_{\mu}(\nu_{\mu}). \end{array} \tag{1.3}$$

A similar decay chain describes kaon and heavier meson contributions to neutrino production. The observed neutrino oscillation [21] offers an additional possibility of $\nu_{\tau}(\overline{\nu}_{\tau})$ fluxes coming from the same sources even if the energies are insufficient to create tau leptons directly.

Based on observations (Figure 1.3), the high-energy differential cosmic ray flux produced in cosmic accelerators can be described by

$$\frac{d\phi_{\mathrm{cr}}}{dE} \propto E^{-(\gamma+1)}, \tag{1.4}$$

where γ depends on the acceleration mechanism, energy losses during the propagation, and the rate of cosmic-ray escape from the Galaxy. Depending on the kinematics of neutrino production at the same source, the neutrino flux is likely to have a harder energy spectrum, i.e., $d\phi_{\nu}/dE \propto E^{-(\alpha+1)}$, where $\alpha < \gamma$.

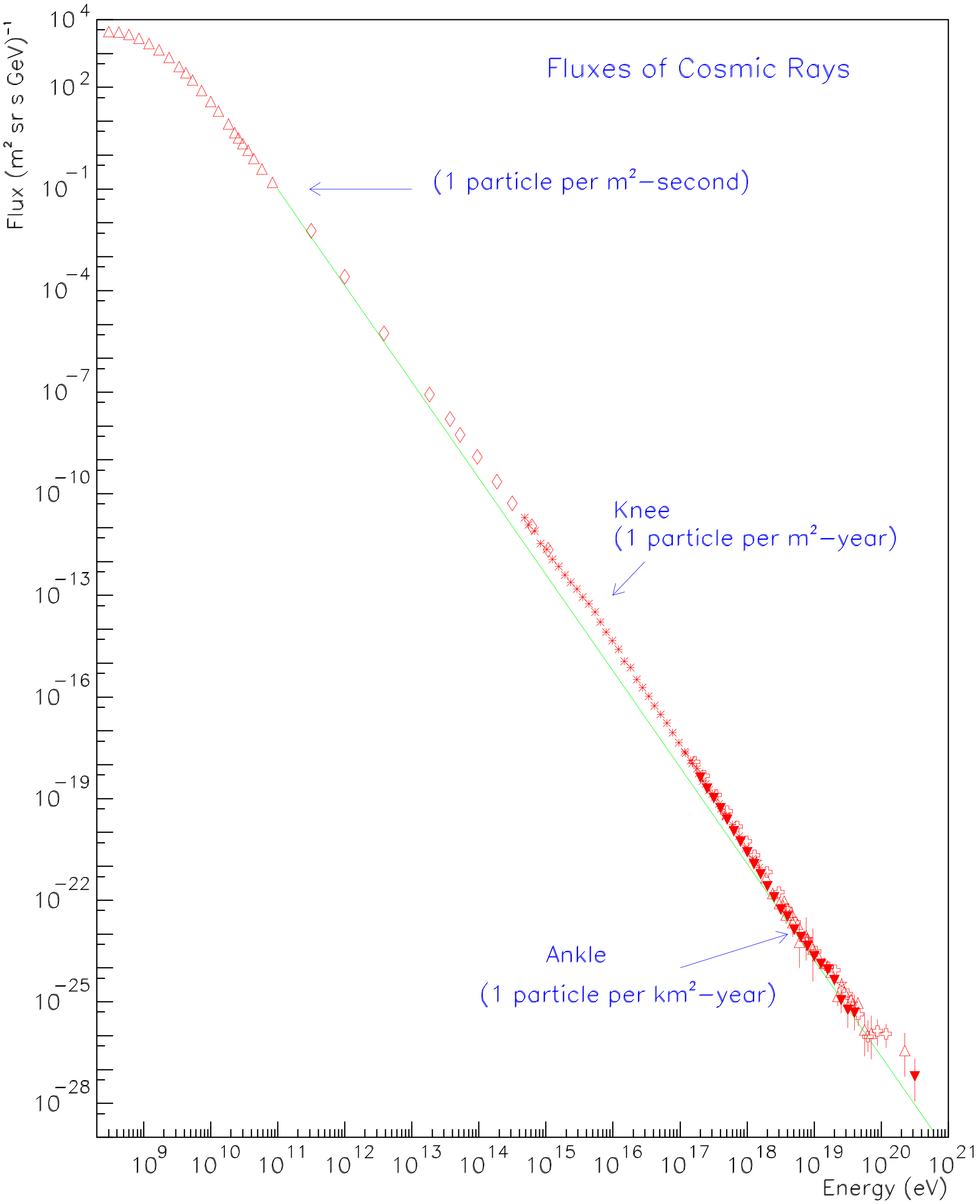

Figure 1.3: The measured flux of cosmic rays.

1.2.2 Neutrino background

Due to the lack of a neutrino calibration beam, the distinction between a background and a signal in the field of high-energy neutrino astrophysics is a blurred one. By taking the old quip that "one person's background is another person's signal" even one step further to "the signal during the calibration is a background during the analysis" creates a rather incestuous experimental situation. For example, the reported observation of atmospheric neutrinos by AMANDA [22], which proves that the operational principles of the detector are sound, will be regarded as a background once searches for extraterrestrial neutrino sources are reported [23].

The dominant contribution to the high-energy neutrino flux recorded by terrestrial detectors comes from cosmic ray interactions in the atmosphere. The observed energy spectrum of high-energy cosmic rays is characterized by $\gamma \sim 1.7$ (steepening to $\sim$2 above 1 PeV). Due to the size and the density of the atmosphere, the majority of mesons produced in cosmic ray showers interact before decaying, which steepens the neutrino spectrum to $\gamma \sim 2.7$.

There is also a small, yet possibly detectable contribution, coming from the prompt decay of charmed hadrons and mesons with the resulting spectrum closer to $\gamma \sim 1.7$ as is observed in cosmic ray flux [24]. New perturbative quantum chromodynamic calculations show that this prompt decay contribution to the atmospheric muon and neutrino fluxes becomes significant only for energies above 100 TeV (Figure 1.4).

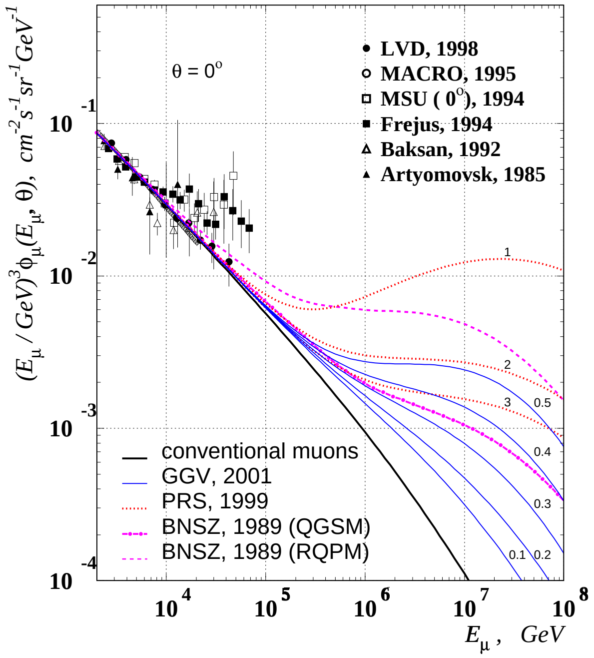

Figure 1.4: Vertical sea-level muon flux predictions. For measurement references see [25, 26]. The conventional muon flux curve does not include muons from prompt hadronic decay. The rest of the curves are calculated using various models for charm decay. For details see [27], from where the figure is taken.

1.2.3 Neutrino sources

Although the neutrino sky has no detected high-energy sources at the present time, the list of possibilities is very long. It ranges from the guaranteed galactic emissions by cosmic ray interactions in the Galactic Plane, to the prime suspects like AGNs and GRBs, and to exotic sources like topological defects (Figure 1.5) [7, 28].

While the cleanest signature for an observation of extraterrestrial neutrinos would be a point-like hot spot on a neutrino sky map, the present resolution of neutrino telescopes ($\sim 3.5°$ [23]) requires very bright neutrino sources for an indisputable detection. A complement to a point source signal is a diffuse extraterrestrial neutrino signal, whose detection

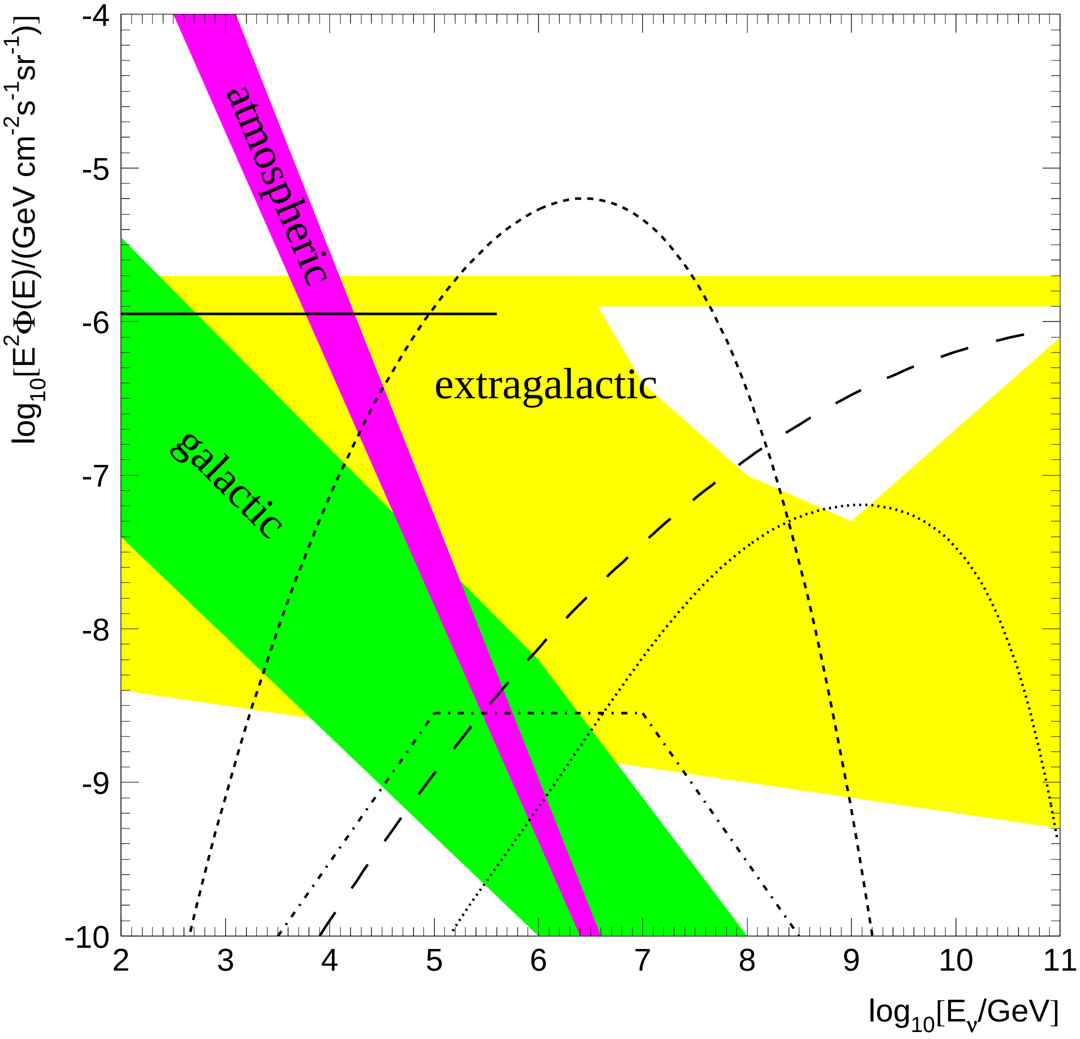

Figure 1.5: A sample of models predicting diffuse neutrino fluxes; blazars (solid), quasars (short dashed), ultra-high-energy cosmic ray sources (dotted), gamma-ray bursts (dot-dashed), and topological defects (long dashed). The terrestrial atmospheric background includes all zenith angles and prompt neutrinos from more conservative charm decay models. The galactic background includes all directions from the center (upper boundary) to the poles (lower boundary) of the Galactic Plane. The extra-galactic background consists of unresolved sources and cosmic ray interactions in intergalactic medium. Adapted from Ref. [7].

hinges on its separation from the atmospheric neutrino background. Since the majority of proposed extraterrestrial neutrino sources have energy spectra significantly harder than $E^{-3.7}$, the use of very-high-energy neutrinos opens a large window for discovery, even if the

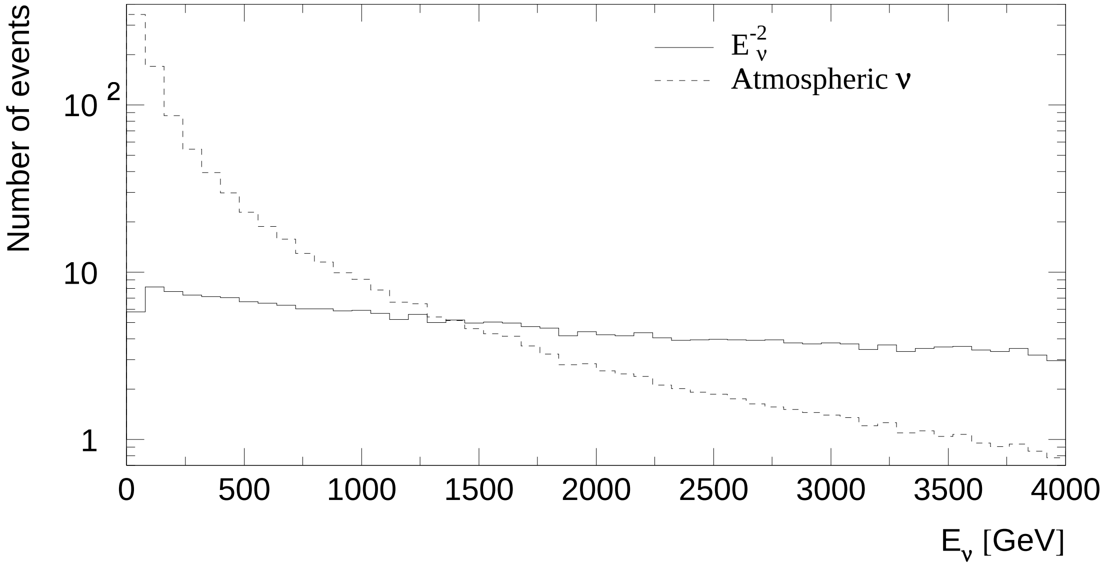

Figure 1.6: The energy distribution of neutrinos detected from a hypothetical source with E_ν^{-2} spectrum compared to an expected atmospheric neutrino background.

integrated source fluxes are orders of magnitude below the background (Figure 1.6).

1.3 The AMANDA telescope

The Antarctic Muon And Neutrino Detector Array (AMANDA) is a neutrino telescope built and operated at the geographic South Pole [29, 30]. It differs from other existing or proposed neutrino telescopes [12, 13, 14, 20, 31] in that its detection medium is ice, not water. Its location and environment offer both advantages and disadvantages over its competitors.

1.3.1 Ice as a detector medium

The glacial ice at the South Pole is the cleanest and the most transparent naturally occurring substance known to man. The concentration of impurities (including radioactive particles) ranges from ~200 to 500 ng/g [32]. Its purity and the low temperature ($\sim -20^\circ$C between depths of 1500–2000 m [33]) provide the most ideal environment on the Earth for operation of photomultiplier tubes. The noise rate of photomultipliers operated by AMANDA ranges from 0.3–1.3 kHz, and is completely dominated by the radioactivity inherent in the instrumentation.

The ice also offers a stable base of operations for the detector installation, operation, and maintenance. Even if routing signals through 2 km of cables frozen in ice might sound troublesome by accelerator physics standards, it is simpler than the case where tens of kilometers of submarine cable are needed to bring signals from water-based detectors to the shore.

It should be noted that the deep oceanic and lake waters with their longer light scattering lengths offer one advantage over ice. Scattering lengths in excess of 100 m ensure that the directional information of a particle will be almost completely preserved over the typical scale of a detector, assuming that the detector geometry and timing can be known accurately enough. On the other hand, stronger scattering and weaker absorption enhances light collection efficiency, making ice a better "calorimeter" than water and allowing for a more accurate measurement of energy.

1.3.2 History

AMANDA was conceived in 1988 by Halzen and Learned [34] and its construction has been carried out in stages over the entire decade of the 1990's. The construction pace has been dictated by the inaccessibility of the South Pole during austral winter and the technical challenges involved in building such an instrument.

To date, the AMANDA collaboration has deployed 761 optical modules on 24 strings, starting with the prototype string in the 1991–1992 season [35] and culminating with the completion of AMANDA-II during the 1999–2000 season (Figure 1.7) [36] . The work presented in this thesis will concentrate on the ten string stage – AMANDA-B10 – which was completed in the 1996–1997 season and operated during 1997 [37].

1.3.3 Instrumentation

AMANDA is a three-dimensional lattice of optical sensors embedded in a large volume of ice which serves as the detection medium. The lattice is made up of *optical modules* and calibration devices lined up on *strings*. An optical module (OM) consists of a photomultiplier tube (PMT) [38] protected by a spherical, high-pressure glass housing and passive electronics necessary to run the PMT and transmit its signals to the surface. A string consists of one or more electrical and optical cables to which the OMs are connected. The cables carry PMT signals to the surface, provide the power for operation, and offer mechanical stability during deployments. All signals are brought to the counting room, where they are amplified, discriminated and recorded.

1.3.4 Detection and reconstruction

The AMANDA data are collected with a simple-majority trigger logic that records the state of the array each time more than a predefined number of OMs record a signal within a specified time window. This produces a data sample that is highly dominated by down-going muons originating in cosmic ray showers in the atmosphere above the South Pole (Figure 1.8). Except at the very highest energies, neutrino-induced muons are outnumbered

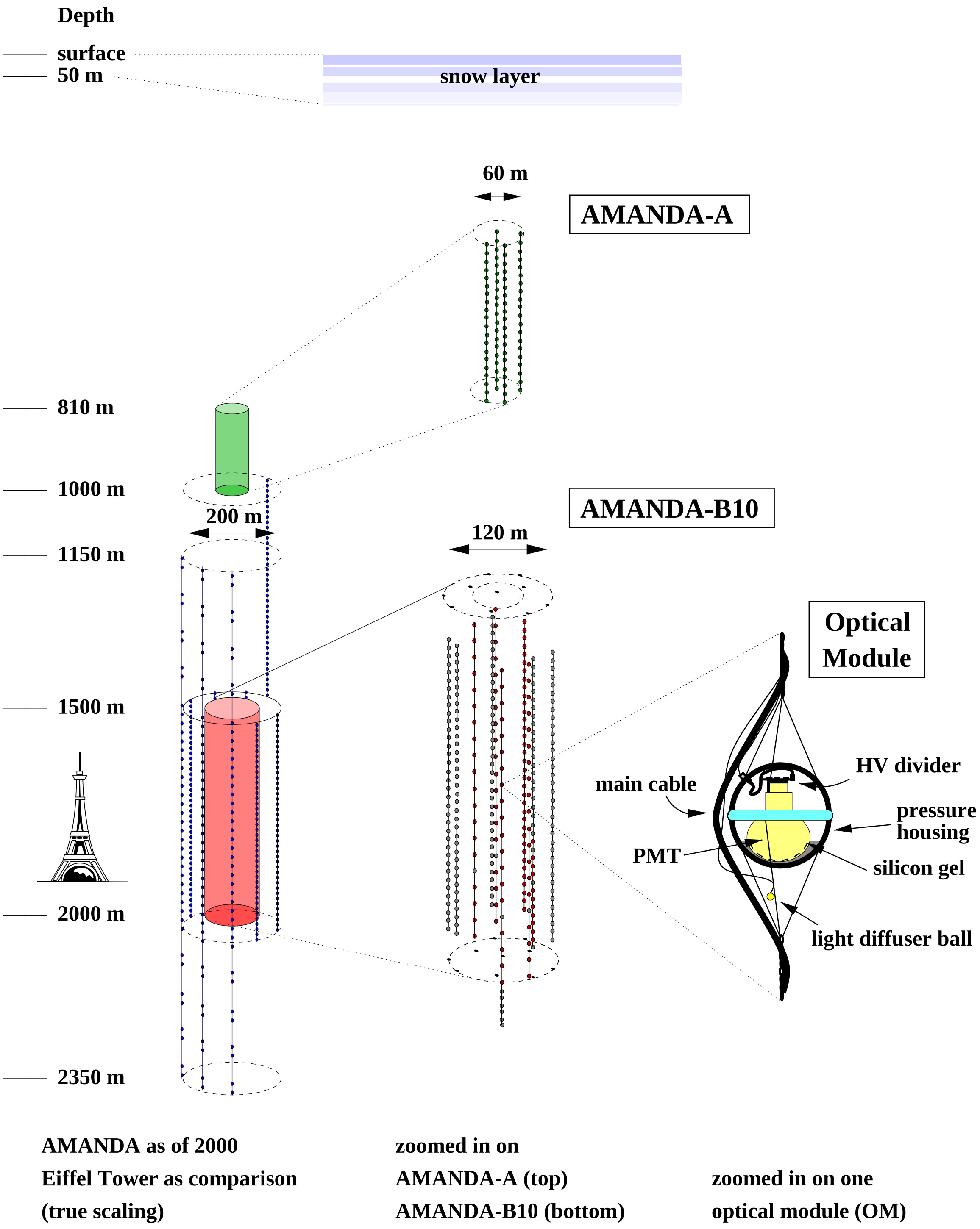

Figure 1.7: A schematic view of different AMANDA stages and components.

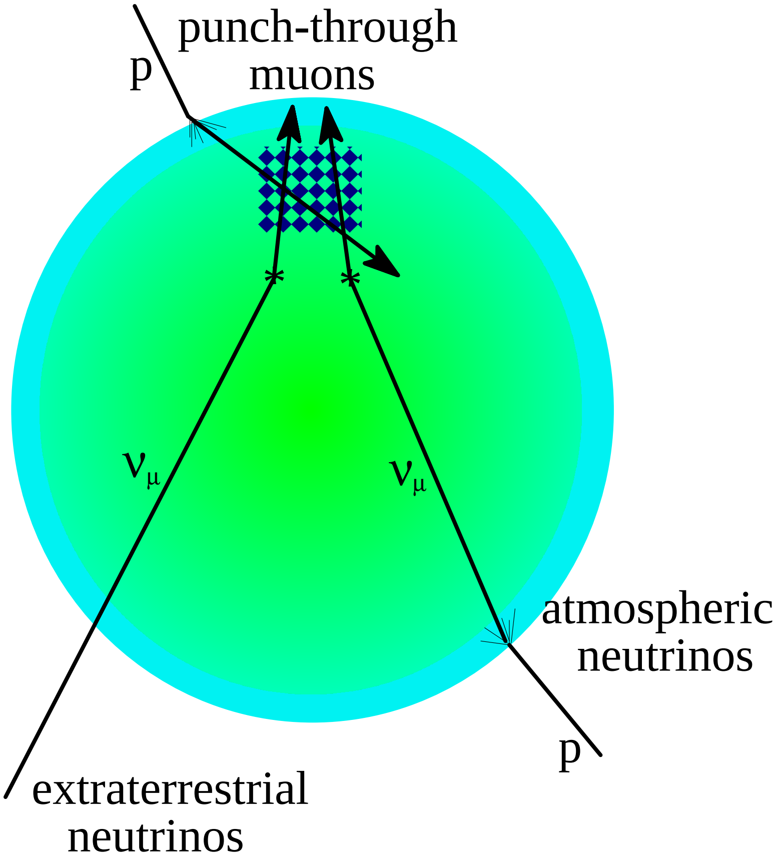

Figure 1.8: The schematic of three different origins of muons recorded by AMANDA.

by $\sim 10^6$ to 1, so the best way to distinguish them from cosmic ray shower muons is to use the Earth as a particle shield and only look for an upward-moving neutrino-induced signal. At the highest energies ($E \gtrsim 1$ PeV), the Earth becomes opaque even to neutrinos, so one is forced to look at the down-going extraterrestrial neutrino signal which should ride on a negligible cosmic ray induced background. High-energy electron-neutrino interactions and muon-neutrino neutral-current interactions can also trigger the detector, but this signal, which has a different topology within the detector, is treated separately from the neutrino-induced muon signal [39]. The trigger rate for electron-neutrinos and neutral-current muon-neutrino interactions is up to two orders of magnitude below the charged-current muon-neutrino trigger rate due to lower propagation ranges of electrons and hadrons.

To distinguish whether an up-going or a down-going muon triggered the array, the muon direction has to be reconstructed. The direction reconstruction is performed off-line, once the data have been recovered from the South Pole Station [40]. A muon direction is calculated based on the timing pattern recorded in the detector [41]. However, due to instrumentation uncertainties and the stochastic nature of light creation and detection within the detector, a large number of *fakes* is present after the reconstruction. A *fake* is an event that appears to have an up-going structure but has been generated by a down-going muon, an electron-neutrino-like cascade, an instrumental artifact, or a combination of these.

To remove the fakes from a data sample, the sample has to be "filtered". Filtering is an iterative data reduction process that aims to extract a pure up-going signal by comparing the data to a simulation. The resulting up-going signal sample can then be studied for its physical characteristics [42].

1.3.5 Muon energy reconstruction

Muon energy reconstruction in large high-energy neutrino telescopes has been previously attempted by several authors. Within the AMANDA collaboration, Wiebusch [43] has presented muon energy reconstruction based on counting how many OMs have recorded light, but without utilizing information about how many photons were recorded. This approach limits the dynamic range and resolution for higher energy muons ($E \gtrsim 100$ TeV). Several attempts have been made to extend this method, but without success.

For the BAIKAL collaboration, Streicher [44] developed a muon energy reconstruction technique which has been the inspiration for the work presented here. The method uses the detected number of photons to establish the total energy deposited by the passing muon. However, since BAIKAL is a water-based telescope with negligible light scattering, the muon generated photon flux predictions can be handled analytically, which is not possible in AMANDA.

In the next three chapters, the primary components of the muon energy reconstruction technique will be discussed: how muons lose energy and produce light; how light propagates in ice; and how light is detected by AMANDA. In the final three chapters, all this information will be pulled together into the muon energy reconstruction model, which will then be applied to data, and the results and the outlook will be discussed.

Chapter 2

Muon energy loss and light production

"...and these should give you the grounding you'll need in thermodynamics, hypermathematics and of course microcalifragalistics."
Professor John Frink, *The Simpsons,*
"The Wizard Of Evergreen Terrace", **5F21**

Muons constitute the primary signal and the primary background for any high-energy neutrino telescope. While ν_e and ν_μ fluxes can be expected to be of the same order in both the signal and the background, the larger muon range makes the muon effective area of a detector several orders of magnitude larger than that for electrons. Thus, the understanding of the muon signal within the detector is crucial, and it starts with the description of muon propagation and energy loss. This chapter reviews the physical processes involved in muon energy loss and describes how this information is incorporated into the muon energy reconstruction.

2.1 Muon interactions

The total muon energy loss can be broken down into several components: ionization, pair production, photo-nuclear interactions, bremsstrahlung, and knock-on electrons,

$$\frac{dE}{dx} = \left(\frac{dE}{dx}\right)_{\mathrm{I}} + \left(\frac{dE}{dx}\right)_{\mathrm{e^+e^-}} + \left(\frac{dE}{dx}\right)_{\mathrm{pn}} + \left(\frac{dE}{dx}\right)_{\gamma} + \left(\frac{dE}{dx}\right)_{\delta}. \tag{2.1}$$

Ionization is a quasi-continuous process, while the rest are stochastic in nature and dE/dx in their case should only be taken as some average energy loss given large enough dx.

Since ionization loss is almost constant above ~1 GeV and losses due to other mechanisms increase linearly with energy (see Section 2.1.6), the muon energy loss is customarily expressed as

$$\frac{dE}{dx} = a(E) + b(E) \cdot E, \tag{2.2}$$

where $a(E)$ stands for ionization loss and $b(E)$ for the rest. Furthermore, making an assumption that a and b are constant, the relation

$$\frac{dE}{dx} \approx a + b \cdot E, \tag{2.3}$$

can be used for a quick and relatively accurate energy loss calculation. For example, in ice $a = 0.25958(6)$ GeV mwe^{-1} and $b = 3.5709(3) \cdot 10^{-4}$ mwe^{-1} with the systematic error estimate of 3.7% [45, 46].

For purposes of muon energy reconstruction, the energy loss has to be known as accurately as possible, so the full stochastic nature of this energy loss should be considered. However, due to computational limitations, a lower limit has to be placed on the size of stochastic energy losses since their number increases rapidly for smaller energy transfer values. A working definition of the muon energy loss can be given by,

$$\left|\frac{dE}{dx}(E)\right| = \left[\frac{dE}{dx}(E)\right]_{\mathrm{CL}} + \left[\frac{dE}{dx}(E)\right]_{\mathrm{SL}}, \tag{2.4}$$

where CL and SL stand for continuous and stochastic losses, which are defined as,

$$\left[\frac{dE}{dx}(E)\right]_{\mathrm{CL}} = \frac{N_{\mathrm{A}}}{A_{\mathrm{eff}}}\rho E \sum_{j} \sum_{i=1}^{n} \left[k_i \int_{v_{\mathrm{min}}^{i,j}}^{v_{\mathrm{cut}}} \frac{d\sigma_i^j}{dv}(E,v) v dv \right], \tag{2.5}$$

$$\left[\frac{dE}{dx}(E)\right]_{\mathrm{SL}} = \frac{N_{\mathrm{A}}}{A_{\mathrm{eff}}}\rho E \sum_{j} \sum_{i=1}^{n} \left[k_i \int_{v_{\mathrm{cut}}}^{v_{\mathrm{max}}^{i,j}} \frac{d\sigma_i^j}{dv}(E,v) v dv \right], \tag{2.6}$$

$$A_{\mathrm{eff}} = \frac{1}{N_{\mathrm{tot}}} \sum_{i=1}^{n} (N_i A_i), \quad k_i = \frac{N_i}{N_{\mathrm{tot}}}.$$

In the above relations, $N_{\mathrm{A}} = 6.022 \cdot 10^{23}$ is Avogadro's number, ρ is the density of the medium, N_{tot} is the total number of atoms in a unit volume, n is the number of different atomic species, N_i is the number of atoms of the i^{th} species, and A_i is the atomic weight of the i^{th} species. The first sum loops over all energy loss processes, whose cross-section is given by $d\sigma/dv$ with $v = \Delta E/E$ as the fractional energy transfer. The range of possible energy transfers $[v_{\mathrm{min}}, v_{\mathrm{max}}]$ is constrained by the physics of each process, and v_{cut} limits the number of stochastic events to a manageable value.

2.1.1 Pair production

Electron pair production is the dominant energy loss process for muons with energies above ~1 TeV. In the presence of an atom, a muon may produce an electron-positron pair by transferring a small fraction of its energy and momentum to the nucleus or the atomic electron. The differential cross-section for this process has been parametrized by

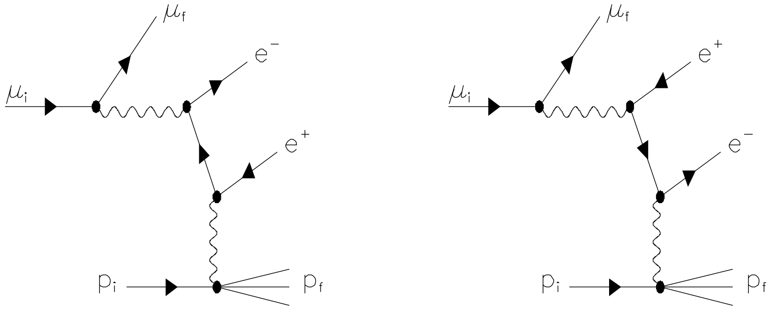

Figure 2.1: Feynman diagrams of pair production Φ_e term.

Kokoulin and Petrukhin [47] and the correction for the pair production on an atomic electron $\zeta(E,Z)$ has been parametrized in Ref. [48, 49];

$$\frac{d\sigma^{e^+e^-}}{dv}(E,v) = \alpha^2 \frac{2}{3\pi} r_e^2 Z \left(Z + \zeta(E,Z)\right) \frac{1-v}{v} \int\limits_{\rho} \left[\Phi_e + (m_e/m_\mu)^2\, \Phi_\mu\right] d\rho, \tag{2.7}$$

$$\Phi_e = \left\{\left[\left(2+\rho^2\right)(1+\beta) + \xi\left(3+\rho^2\right)\right] \ln\left(1+\tfrac{1}{\xi}\right) + \tfrac{1-\rho^2-\beta}{1+\xi} - \left(3+\rho^2\right)\right\} L_e, \tag{2.8}$$

$$\begin{aligned}\Phi_\mu = {} & \left\{\left[\left(1+\rho^2\right)\left(1+\tfrac{3}{2}\beta\right) - \tfrac{1}{\xi}\left(1-\rho^2\right)(1+2\beta)\right] \ln(1+\xi) + \tfrac{\xi\left(1-\rho^2-\beta\right)}{1+\xi}\right. \\ & \left. + \left(1-\rho^2\right)(1+2\beta)\right\} L_\mu, \end{aligned} \tag{2.9}$$

$$L_e = \ln\left[\frac{R\, Z^{-1/3}\sqrt{(1+\xi)\,(1+Y_e)}}{1+\frac{2m_e\sqrt{e}R\, Z^{-1/3}(1+\xi)(1+Y_e)}{E\, v(1-\rho^2)}}\right] - \frac{1}{2}\ln\left[1+\left(\frac{3}{2}\frac{m_e}{m_\mu}Z^{1/3}\right)^2 (1+\xi)\,(1+Y_e)\right], \tag{2.10}$$

$$L_\mu = \ln\left[\frac{\frac{2}{3}\frac{m_\mu}{m_e}R\, Z^{-2/3}}{1+\dfrac{2m_e\sqrt{e}R\, Z^{-1/3}\,(1+\xi)\,(1+Y_\mu)}{E\, v\,(1-\rho^2)}}\right], \tag{2.11}$$

$$Y_e = \frac{5-\rho^2+4\beta\left(1+\rho^2\right)}{2\,(1+3\beta)\ln(3+1/\xi) - \rho^2 - 2\beta\,(2-\rho^2)}, \tag{2.12}$$

$$Y_\mu = \frac{4+\rho^2+3\beta\left(1+\rho^2\right)}{\left(1+\rho^2\right)\left(\dfrac{3}{2}+2\beta\right)\ln(3+\xi)+1-\dfrac{3}{2}\rho^2}, \tag{2.13}$$

$$\beta = \frac{v^2}{2\,(1-v)}, \quad \xi = \left(\frac{m_\mu v}{2m_e}\right)^2 \frac{\left(1-\rho^2\right)}{(1-v)}.$$

Here $\rho = (E^+ - E^-)/(E^+ + E^-)$ describes the asymmetry of the energy distribution between an electron and a positron with limits,

$$\mid \rho \mid \leq \left(1 - \frac{6m_\mu^2}{E^2\,(1-v)}\right)\sqrt{1 - \frac{4m_e}{Ev}}. \tag{2.14}$$

R is a constant determined from the value of a radiation logarithm, Λ_Z, by [50],

$$R = \exp(\Lambda_Z) Z^{1/3} \tag{2.15}$$

A Hartrey-Fock calculation gives R=202.4 and 173.4 for hydrogen and oxygen, respectively. The correction factor for pair production on an atomic electron is parametrized as,

$$\zeta(E,Z) = \begin{cases} 0 & , E \leq 35m_\mu \\ \max\left\{0, \dfrac{0.073\ln\dfrac{E/m_\mu}{1+\gamma_1 Z^{2/3}E/m_\mu} - 0.26}{0.058\ln\dfrac{E/m_\mu}{1+\gamma_2 Z^{1/3}E/m_\mu} - 0.14}\right\} & , \text{otherwise} \end{cases} \tag{2.16}$$

$$\gamma_1 = \begin{cases} 4.4 \cdot 10^{-5} & , \text{for hydrogen} \\ 1.95 \cdot 10^{-5} & , \text{otherwise} \end{cases}$$

$$\gamma_2 = \begin{cases} 4.8 \cdot 10^{-5} & , \text{for hydrogen} \\ 5.30 \cdot 10^{-5} & , \text{otherwise} \end{cases}$$

The energy transfer in a pair production interaction is limited by

$$v_{\text{min}}^{\text{e}^+\text{e}^-} = \frac{4m_e}{E}, \quad v_{\text{max}}^{\text{e}^+\text{e}^-} = 1 - \frac{3}{4}\sqrt{e}\frac{m_\mu}{E}Z^{1/3}, \tag{2.17}$$

where e is the base of natural logarithm.

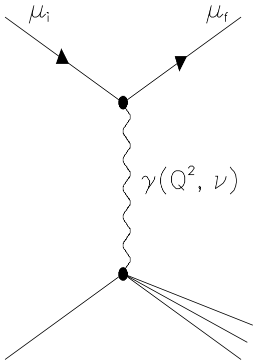

Figure 2.2: Feynman diagram of photo-nuclear interaction.

2.1.2 Photo-nuclear interactions

Photo-nuclear interaction is the process where a muon interacts via real or virtual photon with a hadron in the surrounding medium. The interaction cross-section has been parametrized by Bezrukov and Bugaev [51, 52] as,

$$\begin{aligned}\frac{d\sigma^{\mathrm{pn}}}{dv}(E,v) &= \frac{\alpha}{8\pi}A\sigma_{\gamma\mathrm{N}}\,v\left\{H(v)\ln\left(1+\frac{m_2^2}{t}\right)-\frac{2m_\mu^2}{t}\left[1-\frac{0.25m_2^2}{t}\ln\left(1+\frac{t}{m_2^2}\right)\right]\right. && (2.18)\\ &\left.+\,G(x)\left[H(v)\left(\ln\left(1+\frac{m_1^2}{t}\right)-\frac{m_1^2}{m_1^2+t}\right)-\frac{2m_\mu^2}{t}\left(1-\frac{0.25m_1^2}{m_1^2+t}\right)\right]\right\},\end{aligned}$$

$$H(v) = 1-\frac{2}{v}+\frac{2}{v^2}, \tag{2.19}$$

$$G(x) = \begin{cases}\frac{9}{x}\left[\frac{1}{2}+\frac{(1+x)e^{-x}-1}{x^2}\right] & , Z \neq 1\\ 3 & , Z = 1\end{cases} \tag{2.20}$$

$$x = 0.00282A^{1/3}\sigma_{\gamma\mathrm{N}}/(\mu\mathrm{b}), \quad t = \frac{m_\mu^2 v^2}{1-v}, \quad m_1^2 = 0.54\ \mathrm{GeV}^2, \quad m_2^2 = 1.80\ \mathrm{GeV}^2.$$

In the above, m_1^2 and m_2^2 are values related to quark masses. The total cross-section for nuclear absorption of a real photon of energy $\nu = vE$ can be parametrized as,

$$\sigma_{\gamma\mathrm{N}} = [114.3 + 1.647\ln^2(0.0213\,\nu)]\,\mu\mathrm{b}. \tag{2.21}$$

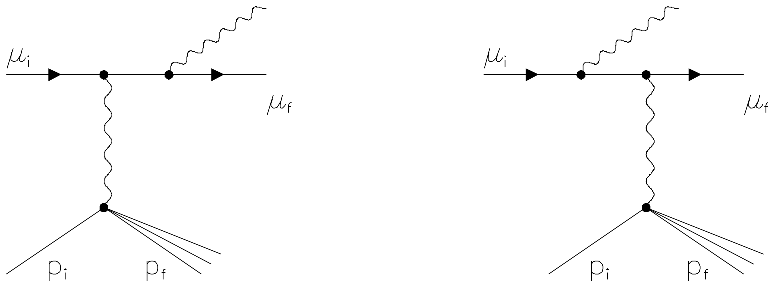

Figure 2.3: Feynman diagrams of bremsstrahlung on an atomic nucleus.

The parameterization is valid for $1 < \nu \lesssim 10^6$ GeV, but it is somewhat outdated with respect to the newest experimental data. Alternative $\sigma_{\gamma \mathrm{N}}$ parameterizations can be found in Ref. [53, 54]. The energy transfer limits should thus be taken as $v_{\mathrm{min}}^{\mathrm{pn}} = 1/E(\mathrm{GeV})$ and $v_{\mathrm{max}}^{\mathrm{pn}} = 1$. For more details on parameter x it is instructive to review Ref. [52].

2.1.3 Bremsstrahlung

As the name implies, bremsstrahlung (german: *braking radiation*) takes place when a muon experiences sudden deceleration accompanied by emission of high-energy photons. In the context of muon propagation in a dense medium, this deceleration is caused by electromagnetic interactions with surrounding atoms.

The total bremsstrahlung cross-section can be expressed as

$$\sigma^{\gamma} = \sigma^{\mathrm{el}} + \Delta\sigma_{\mathrm{a}}^{\mathrm{in}} + \Delta\sigma_{\mathrm{n}}^{\mathrm{in}}, \tag{2.22}$$

where σ^{el} is so-called “elastic” bremsstrahlung which leaves the impacted atom unchanged and $\Delta\sigma_{\mathrm{a,n}}^{\mathrm{in}}$ are contributions from additional “inelastic” processes which change the final atomic or nuclear state of the atom. The differential cross-section can be parametrized by

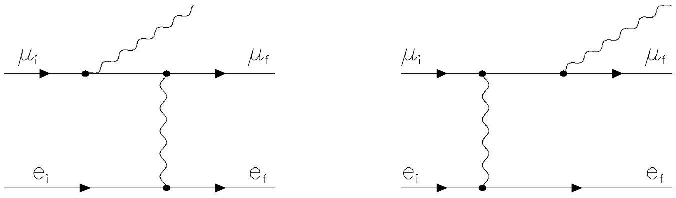

μ diagrams

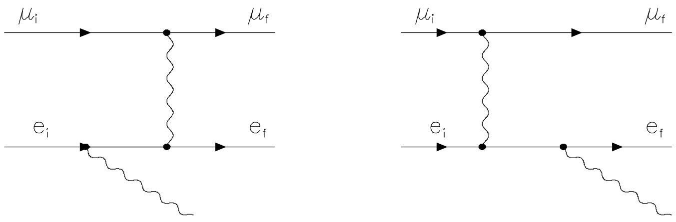

e diagrams

Figure 2.4: Feynman diagrams of bremsstrahlung on an atomic electron.

the prescription of Andreev, Bezurkov, and Bugaev [55],

$$\frac{d\sigma^{\gamma}}{dv}(E,v) = \left(2r_e Z\frac{m_e}{m_\mu}\right)^2 \frac{\alpha}{v}\left[\left(2-2v+v^2\right)\Psi_1\left(q_{\min},Z\right) - \frac{2}{3}\left(1-v\right)\Psi_2\left(q_{\min},Z\right)\right], \quad (2.23)$$

$$\Psi_{1,2}\left(q_{\min},Z\right) = \Psi^0_{1,2}\left(q_{\min},Z\right) - \Delta_{1,2}\left(Z\right), \quad (2.24)$$

$$\begin{aligned}
\Psi^0_1\left(q_{\min},Z\right) &= \frac{1}{2}\left(1+\ln\frac{m_\mu^2 a_1^2}{1+x_1^2}\right) - x_1\arctan\frac{1}{x_1} + \frac{1}{Z}\left[\frac{1}{2}\left(1+\ln\frac{m_\mu^2 a_2^2}{1+x_2^2}\right) - x_2\arctan\frac{1}{x_2}\right], \\
\Psi^0_2\left(q_{\min},Z\right) &= \frac{1}{2}\left(\frac{2}{3}+\ln\frac{m_\mu^2 a_1^2}{1+x_1^2}\right) + 2x_1^2\left(1 - x_1\arctan\frac{1}{x_1} + \frac{3}{4}\ln\frac{x_1^2}{1+x_1^2}\right) \quad (2.25) \\
&+ \frac{1}{Z}\left[\frac{1}{2}\left(\frac{2}{3}+\ln\frac{m_\mu^2 a_2^2}{1+x_2^2}\right) + 2x_2^2\left(1 - x_2\arctan\frac{1}{x_2} + \frac{3}{4}\ln\frac{x_2^2}{1+x_2^2}\right)\right],
\end{aligned}$$

$$\begin{aligned}
\Delta_1\left(Z\neq 1\right) &= \ln\frac{m_\mu}{q_c} + \frac{\zeta}{2}\ln\frac{\zeta+1}{\zeta-1}, \\
\Delta_2\left(Z\neq 1\right) &= \ln\frac{m_\mu}{q_c} + \frac{\zeta}{4}\left(3-\zeta^2\right)\ln\frac{\zeta+1}{\zeta-1} + \frac{2m_\mu^2}{q_c^2}, \quad (2.26) \\
\Delta_{1,2}\left(Z=1\right) &= 0,
\end{aligned}$$

$$q_{\min} = \frac{m_\mu^2 v}{2E(1-v)}, \quad x_i = a_i q_{\min},$$

$$a_1 = \frac{111.7}{Z^{1/3} m_e}, \quad a_2 = \frac{724.2}{Z^{2/3} m_e}, \quad \zeta = \sqrt{1 + \frac{4m_\mu^2}{q_c^2}}, \quad q_c = \frac{1.9 m_\mu}{Z^{1/3}}.$$

The screening correction constants coming from the radiation logarithm are contained within the parameters a_1 and a_2. The energy transfer limits are given by,

$$v_{\min}^{\gamma} = 0, \quad v_{\max}^{\gamma} = 1 - \frac{3}{4}\sqrt{e}\frac{m_\mu}{E} Z^{1/3}. \tag{2.27}$$

This formulation of the bremsstrahlung cross-section omits contributions from e-diagrams in which a photon is emitted by an electron that has been knocked out of an atom by the momentum recoil. Depending on the actual muon energy loss "cutoff" parameter v_{cut}, this contribution is added either to the stochastic knock-on electron cross-section or to the continuous ionization energy loss. The cross-section for e-diagrams is discussed by Kelner, Kokoulin and Petrukhin in the form of an additive correction to the elastic muon-electron scattering [56]. The actual result presented in Ref. [56] has some unwanted properties[†], so an approximate result suited for numerical calculations has been provided by S. R. Kelner [57],

$$\Delta_{\mathrm{e}\gamma}(E, v) = \frac{\alpha}{2\pi} \ln\left(1 + \frac{2vE}{m_e}\right)\left[\ln\left(\frac{4E^2(1-v)}{m_\mu^2}\right) - \ln\left(1 + \frac{2vE}{m_e}\right)\right]. \tag{2.28}$$

2.1.4 Knock-on electrons

The knock-on electron energy loss is technically a part of either the ionization or the inelastic bremsstrahlung cross-sections. However, since we are interested in separating

---

[†] It goes to $-\infty$ for large fractional energy transfer values

stochastic from continuous energy losses, we can combine all muon to electron energy transfers above some v_{cut} into a cross-section for occurrence of knock-on electrons (or δ-rays). It is given by,

$$\frac{d\sigma^{\delta}}{dv}(E,v) = 2\pi r_e^2 Z \frac{m_e}{\beta^2 E}\left(\frac{1}{v^2} - \frac{1}{v}\frac{\beta^2}{v_{\text{max}}^{\delta}} + \frac{1}{2}\right)(1 + \Delta_{\text{e}\gamma}(E,v)), \tag{2.29}$$

$$v_{\text{max}}^{\delta} = \frac{2m_e\beta^2 E}{m_e^2 + m_\mu^2 + 2m_e E}, \tag{2.30}$$

where v_{max}^{δ} is the maximum kinematically allowable energy transfer fraction and $\beta = p/E$ is the muon velocity with p as the muon momentum. The minimum energy transfer is given by, $v_{\text{min}}^{\delta} = \bar{I}/E$, where $\bar{I}$ is the mean ionization potential of the medium. In practice, this lower limit is negligible for high energy muons.

2.1.5 Ionization

Ionization occurs when a muon scatters elastically off the atomic electrons in a surrounding medium and knocks them out of their atoms. The energy lost by the muon in such way is given by the Bethe-Bloch equation [58]. Integrating over energy transfers below v_{cut}, gives

$$\begin{aligned}\left[\frac{dE}{dx}(E)\right]_{\text{BB}} &= \frac{N_{\text{A}}}{A_{\text{eff}}}\rho E \sum_{i=1}^{n}\left[k_i \int_{v_{\text{min}}^{\delta}}^{v_{\text{cut}}} \frac{d\sigma_i^{\text{BB}}}{dv}(E,v)v\,dv\right] \\ &= \frac{K}{\beta^2}\frac{Z_{\text{eff}}}{A_{\text{eff}}}\rho\left[\ln\left(\frac{v_{\text{up}}^{\delta}}{v_{\text{min}}^{\delta}}\right) + \frac{v_{\text{up}}^2}{4(1-\frac{m_\mu}{E})^2} - \beta^2\left(1 + \frac{v_{\text{up}}}{v_{\text{max}}^{\delta}}\right) - \delta\right],\end{aligned} \tag{2.31}$$

where K=0.1535 MeV g^{-1} cm^2, and $v_{\text{up}} \equiv \min(v_{\text{cut}}, v_{\text{max}}^{\delta})$. The last term, δ, is the density-effect correction which can be treated as [59],

$$\delta = \Theta(X - X_0)[4.6052X + a\Theta(X_1 - X)(X_1 - X)^m - C], \tag{2.32}$$

$$\Theta(x) = \begin{cases} 0 & , x \leq 0 \\ 1 & , x > 0 \end{cases}$$

$$X = \log \frac{p}{m_\mu}, \quad C = 2 \ln \left(\frac{\bar{I}}{28.816 \text{ eV}} \sqrt{\frac{A_{\text{eff}}}{\rho Z_{\text{eff}}}} \right) + 1,$$

$$a = 9.116 \cdot 10^{-2}, \quad m = 3.477, \quad X_0 = 0.24, \quad X_1 = 2.8004$$

where a, m, X_0, and X_1 are given for water.

As mentioned before, there is an additional contribution to the ionization energy loss from bremsstrahlung e-diagrams which can be expressed as,

$$\left[\frac{dE}{dx}(E)\right]_{\text{e}\gamma} = \frac{N_{\text{A}}}{A_{\text{eff}}} \rho E \sum_{i=1}^{n} \left[k_i \int_{v^\delta_{\text{min}}}^{v_{\text{cut}}} \frac{d\sigma_i^{\text{e}\gamma}}{dv}(E, v) v dv \right], \tag{2.33}$$

$$\frac{d\sigma_i^{\text{e}\gamma}}{dv}(E, v) = 2\pi r_e^2 Z \frac{m_e}{\beta^2 E} \left(\frac{1}{v^2} - \frac{1}{v} \frac{\beta^2}{v^\delta_{\text{max}}} + \frac{1}{2} \right) \Delta_{\text{e}\gamma}(E, v). \tag{2.34}$$

So, the total continuous ionization loss can be summarized as,

$$\left[\frac{dE}{dx}(E)\right]_I = \left[\frac{dE}{dx}(E)\right]_{\text{BB}} + \left[\frac{dE}{dx}(E)\right]_{\text{e}\gamma}. \tag{2.35}$$

2.1.6 Total energy loss

Combining the equations from preceding sections the total muon energy loss as a function of energy can be calculated (Figure 2.5). As pointed out earlier, this loss can only be taken as an average over large enough dx. The total loss is relatively constant over energies where ionization dominates ($E \lesssim 1$ TeV). Above several TeV, the energy loss is proportional to the muon energy.

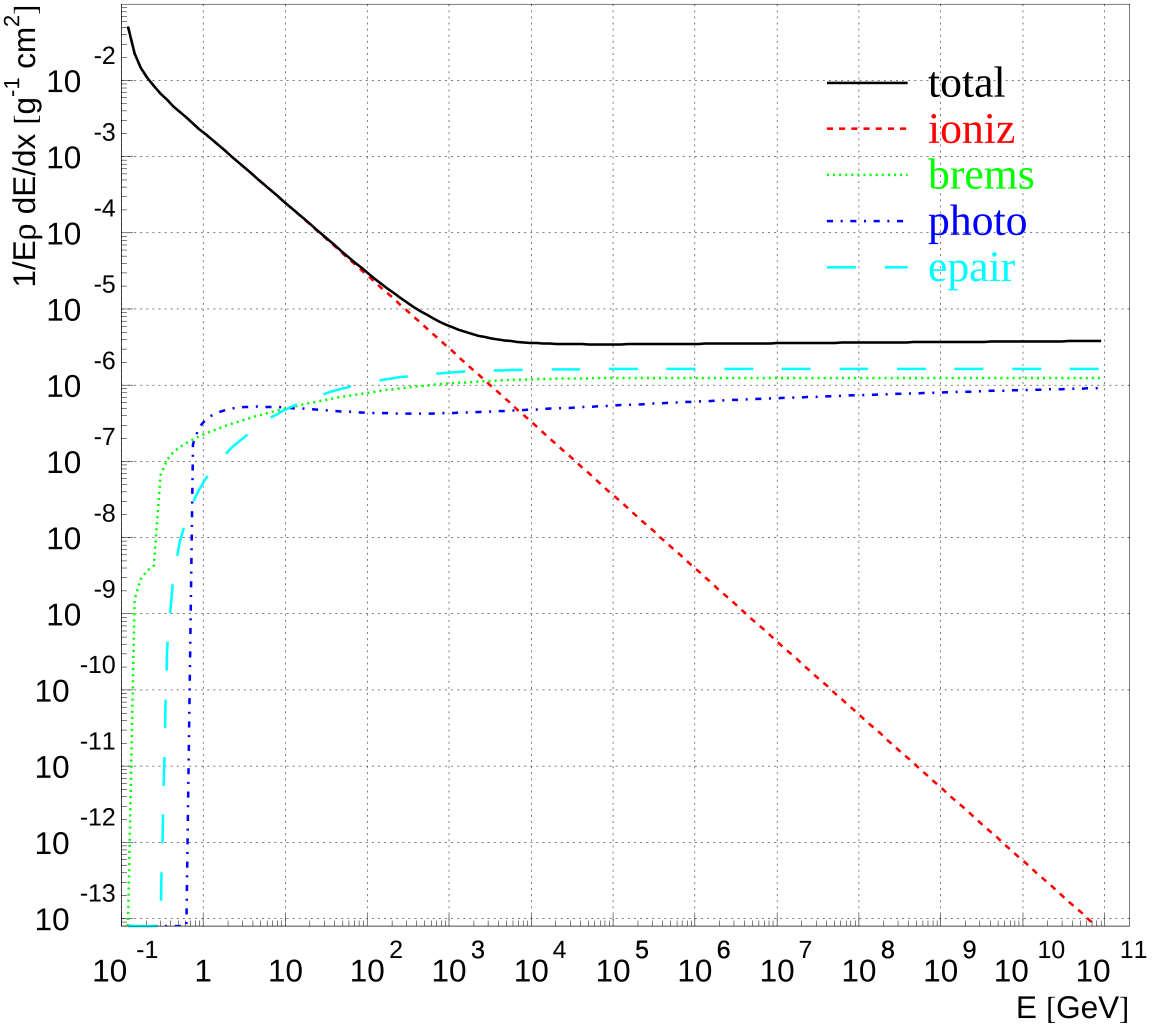

Figure 2.5: Energy loss as a function of muon energy, expressed in units of column density; ρ should be substituted by the density of the material the muon is traveling through. Various contributions are shown individually and knock-on electron losses were added to bremsstrahlung and ionization, as appropriate. Figure courtesy of D. Chirkin.

2.2 Average muon energy loss

The stochastic nature of the muon energy loss combined with the detector‘s small photocathode coverage presents the largest obstacle for muon energy reconstruction. Since it is impossible to tabulate all possible energy loss cases within the detector volume, the

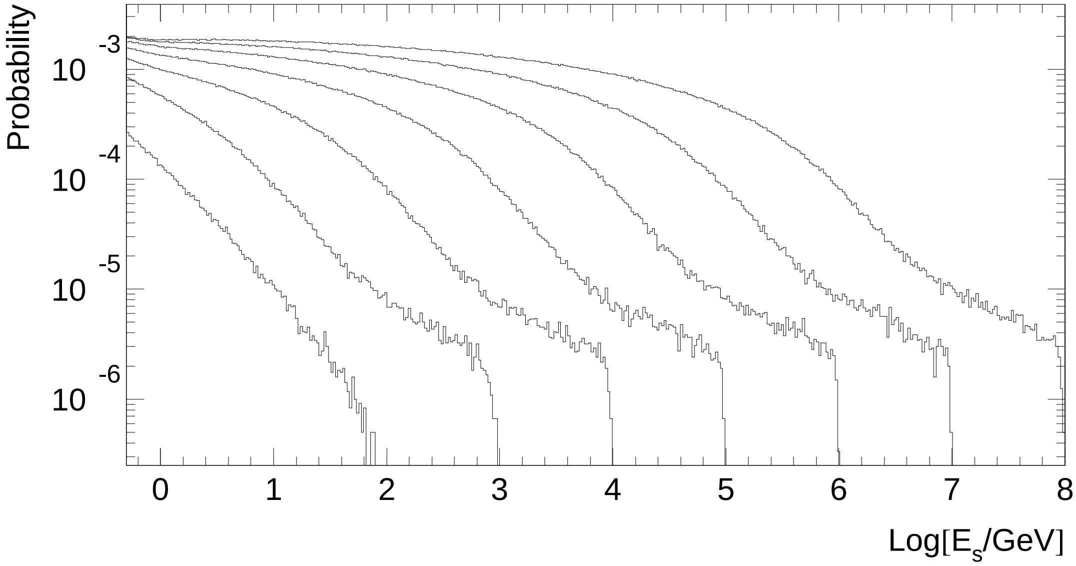

Figure 2.6: The probability that a muon will experience a stochastic energy loss $E_{\rm S}$ per unit step of 0.5 m in ice when traveling 600 m or until all of its energy is lost. Curves are shown for starting energies of 10^2, 10^3, 10^4, 10^5, 10^6, 10^7, and 10^8 GeV with the stochastic energy transfer cutoff set to $v_{\rm cut} = 0.5/E$ (GeV).

next best thing is to create an "average muon" approximation.

An average muon would lose energy at a constant rate proportional to the mean stochastic energy loss for a given *initial* muon energy E_0,

$$\left\langle \frac{dE}{dx}(E) \right\rangle = \left[\frac{dE}{dx}(E) \right]_{\rm CL} + \left\langle \frac{dE}{dx}(E_0) \right\rangle_{\rm SL} . \tag{2.36}$$

While it is possible to evaluate these energy loss components from Equations (2.7 – 2.35), it would be a very computationally intensive task. It is a lot faster to use a muon propagation program, such as `MMC` [45] or `MUM` [57], to generate several thousand muons per given initial energy and then add up stochastic energy loss per unit step. By renormalizing histograms generated in such way, one gets the probabilities that a muon would experience a stochastic energy loss of a certain magnitude within a given distance traveled (Figure 2.6). Since

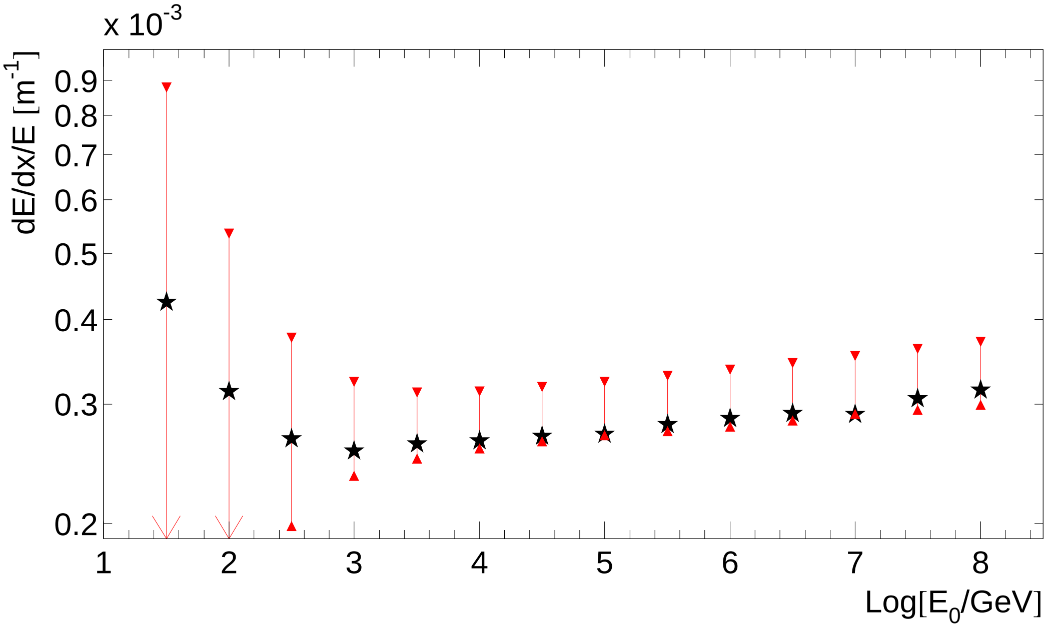

Figure 2.7: Comparison between the stochastic energy loss of an "average muon" per unit of path length (stars) and the actual energy loss of a muon at the beginning (inverted triangles) and the end (triangles) of the sampling path. The energy of a muon at the end of the sampling length has been calculated with an "average muon" energy loss rate approximation (Equation 2.36). For the two leftmost points, muons range out before leaving the 600 meter long sampling volume, so their final energy loss is zero.

the stochastic energy loss is averaged over the total sampling path length of the muon, the mean energy loss calculated by Equation (2.36) will underestimate the energy loss at the beginning of a muon path, whereas it will overestimate the loss towards the end of a path. This effect will be largest for lower energy muons ($E \lesssim 200$ GeV) which lose all or a significant fraction of their energy on the size scale of the sampling path length (Figure 2.7). The continuous losses of an average muon are well approximated by the relation

$$\left[\frac{dE}{dx}(E)\right]_{\text{CL}} = 0.208 + 3.62 \cdot 10^{-3} \ln(E) \text{ GeV m}^{-1}, \tag{2.37}$$

where v_{cut} was set to $0.5/E$ (GeV). The approximation is accurate to better than 0.5% for $E < 10$ TeV.

The "average muon" energy loss approximation is only valid over the scale length for which it has been been calculated[‡]. This can be checked by comparing the average muon range with the distribution of ranges calculated by the full stochastic model (Figure 2.8). The range estimate should be more accurate for lower energy muons which lose most or all of their energy over the sampling length. For higher energies, using Equation (2.36) to calculate an average muon range which is longer than the sampling length is, in essence, a linear extrapolation of a non-linear energy loss process. It will result in a gross underestimate of range as seen in Figure 2.8, bottom panels. However, this is acceptable, since one has no interest in a muon once it leaves the detector. For a 100 GeV muon, the numerical solution of the energy loss differential equations gives a mean range of 407 m which is in excellent agreement with the 396 m range given by an average muon approximation for the same starting energy.

2.3 Average muon light production

Since measuring the amount of emitted light is the only way to determine the energy of a muon passing through the detector[§], the light density profile created by an average muon of given energy needs to be generated. For this, two questions need to be answered: how much light is generated in the medium, and how is that light distributed in the vicinity of the generation point.

[‡] In this work 600 m is used, which corresponds to the scale size of AMANDA-B10.

[§] If the muon's path is fully contained within detector, the path length is also indicative of the energy.

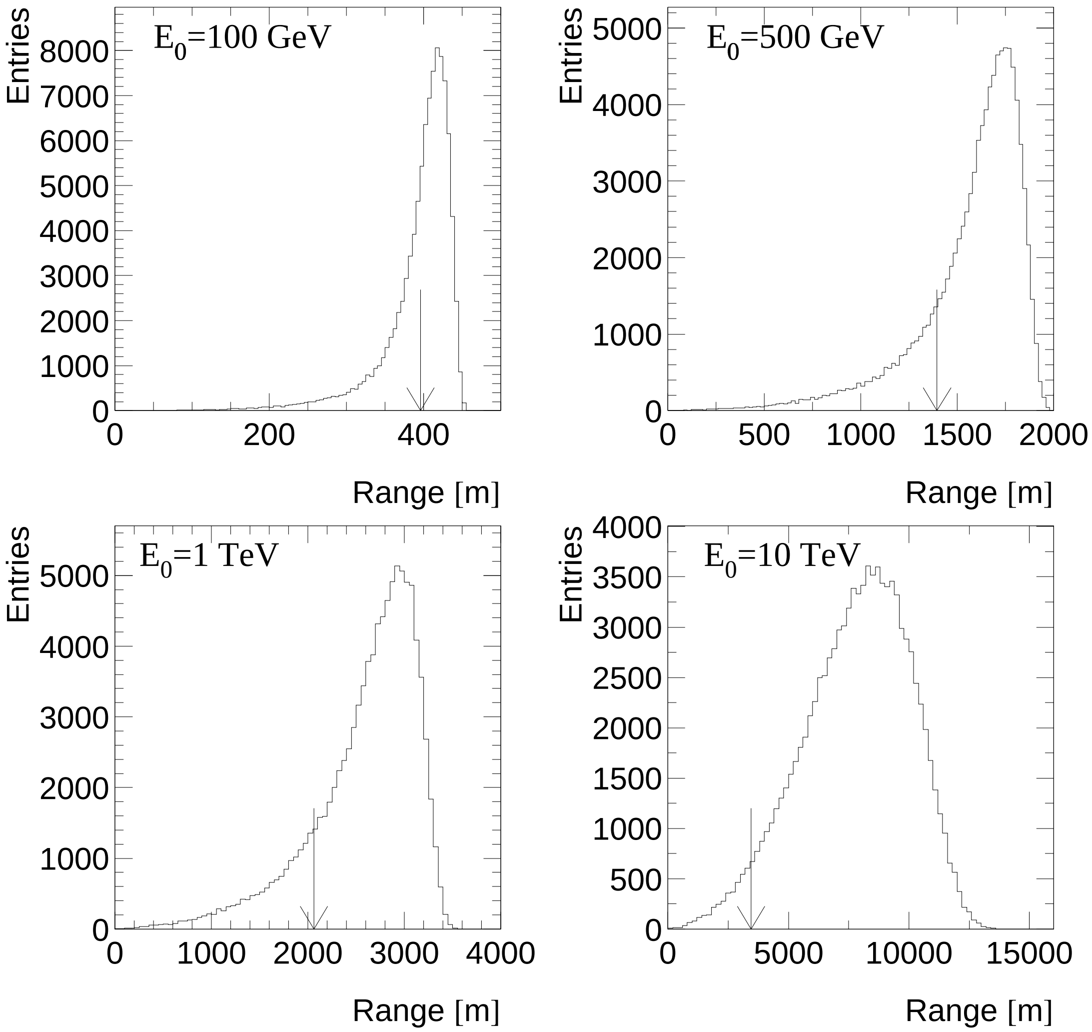

Figure 2.8: Comparison between the range of an "average muon" (arrow) and the actual range distribution of muons with the same starting energy. The 500 GeV average muon range has been interpolated.

2.3.1 Effective light emission from showers

In addition to the muon-generated Čerenkov radiation, all modes of stochastic muon energy loss in ice result in visible light production¶. The stochastic energy losses result in relativistic electromagnetic and hadronic showers which produce secondary Čerenkov

---

¶Incidentally, the muon energy loss due to Čerenkov radiation is almost negligible, ~24 keV/cm for $E > 1$ GeV [60], although it is accounted for by ionization cross-section.

radiation as characterized in section 3.2.4. The total amount of light emitted by any given shower can be calculated from the total track length of its constituent particles. The total track length has been parametrized with shower energy by Wiebusch [61] as

$$l(E) = E \cdot \begin{cases} 4.889 & \text{, for EM showers} \\ 4.076 & \text{, for hadronic showers} \end{cases} \quad [\mathrm{m/GeV}] \,. \tag{2.38}$$

However, since the assumption[‖] $\beta \approx 1$ will not hold true for all secondary particles, correction factors (calculated by Wiebusch) have to be applied to the total light output. For convenience, they can be applied to track length to produce effective shower-track length

$$l_{\text{eff}}(E) = l(E) \cdot \begin{cases} 0.894 & \text{, for EM showers} \\ 0.860 & \text{, for hadronic showers} \end{cases} \tag{2.39}$$

2.3.2 Effective light emission from muons

Considering that the working definition of continuous energy loss (Equation 2.5) also includes low energy showers (with $E_\mathrm{S}/E < v_\text{cut}$), there is an additional contribution to the overall light production. The light due to low energy showers can be added to the primary Čerenkov radiation emitted by the parent muon. The more complex angular emission pattern of showers (see Section 3.2.4) can be ignored since it is being treated as a correction to the muon light yield. Using a similar idea as in Equation (2.39), the effective muon track length used to calculate the amount of light emitted can be defined as [61],

$$l_{\text{eff}}(E) = l_0 \cdot (1.172 + 0.023 \ln(E)), \tag{2.40}$$

where E is the muon energy expressed in GeV and l_0 is the actual muon-track length.

[‖] as discussed in section 3.2.4

2.3.3 Combined light density profile

The light density profile surrounding any light generation point can be calculated with the photon tracking software (see Section 3.2). Then given the starting point, the direction, and the energy of a muon, photon flux density tables can be generated for all regions in the ice through which a muon will pass.

To calculate the average photon flux density surrounding an average muon, the Čerenkov light from muon and secondary showers needs to be added up,

$$\langle\Psi(l,d,\phi;z_0,\alpha,E_0)\rangle = \langle\Psi_\mu(l,d,\phi;z_0,\alpha,E_0)\rangle + \langle\Psi_{\mathrm{S}}(l,d,\phi;z_0,\alpha,E_0)\rangle\,. \tag{2.41}$$

The muon parameters (z_0,α,E_0) denote its starting vertical position relative to the detector, the zenith direction of its origin with respect to vertical, and its energy at the starting point. Within the muon frame, cylindrical coordinates (l,d,ϕ) are used: l is the distance along the muon path from the starting point, d is the perpendicular distance from the path, and ϕ is the azimuthal angle around the track (Figure 2.9). The average photon flux coming from shower and muon contributions is a sum over all track segments along the path of a muon. Each track segment should be small compared to the scale of the detector, so that light scattering washes out the granularity of sampling. Translating this summation into mathematical notation,

$$\begin{aligned}
\langle\Psi_\mu(l,d,\phi;z_0,\alpha,E_0)\rangle &= \sum_{l_{\mathrm{s}}=0}^{R}\Delta l_{\mathrm{s}} N_\mu(E(l_{\mathrm{s}},E_0))\psi_\mu(l-l_{\mathrm{s}},d,\phi;z_0,\alpha), && (2.42)\\
\langle\Psi_{\mathrm{S}}(l,d,\phi;z_0,\alpha,E_0)\rangle &= \sum_{l_{\mathrm{s}}=0}^{R}\Delta l_{\mathrm{s}}\sum_{T}\sum_{E_{\mathrm{S}}} P_{\mathrm{S}}(E_{\mathrm{S}},E_0)N_{\mathrm{S}}(E_{\mathrm{S}},T)\psi_{\mathrm{S}}^{T}(l-l_{\mathrm{s}},d,\phi;z_0,\alpha,E_{\mathrm{S}}), && (2.43)
\end{aligned}$$

where $\psi_{\mu,S}$ is the photon flux density normalized to a single photon emission and is calculated by the photon tracking program (see Section 3.2.2). The sum over all segments l_{s}

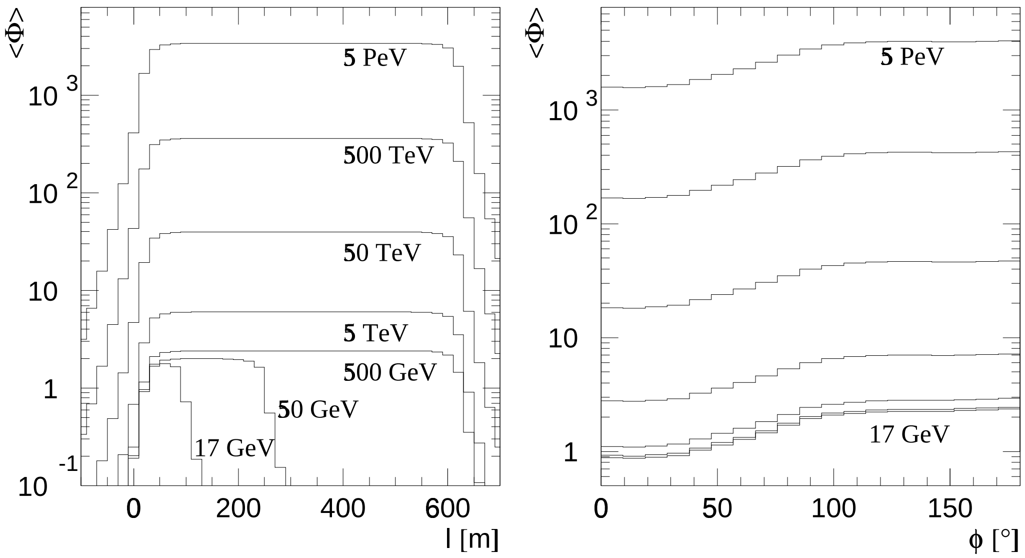

Figure 2.9: An example of muon light profiles. For fixed parameters $z_0 = 0$ m, $\alpha = 90°$, and $d = 9$ m, average photon fluxes generated by muons of various starting energies E_0 are plotted as functions of the distance l from the muon creation point (left, for $\phi = 45°$) and the angle ϕ with respect to an OM (right, for $l = 100$ m). In the left plot, low energy muons can be seen to decay before leaving the sampling volume. In the right plot, the up-down asymmetry of OM acceptance is seen.

runs from 0, where the muon energy was E_0, to some range R which is sufficient to enclose the detector volume. The segment length is expressed by Δl_{s}. The energy of a muon at any given segment, $E(l_{\mathrm{s}}, E_0)$, is calculated by,

$$E(l_{\mathrm{s}}, E_0) = E_0 - l_{\mathrm{s}} \left\langle \frac{dE}{dx}(E_0) \right\rangle_{\mathrm{SL}} - \Delta E_{\mathrm{CL}}(l_{\mathrm{s}}, E_0), \tag{2.44}$$

where $\Delta E_{\mathrm{CL}}(l_{\mathrm{s}}, E_0)$ is evaluated numerically from Equation (2.37)[**]. The sum T runs over secondary shower types (electromagnetic and hadronic), while E_{S} runs over all shower energies. The probability of shower occurrence is given by P_{S} with values taken from histograms such as the ones in Figure 2.6. Finally, the number of photons, $N_{\mu,\mathrm{S}}$, emitted

---

[**] A solution to Equation (2.37) does not exist in a closed form.

per unit length is calculated by

$$N_{\mu,\mathrm{S}}(E) = l_{\mathrm{eff}}(E) \cdot n_{\check{\mathrm{C}}}, \tag{2.45}$$

where $l_{\mathrm{eff}}(E)$ comes from either Equation (2.39) or (2.40) and $n_{\check{\mathrm{C}}}$ is calculated by integrating Equation (3.14) over the sensitivity range of an optical module (as discussed in the following chapters). In this work, the sensitivity range is taken to be 300–600 nm, resulting in $n_{\check{\mathrm{C}}} = 32440$ photons/m.

For simplicity and significant reduction in computing time, the time dependence of light density profiles will be ignored in this work. The timing also carries information which would be useful for energy reconstruction [62]. In the future, the time dimension should be added to light density tables used for muon energy reconstruction.

Chapter 3

Light propagation in glacial ice

"I see the light! It burns!"
Homer Simpson, *The Simpsons,*
"Faith Off", **BABF06**

Since large high-energy neutrino detectors typically instrument large volumes with a low density of optical detectors, the total effective collection area is very small compared to the geometrical surface area of the detector volume. In the case of AMANDA-B10, a quick estimate of the ratio of areas can be made

$$\frac{N_{\mathrm{OM}} \cdot A_{\mathrm{PMT}}}{2\pi \cdot R \cdot H} \approx \frac{302 \cdot 0.0284\mathrm{m}^2}{2\pi \cdot 60\,\mathrm{m} \cdot 500\,\mathrm{m}} = 4.5 \times 10^{-5}, \tag{3.1}$$

where A_{PMT} is the nominal collection area of a PMT, and R and H are the radius and the height of a cylindrical detector. This leads to a very low collection efficiency of light produced by muons and their secondaries. While the amount of light collected is sufficient to establish the particle trajectory, it is marginal when trying to reconstruct the particle energy. Because of this, it is crucial to understand the propagation of light in the detector medium as well as possible, so that the leading unknowns are due to the stochastic fluctuations in the amount of emitted light and not due to the uncertainties in the fraction of the light detected.

3.1 Optical properties of glacial ice

3.1.1 Impurities

The glacial ice covering the majority of the Antarctic continent is among the purest known substances. It has accumulated over thousands of years as a small annual snowfall. Under its own pressure, it undergoes a phase transition from compacted snow to fully dense ice at a depth of around 150 meters. The resulting ice at the AMANDA-B10 depths (1500–2000 m) is pristine H_2O except for trace impurities present in the Antarctic air that precipitated in snowflakes. The impurities present in the ice can be divided into four categories: acids, salts, minerals, and soot. All of them originated as wind-driven particulates from oceans and continents, and their respective concentrations can be considered as proxies for global climatic conditions at the time of their appearance. The actual paleoclimatological modeling will not be discussed here, but it should be stressed that the ratios of concentrations are roughly constant in time and location at Antarctic sites far from the ocean. This allows modeling of impurity concentrations at one location based on data gathered at another location more than 1000 km away, provided certain climatic properties are known (e.g., the snow accumulation rate at both locations and at upstream regions along the glacial flow direction) [32].

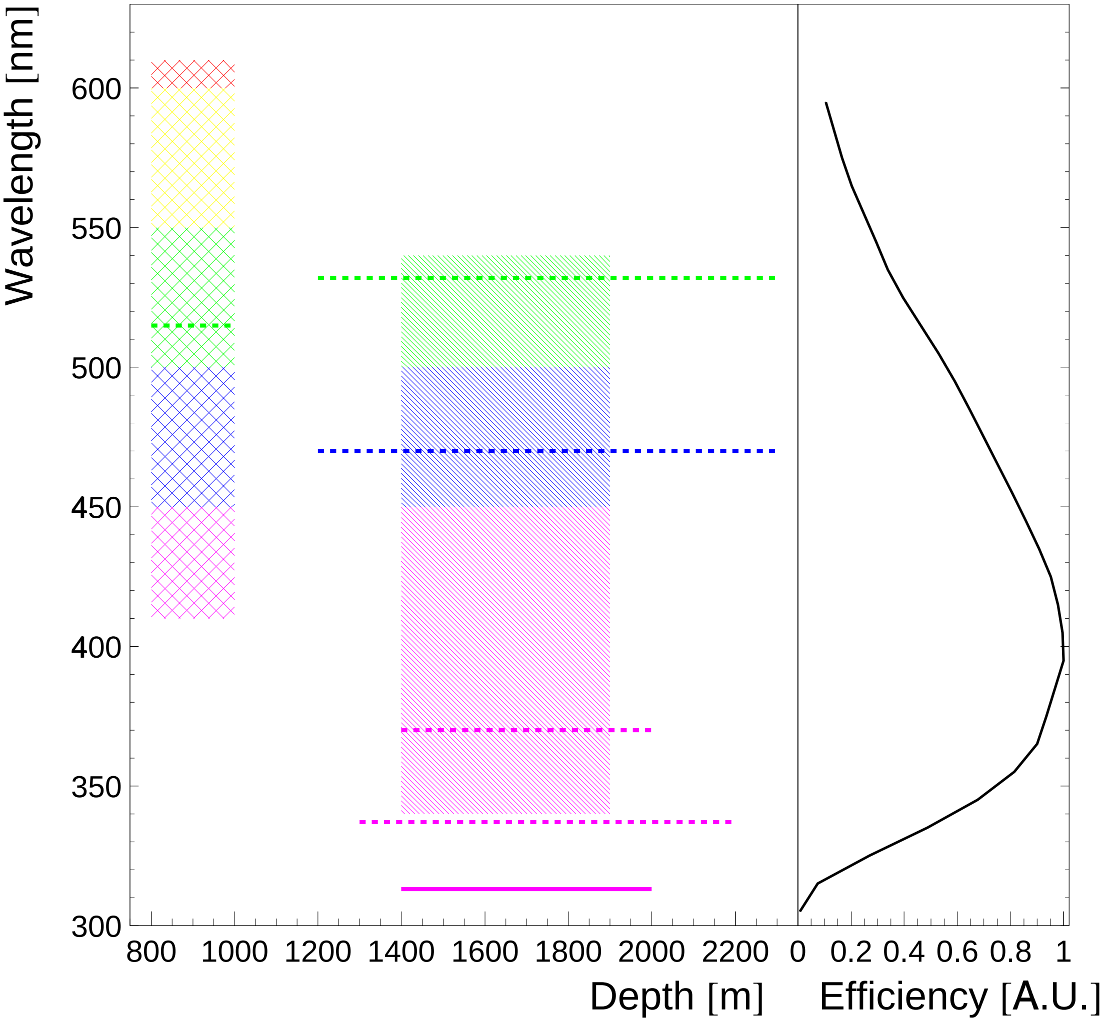

Figure 3.1: The wavelength and depth coverage of the optical properties data collected by AMANDA in the South Pole ice. The solid lines and areas have been investigated by DC sources, while the dashed lines and hashed areas have been investigated by pulsed sources. The curve on the right gives the nominal detection efficiency as a function of wavelength for an AMANDA OM, taking into account the transmission through the pressure vessel and the photocathode efficiency.

3.1.2 Measurements

The AMANDA collaboration has carried out multiple measurements of optical properties of the glacial ice at the South Pole between the 1994 and 2001 seasons [63, 64, 65, 66]. Various pulsed and DC light sources were used to emit light at depths of 0.8–1.0 km and

1.2–2.3 km. The light was then recorded by the same optical modules which are used for the muon detection. The sources emitted at wavelengths from 313 to 610 nm, which covers the complete spectral range of AMANDA optical modules (Figure 3.1).

3.1.3 Modeling

Light propagation in any medium is governed by the medium's propensity to scatter and absorb photons. Based on the measurements, an optical model of deep glacial ice has been developed by the AMANDA collaboration [67, 68]. The absorption is treated by the *3-component model*, which combines the lab measurements of absorption of light in the infrared and ultraviolet regions with the *in situ* measurements in the visible range. At wavelengths $\lambda < 210$ nm and $\lambda > 500$ nm, the absorption is dominated by the properties of pure ice, while in the intermediate range the impurities dominate. The most compact expression of the absorption dependence on wavelength can be written as [32],

$$a(\lambda) = A \cdot e^{-0.48175 \cdot \lambda} + B \cdot e^{-6700/\lambda} + C \cdot M_{\mathrm{dust}} \lambda^{-\kappa}, \tag{3.2}$$

where $a(\lambda)$ is the absorption coefficient, λ is in nanometers and M_{dust} is an experimentally determined mass concentration of impurities contributing to light absorption. The first exponential term is the so-called Urbach tail [69] which dominates at $\lambda < 210$ nm, the second exponential describes the rise of absorption in the red and infrared, while the third term dominates in the range $210 \leq \lambda \leq 500$ nm. The values M_{dust} and κ are determined from fits to data. To simplify the model and still get a good agreement with the measurements, κ can be set to ~ 1.1 for all depths, while allowing M_{dust} vary with depth [65]. The best fit proportionality constants are given by $A = 8 \times 10^{39}$ m^{-1} and $B = 8100$ m^{-1} [67], while

C is absorbed into M_{dust} during fitting of experimental data at different depths.

It is known that below ~1000 m depth, the light scattering is dominated by mineral impurities. However, the contributions from other types of impurities cannot be ignored. The available *in situ* measurements can not be used to distinguish between different types of scattering centers, so the best approach is to evaluate the effective scattering coefficient

$$b_{\text{eff}}(\lambda) \equiv b(\lambda)[1 - g(\lambda)], \tag{3.3}$$

where $b(\lambda)$ is a depth-dependent mean geometric scattering coefficient and $g(\lambda)$ is the mean cosine of the scattering angle.

3.1.4 Index of refraction

An often overlooked issue of the difference between the phase and the group velocity of light in water or ice was recently brought up by Kuzmichev [70]. He points out that the phase velocity and the corresponding index of refraction should be used for evaluating Čerenkov light emission angles and various transmission and scattering coefficients, while the group velocity should be used for measuring the time of light travel. There is a noticeable difference between phase and group indices of refraction for visible light in ice, and Price and Woschnagg parameterized these for AMANDA wavelengths of interest [71]. In the region from 0.3–0.6 μm, the phase index of refraction is given by,

$$n(\lambda) = 1.55749 - 1.57988\lambda + 3.99993\lambda^2 - 4.68271\lambda^3 + 2.09354\lambda^4 \tag{3.4}$$

while the group index of refraction can be expressed as,

$$\frac{n_g - n}{n} = \frac{\lambda}{n}\left|\frac{\mathrm{d}n}{\mathrm{d}\lambda}\right|, \tag{3.5}$$

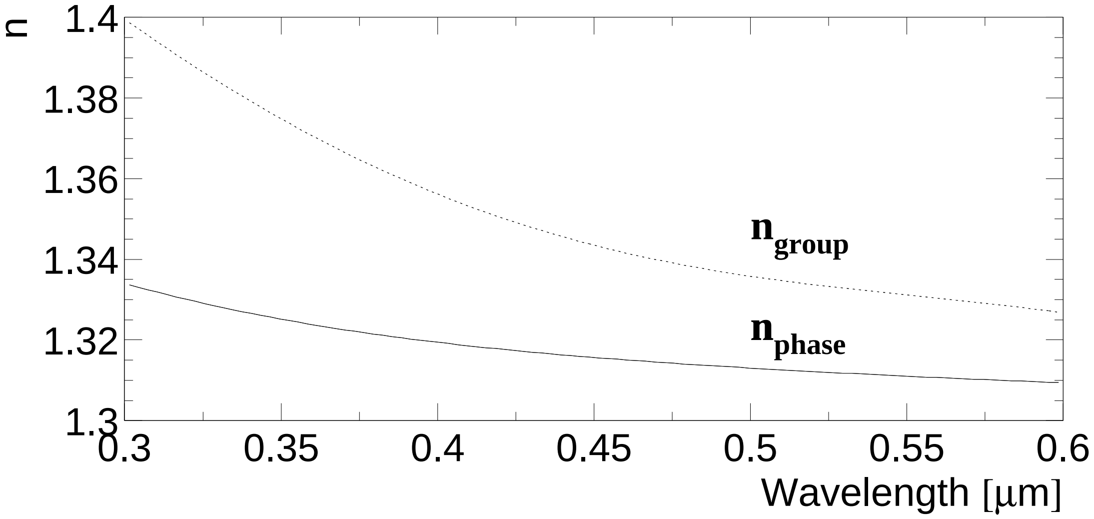

Figure 3.2: The phase and group indices of refraction for ice.

$$n_g(\lambda) = 1.55749 - 3.9993\lambda^2 + 9.36542\lambda^3 - 6.28062\lambda^4. \tag{3.6}$$

The indices of refraction for the region of interest are shown in Figure 3.2.

3.2 Photonics

`Photonics` is a software package developed by the author for tracking photons in media with vertically heterogenous optical properties [72]. The package consists of the main Monte Carlo tracking program that calculates photon density in the medium surrounding the light source and several additional programs for manipulation and display of photon density tables (see Appendix A). Within the `photonics` framework, different physical processes can be simulated by controlling the description of the propagation medium, the detection grid geometry, and the type of light-emitting source.

3.2.1 Photon tracking

The Monte Carlo program calculates photon densities by tracking the photons from their origin and assigning them survival probability weights at each point in space-time they pass through. The sum of all weights is the total photon density at any given point. The survival probability depends on the photon wavelength and on the optical properties of the medium along the photon trajectory;

$$w = \prod_{i=0}^{n} \exp\left(-\frac{l_i}{\lambda_{\mathrm{a}}(\lambda;i)}\right), \tag{3.7}$$

where l_i is the length of the photon path at step i and $\lambda_{\mathrm{a}}(\lambda;i)$ is the local absorption length for the photon of wavelength λ at step i.

The photon trajectory is determined by random scattering processes. As discussed in the previous section, various impurities contribute to the optical properties of the medium. In the Monte Carlo simulation, these contributions are combined and a mean scattering length is used to generate photon paths;

$$l_i = -\lambda_{\mathrm{s}}(\lambda;i)\log r, \qquad \lambda_{\mathrm{s}}(\lambda;i) \equiv b_{\mathrm{eff}}^{-1}(\lambda;i). \tag{3.8}$$

The length of the i^{th} step is determined by the local mean scattering length and a random number, r, in the range (0,1). The scattering angle calculation is based on the Henyey-Greenstein approximation to the Mie scattering function [68];

$$\frac{\mathrm{d}\sigma}{\mathrm{d}(\cos\theta)}(\lambda) = \frac{1-g(\lambda)^2}{(1+g(\lambda)^2-2g(\lambda)\cos\theta)^{\frac{3}{2}}}. \tag{3.9}$$

The mean scattering angle, $g(\lambda)$, can either be calculated from Mie theory or measured *in situ*. Since the precise measurement is very difficult and has not been performed, the value

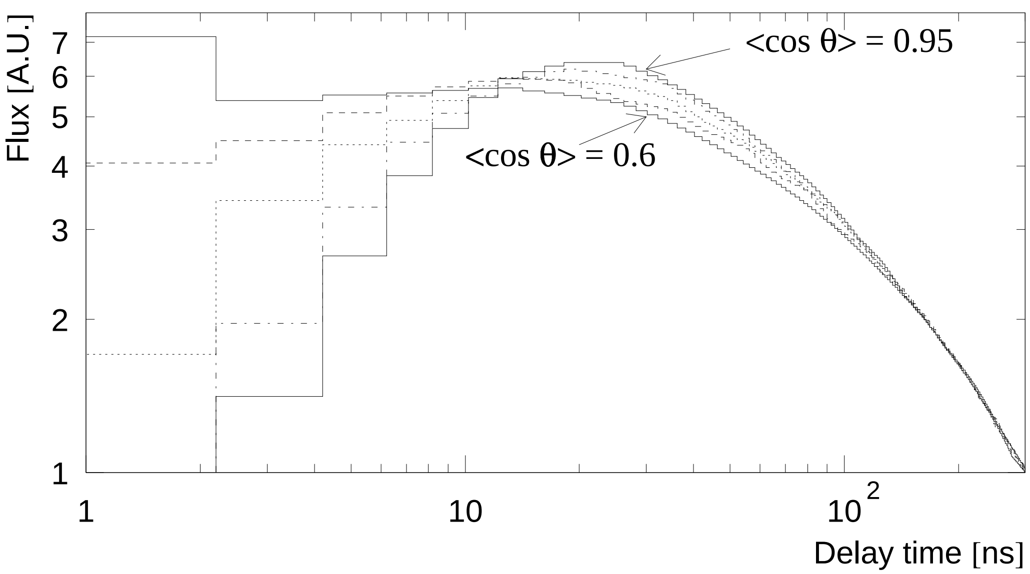

Figure 3.3: The photon flux density as a function of time for a fixed emitter-receiver pair separated by 40 m with $\langle\cos\theta\rangle$ values of 0.6, 0.7, 0.8, 0.9, and 0.95. The integrated fluxes vary by less than 2% and the peak flux arrival times vary up to ~10 ns. The excess in the first bin for $\langle\cos\theta\rangle$=0.60 is due to unscattered photons.

$g(\lambda) \approx \langle\cos\theta\rangle \approx 0.8 \pm 0.1$ can be taken as a good estimate for all depths [32]. It should be pointed out that the simulation results are very robust for changes of $\langle\cos\theta\rangle$ in the range [0.6,0.95] if one keeps the measured value of b_{eff} fixed [73]. This can be seen in Figure 3.3 where the timing profiles between the fixed source and receiver pair are plotted and only $\langle\cos\theta\rangle$ is varied. The photon flux peak position changes by ~10 ns between the extremes, which is on the order of the timing uncertainty of AMANDA PMTs, so any influence of $\langle\cos\theta\rangle$ on the timing is washed out in the data.

3.2.2 Flux calculation

To speed up the calculation, the photon tracking volume is subdivided into cells over which the photon density is averaged (Figure 3.4). The size of each cell can be varied to

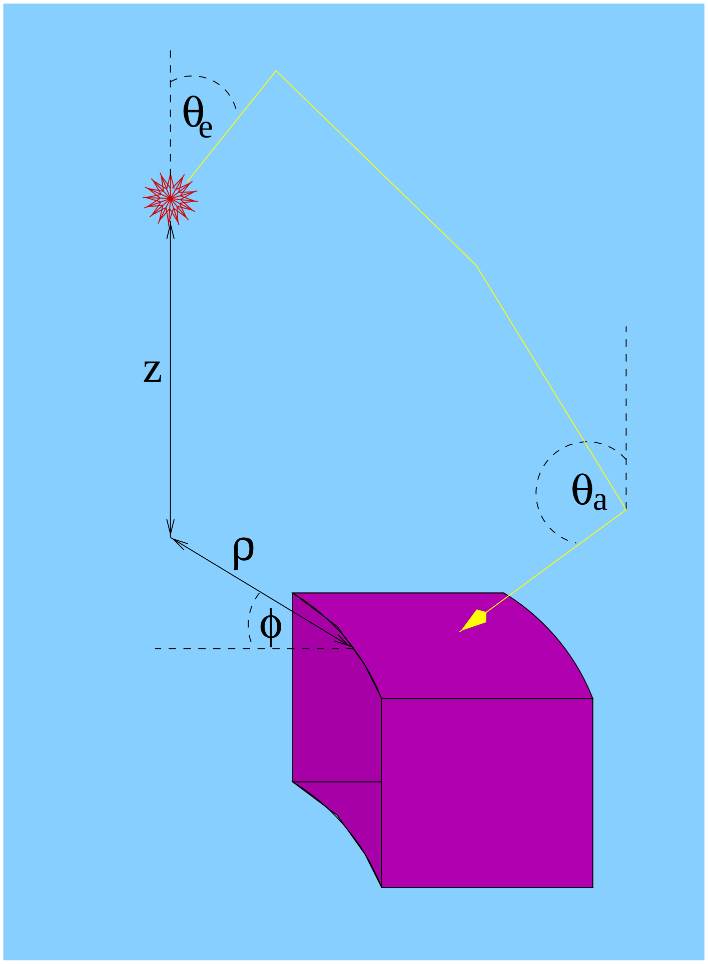

Figure 3.4: The unit cell geometry and a photon trajectory with variables which are used for the binning of photon flux data.

accommodate the necessary accuracy of a simulation. Within each cell, the photon direction and time of arrival are recorded, which makes it possible to calculate the directional time-dependent photon flux (Figure 3.5).

Depending on the tracking options used, the photon flux in a particular cell can be calculated by one of two methods; the area-crossing method (AC) or the volume-density

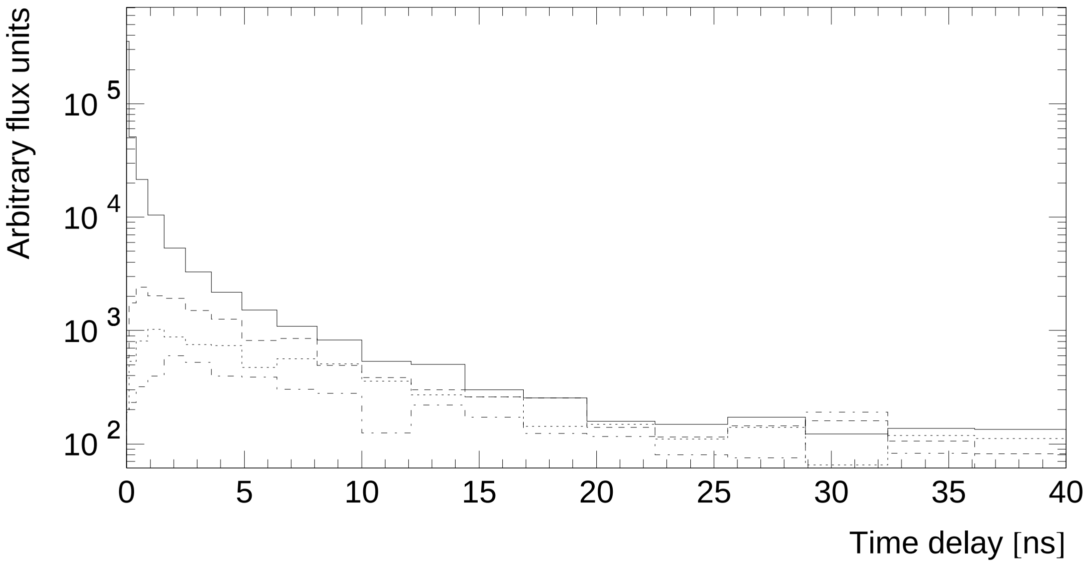

Figure 3.5: The photon flux coming from four different directions. An isotropic source is located 2 meters above an isotropic receiver. The four histograms represent fluxes for acceptance angles from 0° – 60° (solid), 60° – 90° (dashed), 90° – 120° (dotted), and 120° – 180° (dot-dashed) with respect to vertical.

method (VD). The respective flux calculation equations are

$$\psi_{\mathrm{AC}} = \frac{1}{N}\sum_{\gamma} w_{\gamma} A_{\perp}^{-1} = \sum_{\gamma} w_{\gamma} \left(\sum_{S} \widehat{\mathbf{d}}_{\gamma} \cdot \vec{\mathbf{A}}_{S} \right)^{-1}, \tag{3.10}$$

$$\psi_{\mathrm{VD}} = \frac{1}{N}\sum_{\gamma} w_{\gamma} \frac{\Delta s}{V}, \tag{3.11}$$

where N is the total number of simulated photons, w_{γ} is the survival weight of a photon, $A_{\perp}$ is the unit cell area projected perpendicular to the direction of a photon, V is the volume of the unit cell and Δs is the step size used for photon tracking. The sum S runs over unit cell surfaces with areas A_S which are projected onto the photon direction $\widehat{\mathbf{d}}_{\gamma}$. For the area-crossing method, the contribution of each photon to the total flux depends on the projected surface area of a unit cell as seen from the direction of photon arrival. In the volume-density method, each photon contributes to the photon density inside a unit cell, which is converted to the total flux by being multiplied by the distance Δs between photon position sampling points.

The calculation and recording of a photon contribution to the total flux in a unit cell is the most expensive computational step. To optimize for the speed and accuracy of flux calculation, one should consider the parameter $\Delta s/D_{\mathrm{uc}}$, the ratio of the step size to the scale dimension of a unit cell. If $\Delta s/D_{\mathrm{uc}} < 1$, the area-crossing method would be more efficient. Otherwise, the volume-density method should be used. Thus, the area-crossing method typically results in a faster code execution for large detection volumes with large unit cells, while the volume-density method is superior for small, dense unit cell configurations.

3.2.3 Ice models

The primary reason for the development of `photonics` was a need to study the variations in photon fluxes caused by optical inhomogeneities in the propagation medium, namely the ice. Experience has shown that the treatment of ice as a homogeneous medium is inadequate when trying to fully explain the data collected by AMANDA. With this goal in mind, at least two ice models needed to be developed for the use with `photonics`; a homogeneous ice model which would be used to compare the performance of `photonics` with the existing photon tracking software [74], and a heterogenous ice model representing the best understanding of the optical properties of South Pole ice.

An additional complication arises from the disturbances in the optical properties of the bulk ice introduced by the hot water drilling method used to install detector strings. However, since the overall volume of ice affected in such manner is small[†], this effect will

---

[†] A typical hole diameter of 60 cm is very small compared to the 120 m diameter of AMANDA-B10

be treated as a correction to bulk ice models.

Homogeneous Ice Model

To first order, the deep Antarctic glacial ice can be described as a homogeneous medium. The local scattering and absorption lengths can then be averaged out over all depths of interest. The optical properties were first extensively mapped at the wavelength of 532 nm[‡], so that can be taken as the reference point. From the relation

$$b_{\text{eff}}(\lambda) = \left(\frac{\lambda}{532}\right)^{-\alpha} b_{\text{eff}}(532), \tag{3.12}$$

the effective scattering coefficient can be calculated for any given wavelength. As described by He and Price [32], using Mie scattering theory with impurity concentrations measured at other Antarctic locations, α is calculated to be ~ 0.84 for the deep South Pole ice at depths of 1.4–2.1 km. The recent measurement of α agrees with this prediction [66].

From the 3-component model, the mean absorption coefficient is given by Equation (3.2), where CM_{dust} is an empirically determined value related to the impurity concentration and can be approximated by $CM_{\text{dust}} = 158 \cdot b_{\text{eff}}(532) - 0.634$.

Based on the *in situ* measurements, $b_{\text{eff}}(532) = 1/24\ \text{m}^{-1}$ with $\langle\cos\theta\rangle = 0.8$ can be taken as canonical values (Figure 3.7).

The Standard South Pole Ice Model

At the time of writing, the best available description of the optical properties of the South Pole ice is given by Woschnagg [65]. Taking $b_{\text{eff}}(532)$ *vs* depth data, effective scattering coefficients can be interpolated in 10-meter steps (Figure 3.6). Using Equations

---

[‡] Green light from a frequency-doubled YAG laser

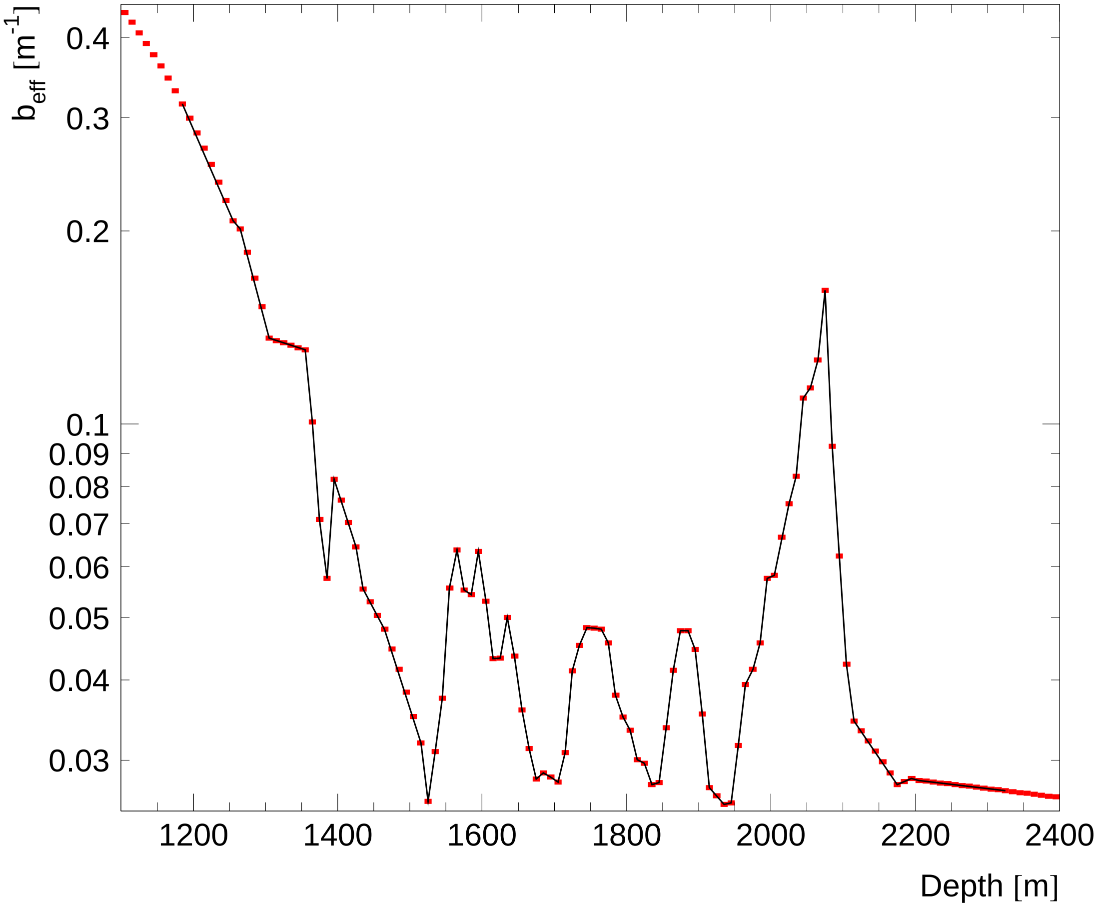

Figure 3.6: The dashes, each 10 m wide, are the nominal values of $b_{\text{eff}}(532)$ used in the Standard South Pole Ice Model. The solid curve connects the measured values of the effective scattering coefficient and it is only intended to guide the eye.

(3.2) and (3.12), the local optical properties can be described in each 10-meter thick layer of ice. An example of resulting values is shown in Figure 3.7 where the effective absorption coefficients and scattering lengths for two depths from the Standard South Pole Ice Model and for the Homogeneous Ice Model are plotted as functions of wavelength.

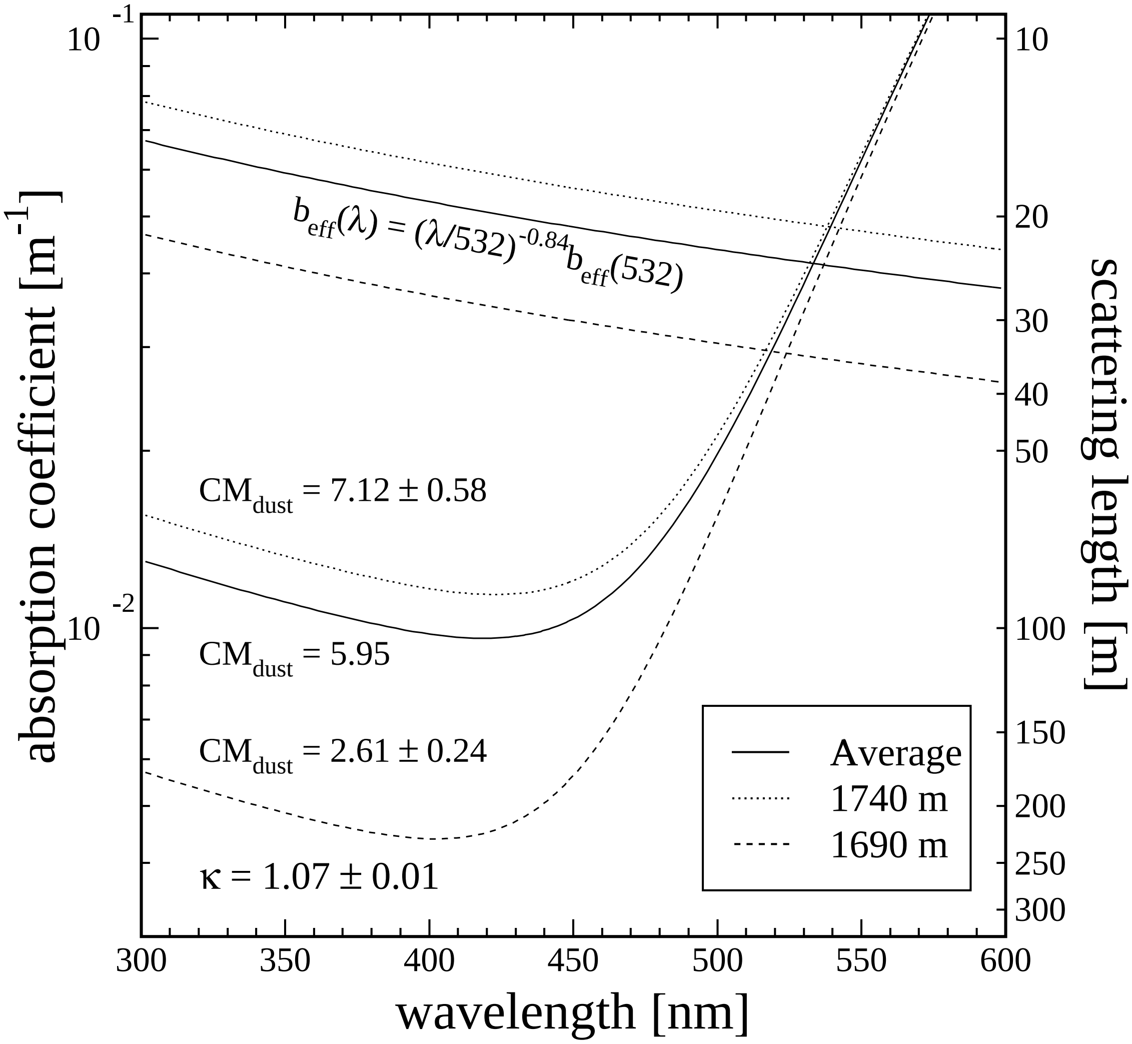

Figure 3.7: The wavelength dependences of scattering and absorption coefficients are plotted for two depths from the Standard South Pole Ice Model and for the average optical properties used in the Homogeneous Ice Model.

Hole ice model

The hot water drilling introduces variations in optical properties for a small region of ice surrounding the optical modules. The melting and subsequent refreezing of ice creates a population of microscopic air bubbles frozen inside the ice matrix. Air bubbles also occur naturally in the glacial ice as air trapped between snowflakes which eventually form ice.

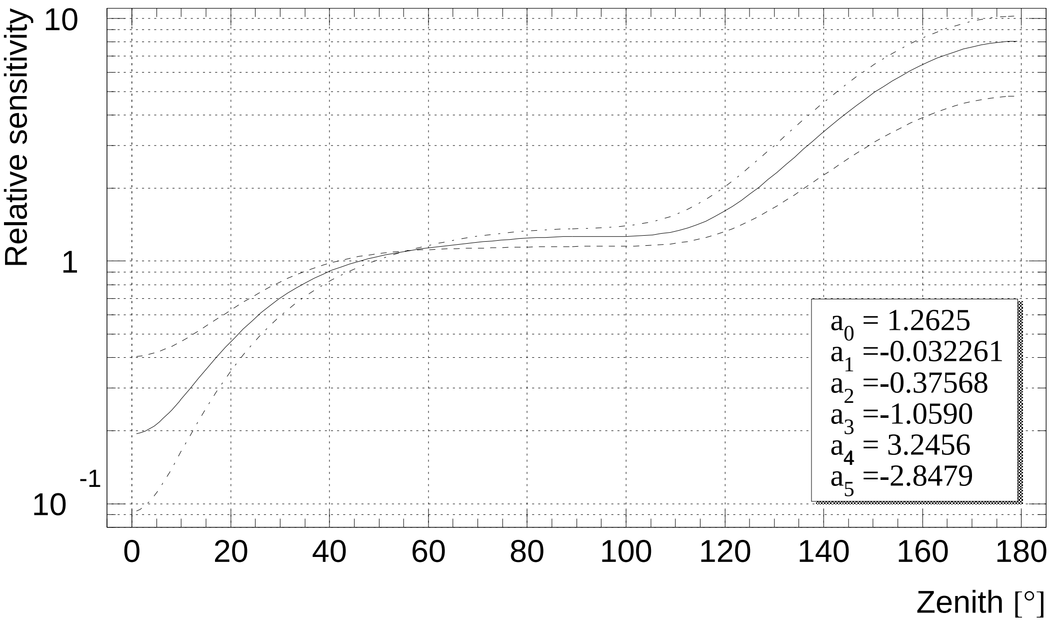

Figure 3.8: A relative change in the angular sensitivity of an optical module relative to the forward direction (zenith of 0°). The sensitivity has been normalized to the case with absence of bubbles. The three curves are for different bubble concentrations resulting in $b_{\mathrm{hole}} = 2\ \mathrm{m}^{-1}$ (solid), $b_{\mathrm{hole}} = 1\ \mathrm{m}^{-1}$ (dashed), and $b_{\mathrm{hole}} = 3.33\ \mathrm{m}^{-1}$ (dot-dashed). The intermediate curve is described by a 5^{th}-order polynomial in $\cos\theta$ with coefficients a_n as shown.

The bubbles shrink in size under increasing pressure, and eventually undergo conversion to an air hydrate phase at large depths [75]. The bubbles dominate scattering in ice above 1000 m depth [63], but below they are almost completely converted into the air hydrate phase with an index of refraction almost identical to that of ice ($n_{\mathrm{ah}}/n_{\mathrm{ice}} \approx 1.004$ [76]). Thus, air hydrate crystal contribution to scattering in AMANDA-B is negligible compared to the effect of impurities.

By melting the ice during the deployment of the detector, air bubbles are reintroduced and they again affect the scattering properties. Since the rate of conversion of air to the air hydrate phase is thought to be very slow compared to a lifetime of a neutrino detector, the increase in scattering near optical modules has to be taken into consideration.

An empirical model of how the directional photon flux detected by AMANDA optical modules is affected within a narrow column of highly scattering ice was developed [77, 78]. Figure 3.8 shows the effect for three different bubble concentrations. The measurements are best described by a scattering coefficient in the hole of $b_{\mathrm{hole}} = 2\ \mathrm{m}^{-1}$ [77].

3.2.4 Light sources

Various light emission sources can be modeled for testing and analysis purposes. The artificial sources with isotropic (e.g., diffuser balls), beamed (lasers), and cosine peaked (LEDs) emissions can be used for analysis of calibration data. For the analysis of physics data, the description of the light emitted by passing muons and muon-generated secondary showers is needed.

Čerenkov light

The light emitted by high-energy muons propagates in a Čerenkov cone, with an opening angle given by [17]

$$\cos\theta_{\check{c}} = \frac{1}{n\beta}, \tag{3.13}$$

where n is the phase index of refraction of the propagation medium, and $\beta \approx 1$ for relativistic muons. The wavelength spectrum and the number of Čerenkov photons emitted are given by

$$\frac{\mathrm{d}N_{\check{c}}}{\mathrm{d}l\,\mathrm{d}\lambda} = 2\pi\alpha \sin^2\theta_{\check{c}} \frac{1}{\lambda^2} \approx 2\pi\alpha \frac{n^2 - 1}{(n\lambda)^2}, \tag{3.14}$$

where α is the fine structure constant (Figure 3.9).

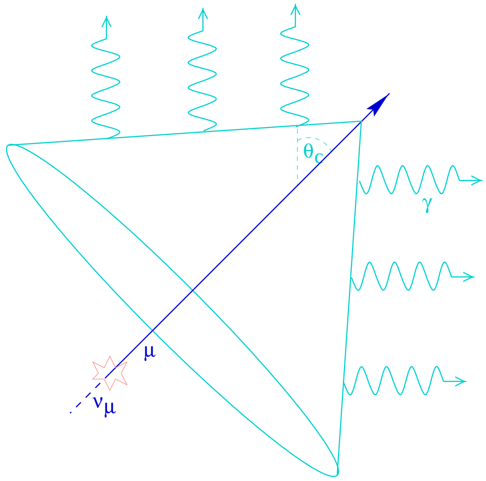

Figure 3.9: Čerenkov cone light emission from a muon.

Shower light

The shower light emission is also Čerenkov in nature, but it originates from secondary particles created in muon energy loss processes. Since the trajectories of these secondaries are not necessarily parallel to that of the parent muon, the Čerenkov cone emission is distorted. In addition, the showers are not point-like, but have a longitudinal development component with a length proportional to the logarithm of their energy. However, this longitudinal component can be approximated with a point-like emission by even further distorting the emission cone if an observation point is at a distance comparable to or larger than the shower length. A detailed study of electromagnetic and hadronic showers generated by high energy muons in water or ice was done by Wiebusch in Section 7.1 of his thesis [61]. Only the most relevant results are mentioned here. The angular distribution of

Table 3.1: The parameters used to describe the light profile emitted by a shower; the first line is for electromagnetic and the second for hadronic showers.

$\theta_{\check{c}}$ [°]	σ_1 [°]	σ_2 [°]	σ_3 [°]	ϵ_1 $[10^{-3}]$	ϵ_2 $[10^{-3}]$	ϵ_3 $[10^{-3}]$	N_1 $[10^{-3}]$	N_2 $[10^{-3}]$	N_3 $[10^{-3}]$	a	b
41.27	2.33	17.6	23.6	-68.3	401	-770	87.5	13.6	13.1	0.73	0.266
41.67	2.54	20.1	22.9	-213	425	-786	40.6	13.9	14.0	0.86	0

emitted light is given by the parameterization

$$\begin{aligned}\frac{\mathrm{d}N_{\check{c}}(\theta)}{\mathrm{d}\Omega} &= \frac{1}{2\pi}\cdot\left[N_1\exp\left(-\left|\frac{\theta-\theta_{\check{c}}}{\sigma_1+\epsilon_1(\theta-\theta_{\check{c}})}\right|\right)\right.\\ &\quad +N_2\exp\left(-\left|\frac{\theta-\theta_{\check{c}}}{\sigma_2+\epsilon_2(\theta-\theta_{\check{c}})}\right|^2\right)\\ &\quad \left.+N_3\exp\left(-\left|\frac{\theta-\theta_{\check{c}}}{\sigma_3+\epsilon_3(\theta-\theta_{\check{c}})}\right|^3\right)\right],\end{aligned} \tag{3.15}$$

where θ is the angle of emission with respect to the parent muon track, $\theta_{\check{c}}$ is treated as a free parameter, and N_i, σ_i and ϵ_i are fit parameters which depend on shower type and energy. The longitudinal to point-like emission angle correction can be expressed as

$$\frac{\mathrm{d}N_{\check{c}}^{corr}(\theta)}{\mathrm{d}\Omega} = \frac{\mathrm{d}N_{\check{c}}(\theta)}{\mathrm{d}\Omega}\cdot(a+b\cdot\cos\theta). \tag{3.16}$$

Due to the large parameter space of various secondary particles and their energies, the results from [61] are simplified for the broad categories of electromagnetic showers and hadronic showers. The fit parameters that are used by `photonics` are given in Table 3.1.

Chapter 4

PMT and electronics response to light

"Oh, I see. Then everything is
wrapped up in a neat little package."
Homer Simpson, *The Simpsons,*
"Bart of Darkness", **1F22**

The AMANDA optical modules (OMs) are independent light detectors, each one consisting of a photomultiplier tube[†] with its bleeder circuit, a glass pressure vessel, and silicon gel providing optical coupling between the pressure vessel and the PMT (Figure 4.1). PMTs are the most sensitive light detectors with large collection areas in use. Even in the age of CCDs, they still reign supreme when large scale photon counting is necessary. Their ability to resolve single photons with a large signal to noise ratio is crucial to experiments such as AMANDA.

[†] Almost exclusively a 14-stage, 8" Hamamatsu R5912-2.

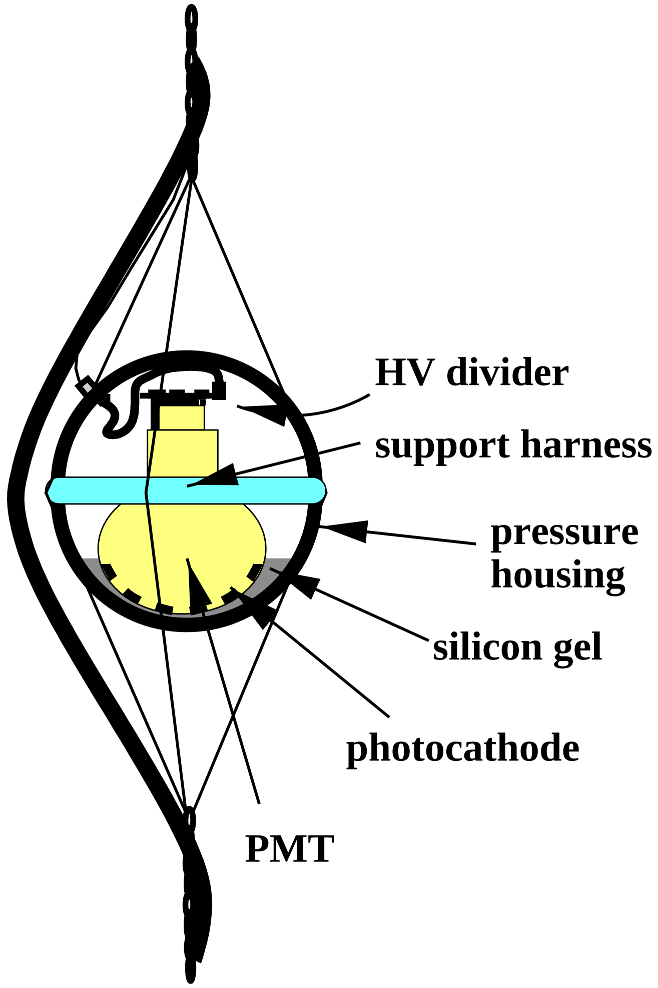

Figure 4.1: An optical module, shown mounted on a main electrical cable that supplies power and carries PMT signals to the surface.

4.1 Pulse generation

The probability that a photon reaching an OM will be detected and that a subsequent electrical pulse will be generated needs to be evaluated in order to understand the collection efficiency of an OM. The optical properties of an OM that have to be considered are its angular acceptance and its absolute efficiency of light detection. That way a function $\epsilon(\theta, \lambda)$, the OM detection efficiency as a function of light incident angle and wavelength,

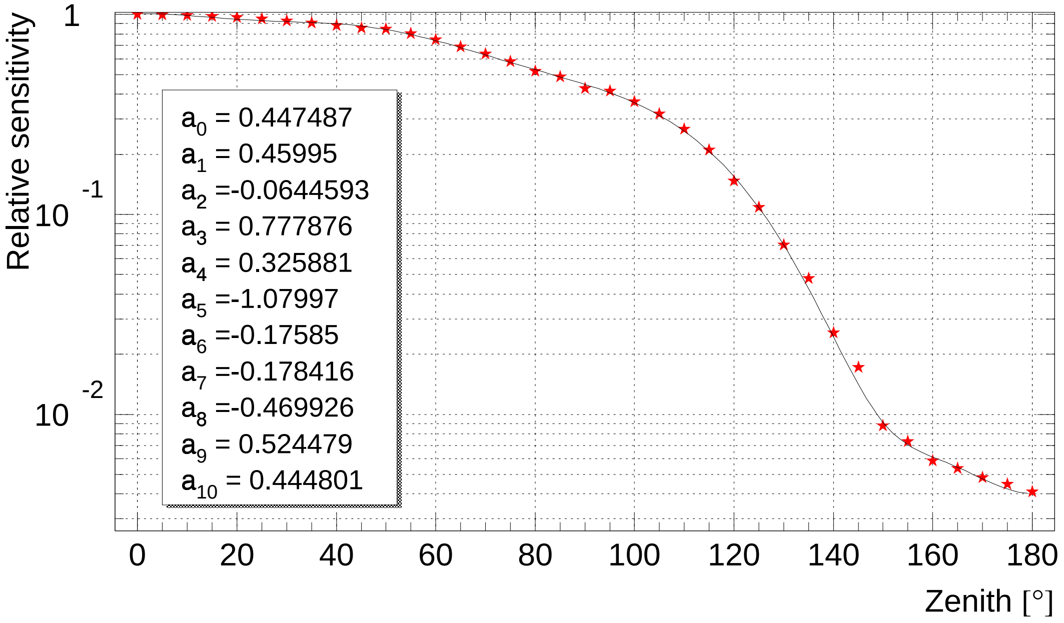

Figure 4.2: The angular sensitivity of an optical module, normalized to unity in the forward direction. The fit is a 10th-order polynomial with coefficients given for $\cos\theta$.

can be established. Due to complex geometry of OM components, the angular acceptance would be difficult to calculate from first principles, so a laboratory measurement will be used. Figure 4.2 has been adapted from Ref. [79], where the relative sensitivity of an OM for plane wave detection has been normalized to the forward (head-on) direction.

The absolute angular efficiency of an optical module can be expressed in terms of the absolute efficiency for a plane light wave incident in the forward direction and the relative angular efficiency as

$$\epsilon(\theta, \lambda) = \epsilon_0(\lambda) \cdot R(\theta), \tag{4.1}$$

where ϵ_0 is the absolute efficiency in the forward direction and R is taken to be the parameterization in Figure 4.2. The absolute efficiency is given by

$$\epsilon_0(\lambda) = \prod_I F_I^{\mathrm{t}}(\lambda) \prod_M T_M(\lambda) \epsilon_{\mathrm{qe}}(\lambda) \epsilon_{\mathrm{dy}}, \tag{4.2}$$

where $F_I^{\mathrm{t}}(\lambda)$ is the Fresnel transmittance coefficient of interface I (ice - pressure vessel, pressure vessel - silicone gel, silicone gel - PMT glass), $T_M(\lambda)$ is the transmittance of medium M (pressure vessel, silicone gel, PMT glass), $\epsilon_{\mathrm{qe}}(\lambda)$ is the quantum efficiency of the photocathode, and ϵ_{dy} is the collection efficiency of the first dynode in the PMT gain amplification stage. It is necessary consider only the first dynode since it is the only dynode whose inefficiency can can quench photon detection. Inefficiencies of all subsequent dynodes will only affect the size and the shape of the signal produced by a photon. The Fresnel transmittance, averaged over photon polarizations, is given by [80]

$$F^{\mathrm{t}}(\theta_1, n_1, \theta_2, n_2; \lambda) = 2 n_1 n_2 \cos\theta_1 \cos\theta_2 \times \left[\frac{1}{(n_1 \cos\theta_1 + n_2 \theta_2)^2} + \frac{1}{(n_1 \cos\theta_2 + n_2 \theta_1)^2} \right], \tag{4.3}$$

where $n_{1,2}$ and $\theta_{1,2}$ are indices of refraction and incident and refracted angles in the respective media (Figure 4.3). The transmittance of a medium can be simply treated with the use of the characteristic attenuation length of the medium, so that

$$T_M(l_M; \lambda) = \exp\left(-\frac{l_M}{\tau_M(\lambda)} \right) \tag{4.4}$$

gives the probability that a photon of wavelength λ survived over the path length l_M in the medium with the mean attenuation length $\tau_M(\lambda)$.

Since the measurement of the relative angular sensitivity of an OM has been averaged over the projected surface of the OM, the same has to be done for the absolute efficiency. This would be a numerically intensive calculation if it were to be done for each

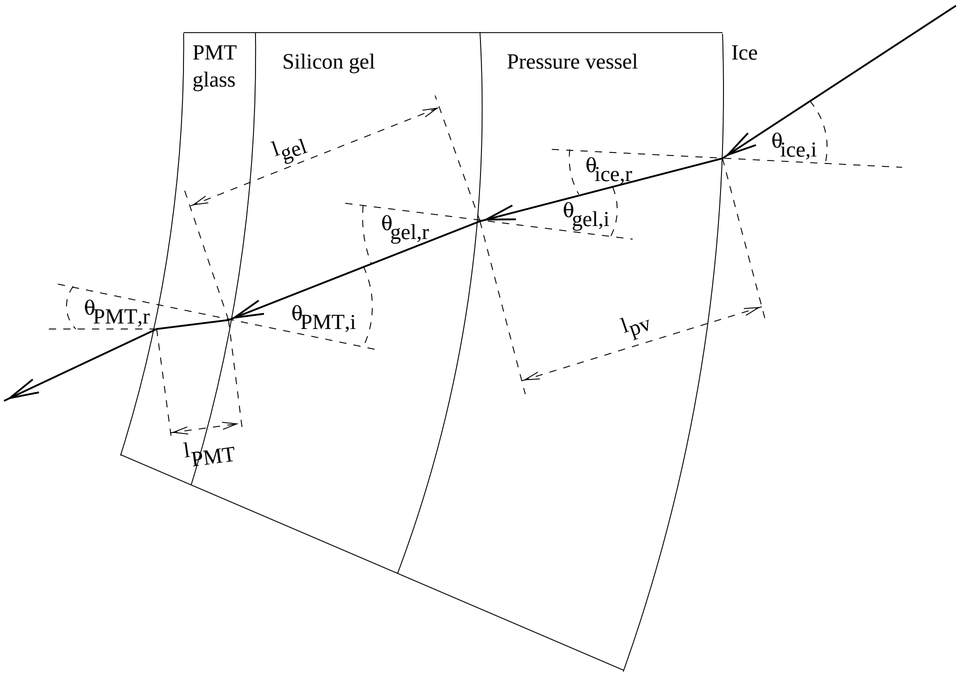

Figure 4.3: Photon transmission through the various OM layers. Figure adapted from [81].

photon incident on the curved surface of an OM, so one should resort to a shortcut. If one imagines that the optical module has been projected onto a plane, then the absolute efficiency for the detection of a plane light wave incident on it is simply given by

$$\begin{aligned} \epsilon_{\text{flat}}(\lambda) &= \prod_I f_I^{\text{t}}(\lambda) \prod_M t_M(\lambda) \epsilon_{\text{qe}}(\lambda) \epsilon_{\text{dy}}, && (4.5) \\ f^{\text{t}}(n_1, n_2) &= \frac{4 n_1 n_2}{(n_1 + n_2)^2}, && (4.6) \\ t_M(\lambda) &= \exp\left(-\frac{l_0}{\tau_M(\lambda)}\right). && (4.7) \end{aligned}$$

Considering that the thickness l_0 of each medium is known, both the f^{t} and the t_M terms can be calculated. To correct for the curvature, a wavelength dependent correction factor is used, defined as

$$\mathcal{C}(\lambda) = \frac{\int_0^r \epsilon_0(\lambda) 2r' dr'}{\epsilon_{\text{flat}}(\lambda) r^2}, \tag{4.8}$$

where the integral runs over the radius of an OM, with r being the ratio of PMT and OM radii. Then,

$$\epsilon_0(\lambda) = \epsilon_{\text{flat}}(\lambda) \cdot \mathcal{C}(\lambda). \tag{4.9}$$

4.2 Pulse detection and calibration

The preceding section describes the probability that a photon hitting an optical module will be detected, i.e., generate a PMT pulse. The photon-generated pulse (or photo-electron pulse, PE) is amplified and propagated to the detector readout electronics where it is discriminated and its amplitude and timing are read out. To handle large experimental data collection rates, the only information coming from an OM that is recorded in any single data event are the start and the end of each pulse and the highest pulse amplitude seen during the event. This is sufficient to correctly describe the majority of events, but these might not be the most physically interesting ones[‡].

Several factors complicate the counting of the exact number of photons detected at depth. The pulses have to travel 1.5 km or more to reach the surface. During their propagation, the dispersion in a copper conductor severely affects the pulse shape and timing profile. Pulses are ~10 ns wide at the PMT anode, but they stretch to 250 ns or more by the time they reach the surface. This causes several closely separated pulses to merge into one pulse by the time they reach the surface. Since the pulse shape information is lost, it can be hard to reconstruct how many photo-electrons contributed to the observed pulse. In the event of a pulse train, a further complication arises from the fact that only the

---

[‡] Thanks to advances in computing technology, continuing upgrades to AMANDA readout electronics will soon allow for more complete description of data coming from the ice.

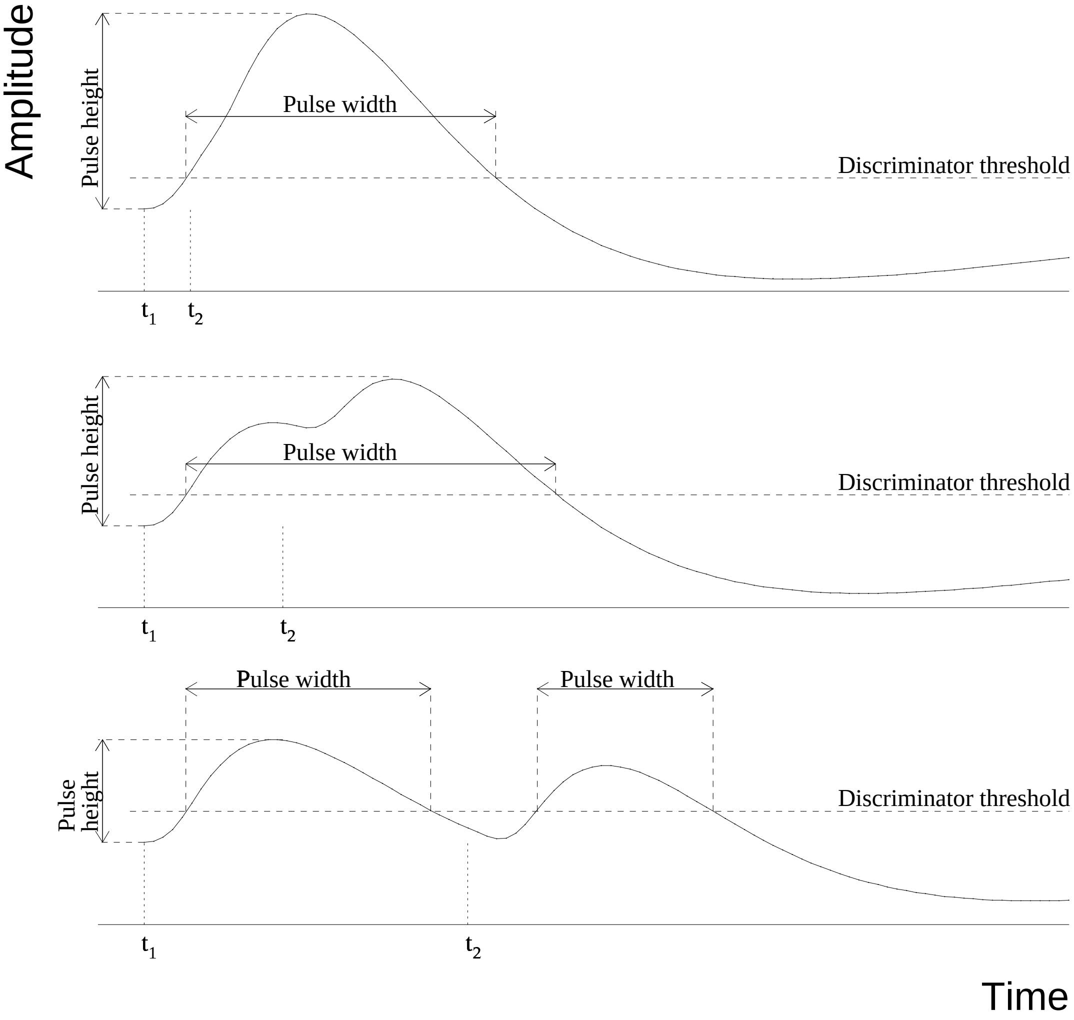

Figure 4.4: A graphical representation of how two pulses separated by three different delay times can appear in the readout electronics. The pulses are recorded when they exceed a preset discriminator threshold, at which point the highest pulse amplitude and the pulse widths are measured. Positions t_1 and t_2 mark the actual beginning of each pulse.

largest pulse amplitude will be recorded and the rest of them will be lost. As an example, three scenarios of how two photo-electrons can appear are depicted in Figure 4.4. The data calibration can partially rectify the situation by using the fact that the pulse amplitude and width are correlated, so some missing information can be approximated.

4.3 Probabilistic treatment of pulse amplitude

Since it can not be determined with certainty how many photons made up any individual pulse, a probabilistic treatment of pulse amplitudes should be used. For any given measured pulse, probabilities can be assigned that the pulse was created by one, two, three, or more coincident photons.

Laboratory measurements show a linear mean amplitude response to the number of coincident photons in a pulse (see Ref. [82], Appendix D), with approximately Gaussian distributions of amplitudes [83]. The widths of the Gaussians can be described as functions of the mean amplitudes μ, such that

$$\sigma(N) = \mu \cdot \begin{cases} 0.42 & , \text{for}\, N = 1\,\text{PE} \\ 0.22 & , \text{for}\, N > 1\,\text{PEs} \end{cases} \tag{4.10}$$

The probability that a pulse of amplitude A is the result of N photons can then be written as

$$P_{\text{pulse}}(A; N) = \frac{1}{\sqrt{2\pi}\sigma(N)} \exp\left(-\frac{1}{2}\left(\frac{A-N}{\sigma(N)}\right)^2\right), \tag{4.11}$$

where A has been re-normalized to units of mean single PE pulse height.

This type of amplitude treatment assumes that all photons recorded by an OM have been coincident. Since this will not always be the case in the experiment, time delay between the photons should be considered. In this work, primarily due to computational constraints in generating light density tables, the time dimension will be ignored. In the future, refinements to the energy reconstruction technique described herein should include the proper treatment of photon and pulse timing.

4.4 Converting photon flux into pulse amplitude

A probabilistic description of the light density measurement can be made by combining the treatment of the light emission and propagation described in previous chapters with the treatment of light detection described here.

The average photon flux calculated by Equation (2.41) can be converted into the mean photocathode illumination by integrating over all photon arrival directions and weighting them with Equation (4.1). Since Equation (4.1) contains all detection efficiencies, this procedure results in a mean "photo-electron density". The probability of observing a certain number of photo-electrons given a certain mean density is Poissonian, so

$$P_{\text{ampl}}(A; \langle NPE \rangle) = \sum_{NPE=0}^{NPE_{\max}} P_{\text{poisson}}(NPE; \langle NPE \rangle) \cdot P_{\text{pulse}}(A; NPE) \tag{4.12}$$

is the probability that the pulse amplitude A has been recorded due to the mean photo-electron density $\langle NPE \rangle$. Considering that the Poissonian distribution is only valid for low values of the mean, the working version is defined as

$$P_{\text{poisson}}(x; \mu) = \begin{cases} \dfrac{\mu^x}{x!} \exp(-\mu) & , \text{for}\, x < 30 \\ \left[\sqrt{\dfrac{\pi}{2}\mu}\left(1 + \text{erf}\sqrt{\dfrac{\mu}{2}}\right)\right]^{-1} \exp\left(-\dfrac{1}{2}\dfrac{(x-\mu)^2}{\mu}\right) & , \text{for}\, x > 30 \end{cases} \tag{4.13}$$

where the Gaussian distribution has been normalized to unity on range $[0, \infty)$.

4.5 Discriminator threshold effect

The use of fixed level discriminators for pulse detection results in a nonzero probability that a photon that produces a photo-electron in an OM will not be recorded by the detector electronics. This can easily be seen from the functional form of Equation (4.11) where the value of amplitude A can range all the way down to zero.

The probability that a photon conversion in OM i will go unrecorded can be expressed as

$$P_{\mathrm{th}}^{i}(\langle NPE\rangle) = \int_{0}^{A_{\mathrm{th}}^{i}} P_{\mathrm{ampl}}(A;\langle NPE\rangle)dA, \tag{4.14}$$

where A_{th}^{i} is an OM-dependent relative discriminator threshold expressed in units of mean single PE pulse height.

The preceding three chapters have outlined all physical processes which have to be considered when reconstructing muon energies in AMANDA. Now we turn to the description of the muon energy reconstruction technique and its applications.

Chapter 5

Muon energy reconstruction technique

"Trying is the first step towards failure."
Homer Simpson, *The Simpsons,*
"Reality Bites", **5F06**

Due to the stochastic nature of muon energy loss and light detection in AMANDA, the energy measurement of any specific muon event recorded by the detector will have significant uncertainties. Thus, information about muon energy that can be extracted on an event by event basis is limited. A more suitable approach is to treat energy measurements in a probabilistic fashion.

The basic assumption made here about energy measurement is that the amount of light generated by a muon is proportional to its energy. This proportionality relation can be easily established. From a basic notion of photon flux around a light source, we know that the flux Ψ_γ will be proportional to N_γ, where N_γ is the number of photons generated by the source. By virtue of Equation (3.14), $N_\gamma \equiv N_{\check{c}} \propto l_{\text{eff}}$, with l_{eff} coming from both muon (Equation 2.40) and shower (Equation 2.39) contributions. If we assume that for high-energy muons the majority of light produced and energy lost is due to secondary showers, then by Equations (2.3) and (2.39), $l_{\text{eff}} \propto E_{\text{s}} \propto \Delta E \propto E$. Thus, $\Psi_\gamma \propto E$. Adding the detector response,

$$\Psi_{\text{OM}}(E; \mathit{geometry}) \propto NPE_{\text{OM}} \propto A_{\text{OM}}, \tag{5.1}$$

where A_{OM} is the amplitude measured by an OM, NPE_{OM} is the number of photo-electrons collected by an OM, and E is the energy of a muon as it *enters* the active detector volume. In the case of AMANDA, this active volume extends approximately 50–100 m beyond the instrumented volume of the detector[†] and is somewhat a matter of definition. Programs and tables involved in exact calculations of energy measurement relationships are described in Appendix C.

5.1 Likelihood generation

The measurement of energy is based on a Maximum Likelihood method where the hypothesis that would most probably result in the given set of observables is selected as a solution. The likelihood we are interested in can be constructed as

$$\mathcal{L}(E; \mathit{geometry}) = \frac{W_{\text{global}}}{N_{\text{OM}}^{\text{tot}}} \cdot \prod_{i=1}^{N_{\text{OM}}^{\text{tot}}} w_i \cdot P_i(A_i), \tag{5.2}$$

where P_i is the probability of observing pulse amplitude A_i in OM i out of the total number of OMs $N_{\text{OM}}^{\text{tot}}$ in a muon active volume. The muon active volume is an arbitrary cylinder

---

[†] It is a function of the optical properties of ice surrounding the detector.

with the muon track as its axis. Additional weights w_i and W_{global} are associated with an OM and the entire detector, respectively. An implicit dependence on muon energy and geometry is assumed for all variables in this section. The geometry of an event, i.e., the direction and the relative position of a muon track with respect to the detector array, is taken from the AMANDA muon-direction reconstruction [41]. For the purposes of energy measurement this geometrical information is taken to be *a priori* correct. Additionally, since muon vertex detection and fitting algorithms have not been developed for AMANDA data, all muons will be assumed to have been created outside of the detector. In the future, these assumptions can be amended since muon direction, vertex, and energy reconstruction could be performed simultaneously, thereby improving each one.

The probabilities P_i have to be treated separately for two cases: (i) when the OM did not record a pulse and (ii) when the OM recorded a pulse;

$$P_i(0) = P_{\text{no hit}} + P_{\text{hit}} \cdot P^i_{\text{th}}(\langle NPE \rangle), \tag{5.3}$$

$$P_i(A_i) = P_{\text{hit}} \cdot (1 - P^i_{\text{th}}(\langle NPE \rangle)) \cdot \frac{P_{\text{ampl}}(A_i; \langle NPE \rangle)}{P_{\text{ampl}}(A_{\text{ml}}; \langle NPE \rangle)}, \tag{5.4}$$

$$P_{\text{no hit}} = P_{\text{poisson}}(0; \langle NPE \rangle) \cdot (1 - P_{\text{noise}}),$$

$$P_{\text{hit}} = 1 - P_{\text{no hit}},$$

where P_{noise} is the experimentally measured OM dark noise rate. According to conditional probability rules, the probability $P_i(A)$ for observing A_i can be renormalized by P_{ampl} of observing the most likely amplitude A_{ml} for a given $\langle NPE \rangle$.

The contributing weights W_{global} and w_i can be adjusted to include more detailed knowledge of detector response (e.g., event topology, hit time correlations, etc.) and thereby improve the resolution of the energy reconstruction. For the purposes of the analysis pre-

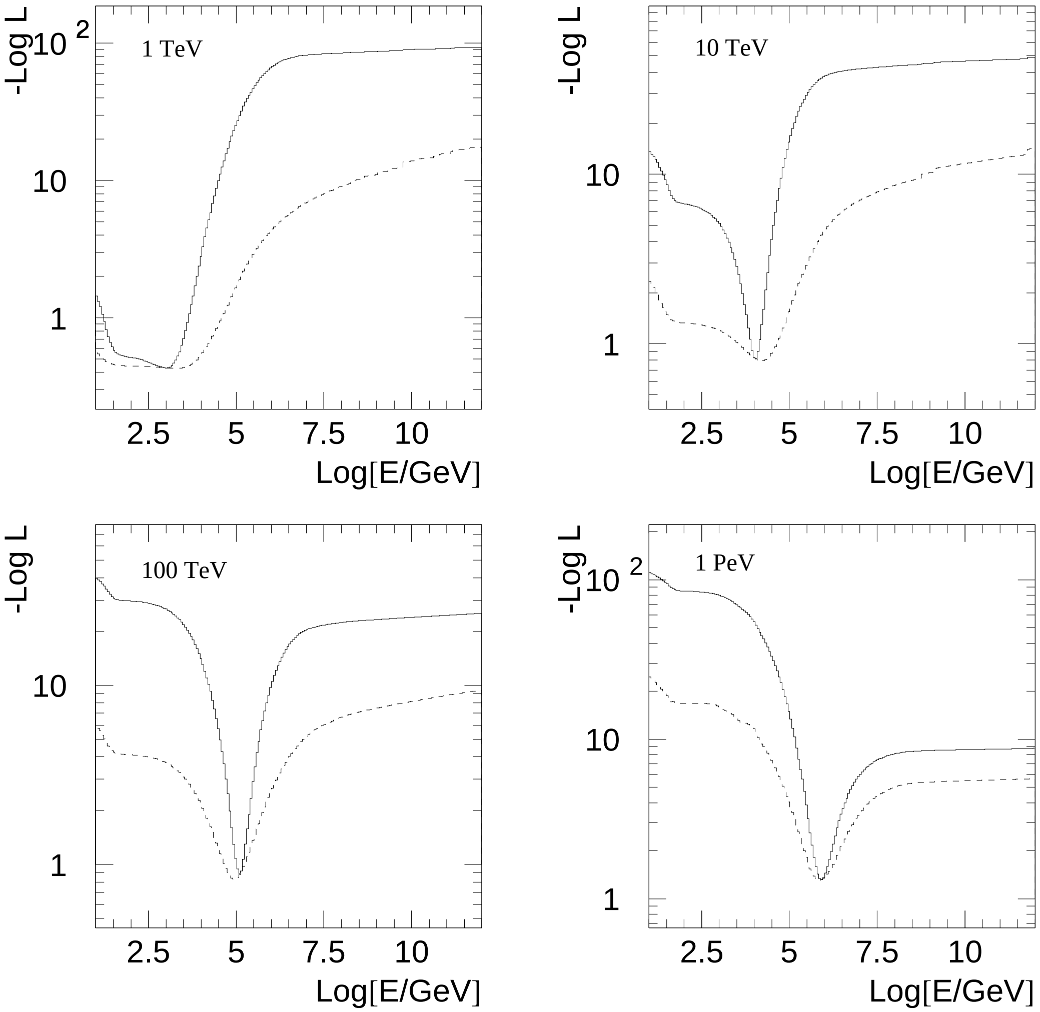

Figure 5.1: Negative logarithm of muon energy likelihood *vs* muon energy for several well reconstructed events. The dashed line is the likelihood without W_{global}. One can see that the use of the global event weight constrains the likelihood maximum, resulting in an improved resolution. This is especially important for lower energy muons (e.g., 1 TeV) where the neighborhood of the likelihood maximum is nearly flat.

sented in this work, $w_i \equiv 1$ and

$$W_{\mathrm{global}} = \exp\left(-\frac{1}{2}N_{\mathrm{OM}}^{\mathrm{tot}}(\mu_{obs} - \mu_{exp})^2\right), \tag{5.5}$$

$$\mu_{obs} = \frac{N_{\mathrm{OM}}^{\mathrm{hit}}}{N_{\mathrm{OM}}^{\mathrm{tot}}}, \quad \mu_{exp} = \frac{\sum_i P_{\mathrm{hit}} \cdot (1 - P_{\mathrm{th}}^i(\langle NPE \rangle))}{N_{\mathrm{OM}}^{\mathrm{tot}}},$$

where $N_{\rm OM}^{\rm hit}$ is the number of hit OMs in the muon active volume. The global event weight, $W_{\rm global}$, is thus the probability that the observed number of hit OMs has deviated from the expected number. This quantity by itself could be used as a crude energy estimator. Combined with the amplitude measurements, it improves the overall resolution of energy reconstruction. An example of reconstructed muon energy likelihoods for four simulated events with different true muon energies is shown in Figure 5.1.

5.2 Characterization of energy reconstruction

Due to the lack of a high-energy muon calibration beam, the only way to tie down the response of the detector to muon energy is through a comparison with a detector Monte Carlo simulation. So, instead of gathering calibration data with the detector, one does it with the detector simulation. This implies that the quality of energy reconstruction that can be achieved is directly tied to the quality of the detector Monte Carlo, i.e., *the energy reconstruction will be only as good as the detector simulation.*

An energy calibration MC data set was generated to study properties of the energy reconstruction algorithm and to be used for generation of the smearing matrix needed for spectrum unfolding (see Section 5.3). The data set was generated by simulating an isotropic muon flux, with muon energies in the range 50 GeV to 50 PeV. The muon creation point was either set on the plane of a disk with a radius of 350 meters and centered on a 350 m radius sphere surrounding AMANDA, or inside this 350 m radius sphere, thus covering the entire geometrical phase space. Muons were propagated to and through the active detector volume[‡]

[‡] Cylinder with height 620 m and radius 135 m around AMANDA.

with `MMC` [45], and the detector response was simulated by `amasim` [84]. The directional reconstruction and hit data cleaning followed the prescription set by DeYoung [85].

5.2.1 Hit frequency comparison

To verify that the energy reconstruction tables agree with MC data, a simple test can be made. For a muon with known direction and energy, energy reconstruction tables can be used to calculate the expected number of OMs that will record a photon. This expected number of hit OMs, μ_{exp}, can then be compared to the observed number, μ_{obs}, as simulated by the detector MC (see definitions below Equation 5.5). If this is repeated for a large number of muons, the agreement between the distributions of predicted means and observed numbers of hits is expected. Figure 5.2 shows this comparison for two mono-energetic muon data sets.

The fits in the bottom plots of Figure 5.2 are Gaussian, implying that all variation is due to the stochastic nature of light emission and detection. The non-Gaussian high-end tails are due to the appearance of very large, but rare secondary showers associated with muon energy loss. For fixed energy, the widths of the Gaussian fits are inversely proportional to $1/\sqrt{N_{\text{OM}}^{\text{tot}}}$ (Figure 5.3). At first glance this might be counter-intuitive, since the width of the Gaussian distribution would be expected to be proportional to the number of sampling points. However, this proportionality holds only in the case where the sampling points are equally likely to record a hit. In the present case, the sampling points (i.e., OMs) are not equally likely to record the light since its intensity drops off with the distance from a muon track.

The slight disagreement between distributions in Figure 5.2, best visible as nonzero

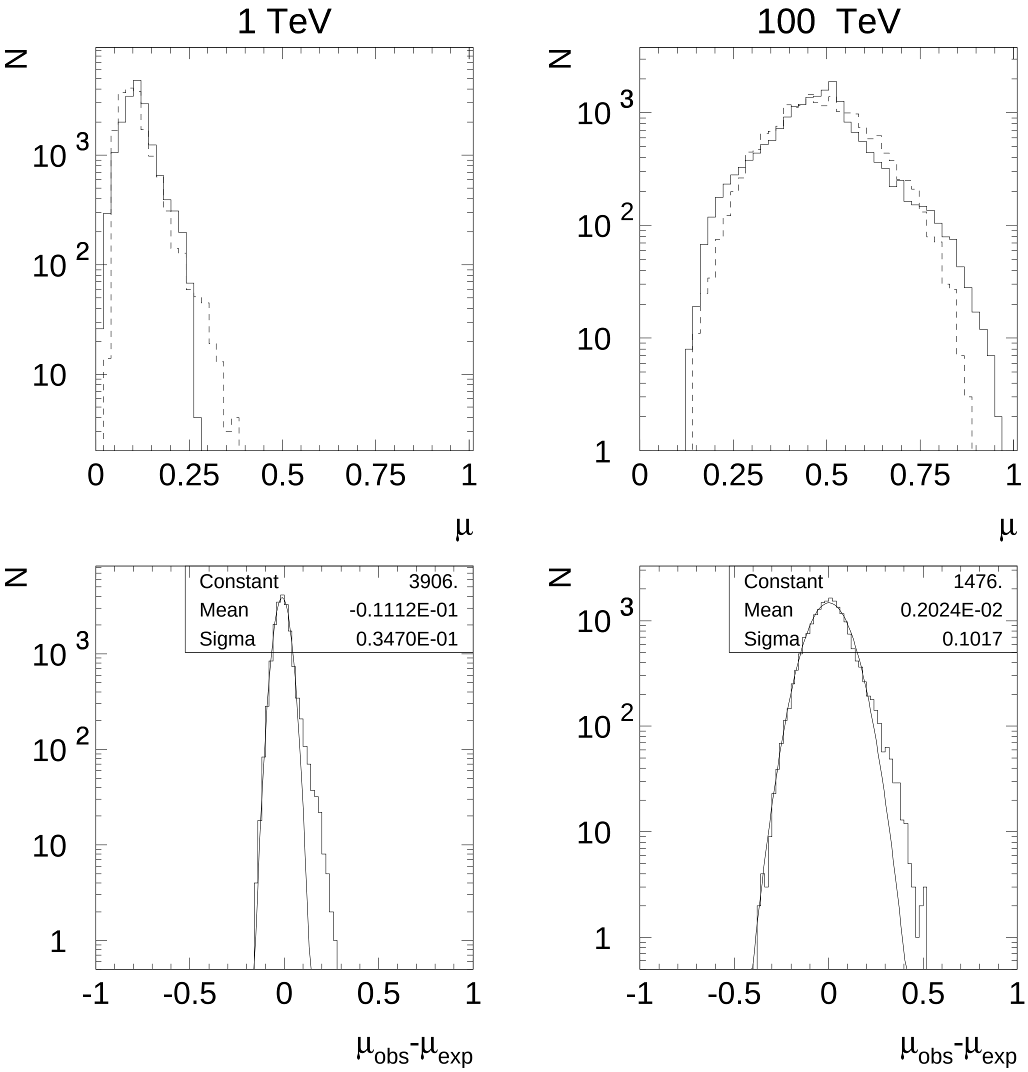

Figure 5.2: Comparison of expected (solid) and observed (dashed) fraction of OMs hit for 1 TeV (left plots) and 100 TeV (right plots) muons. The expected fraction is calculated from energy reconstruction tables and the observed fraction is taken from the detector simulation. The top plots show fraction distributions, while the bottom plots show fraction difference distributions. See text for discussion.

means of the Gaussian fits, is attributed to the use of different photon density tables for the two cases (expected and observed). Due to technical reasons, at the time of writing, `photonics` based tables were not available for the detector simulation, so alternate tables

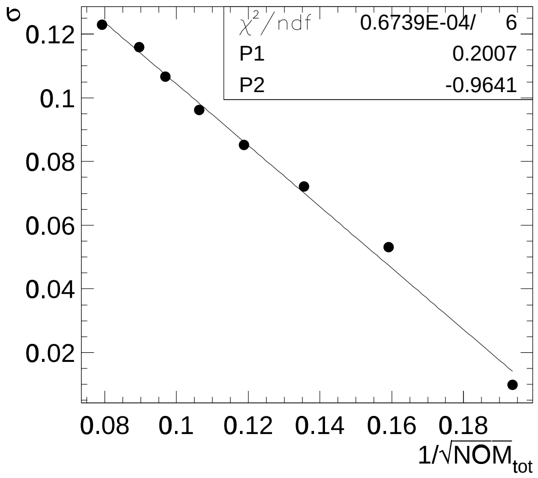

Figure 5.3: The width of distribution of hit fraction difference as a function of $N_{\mathrm{OM}}^{\mathrm{tot}}$ for a 100 TeV isotropic muon flux. $N_{\mathrm{OM}}^{\mathrm{tot}}$ is varied by changing the muon active volume. The fit is a straight line.

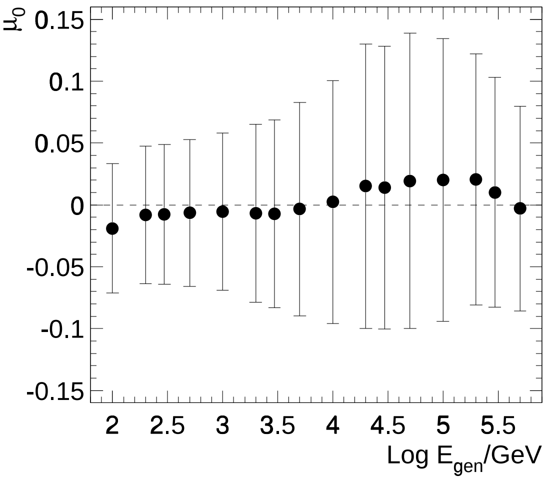

Figure 5.4: The fitted mean of the fraction difference as a function of muon energy. The error bars correspond to widths of Gaussian fits.

were used [74]. However, these substitute tables do not fully treat the physics of light propagation in ice. The differences resulting from their are dependent on muon energy (Figure 5.4).

5.2.2 Quality of energy reconstruction

The best way to test just the energy reconstruction algorithm is to provide it with the true muon trajectory and the true photon hit distribution before it is affected by detector electronics. This allows for the independent study of its properties without effects of muon direction reconstruction or any other data treatment.

Figure 5.5(a) shows the reconstructed energy spread – the difference between reconstructed and true energies – as a function of reduced maximum likelihood. The reduced

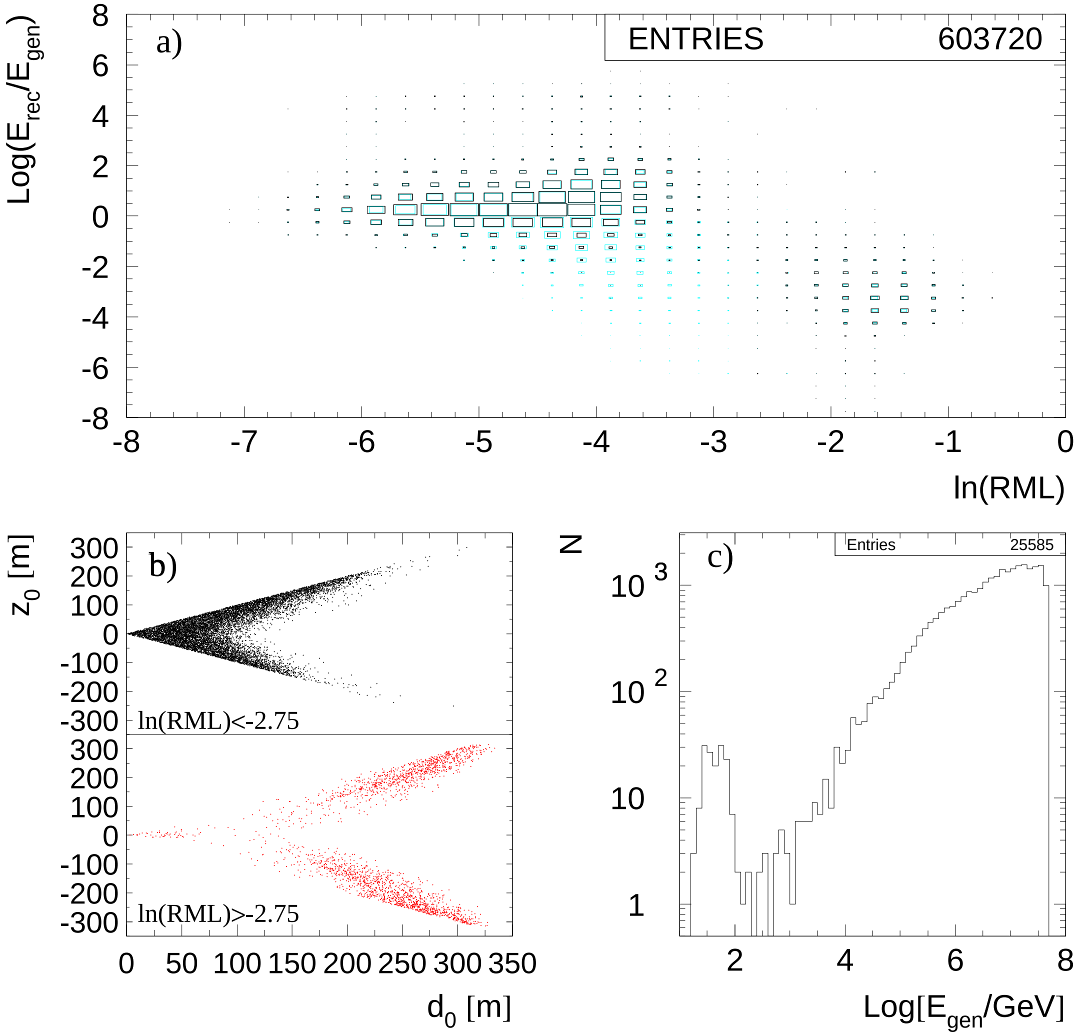

Figure 5.5: Plot (a) shows the reconstructed energy spread as a function of reduced maximum likelihood of the fit. Black boxes are for through-going and stopping muons, while cyan boxes are for starting and contained muons. Plot (b) shows a scatter plot of the z coordinate of closest approach point of the muon track *vs* the closest approach distance. Events in the top panel satisfy $\ln(RLM) < -2.75$ while events in the bottom panel do not. Plot (c) shows the initial muon energy distribution for events with $\ln(RML) > -2.75$.

maximum likelihood[§], $RML = -\ln \mathcal{L}/(N_{\mathrm{hit}} - 1)$, is a measure of fit quality. The four possible muon event types have been separated into two categories; through-going[¶] and

---

[§] analogous to χ^2 of a fit

[¶] Muon is created outside of the detector active volume and it travels through the entire detector.

stopping[‖] muons, and starting[**] and contained[††] muons (see Figure 5.6 for examples).

For the majority of through-going and stopping events the reconstructed energy is distributed around the true energy, except for the group of events with high values of reduced maximum likelihood. On closer inspection, it is revealed that this misreconstructed group of events consists of high energy corner clippers; events in which the muon never enters the instrumented detector volume but passes by one of the corners, and is energetic enough to create a majority trigger in the array (Figure 5.7). The explanation for both the underestimate of the energy and the low quality of energy fit is tied to the way that the active detector volume is used in the simulation. Since a high degree of computational efficiency is required, the muon propagator program was used to calculate and record fully stochastic muon energy losses only inside the active volume. For very energetic muons this active volume has been underestimated, and an insufficient amount of light has therefore been simulated. The muon energy reconstruction responds by assigning a lower energy to the muon, but also by indicating that the observed light distribution is not fully consistent with the reconstructed energy. Enlarging the active volume would eliminate this problem, but it would impose a reduction in simulation speed and would strain some other technical aspects of the simulation chain. However, the real life muons will not be limited to light emission only inside the active volume, so this subclass of incorrectly simulated events can be safely ignored.

For the distributions of starting and contained muons there is a large tail of events with underestimated energies. This is due to the fact that energy reconstruction is currently

---

[‖] Muon is created outside of the detector active volume and it decays somewhere in the detector.

[**] Muon is created inside the detector active volume and it travels through the entire detector

[††] Muon both is created and decays inside the detector.

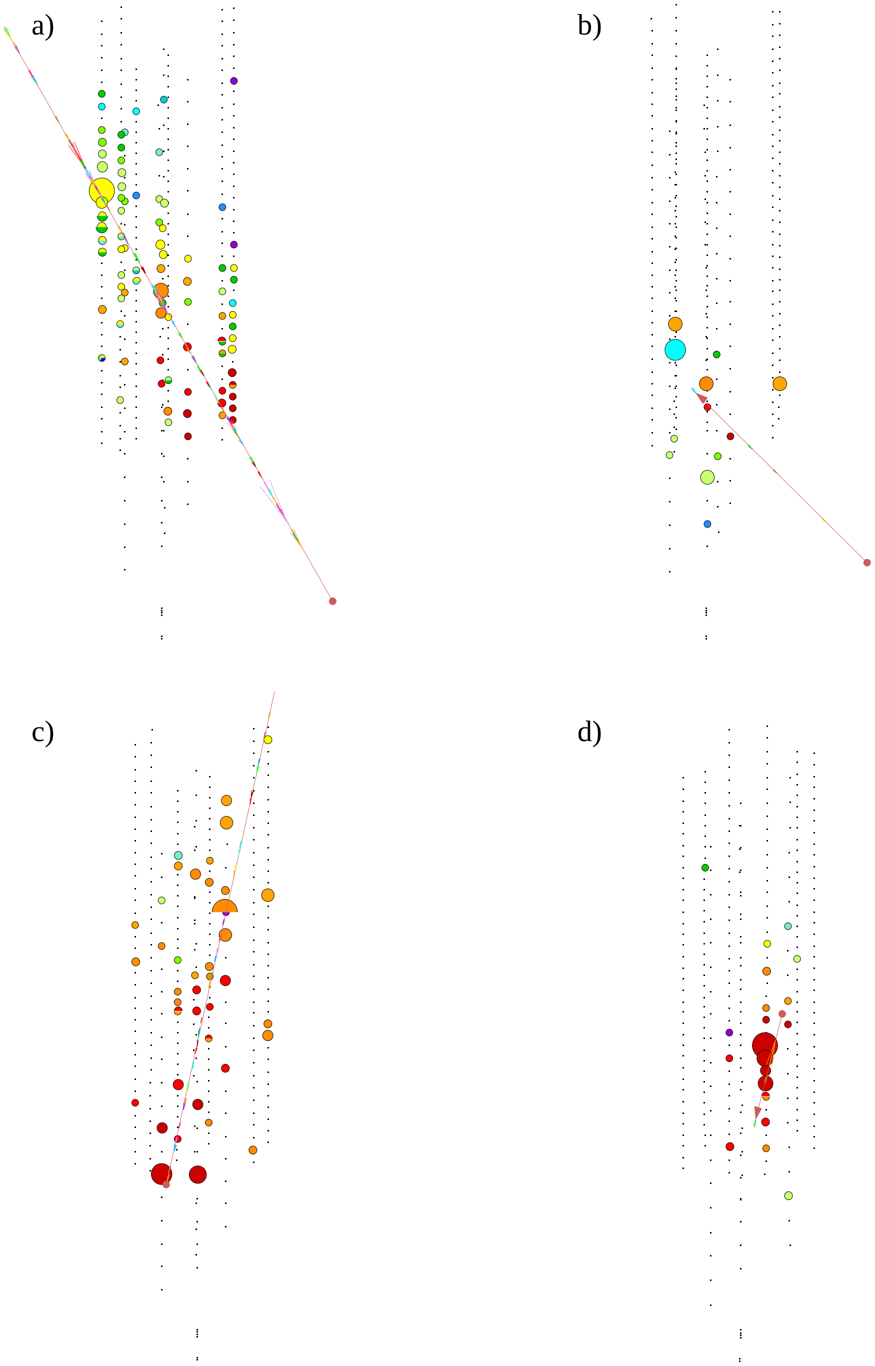

Figure 5.6: Four simulated muon events in AMANDA, one of each possible type: a) through-going, b) stopping, c) starting, and d) contained. Hit time flows from red to violet and size represents number of recorded photons.

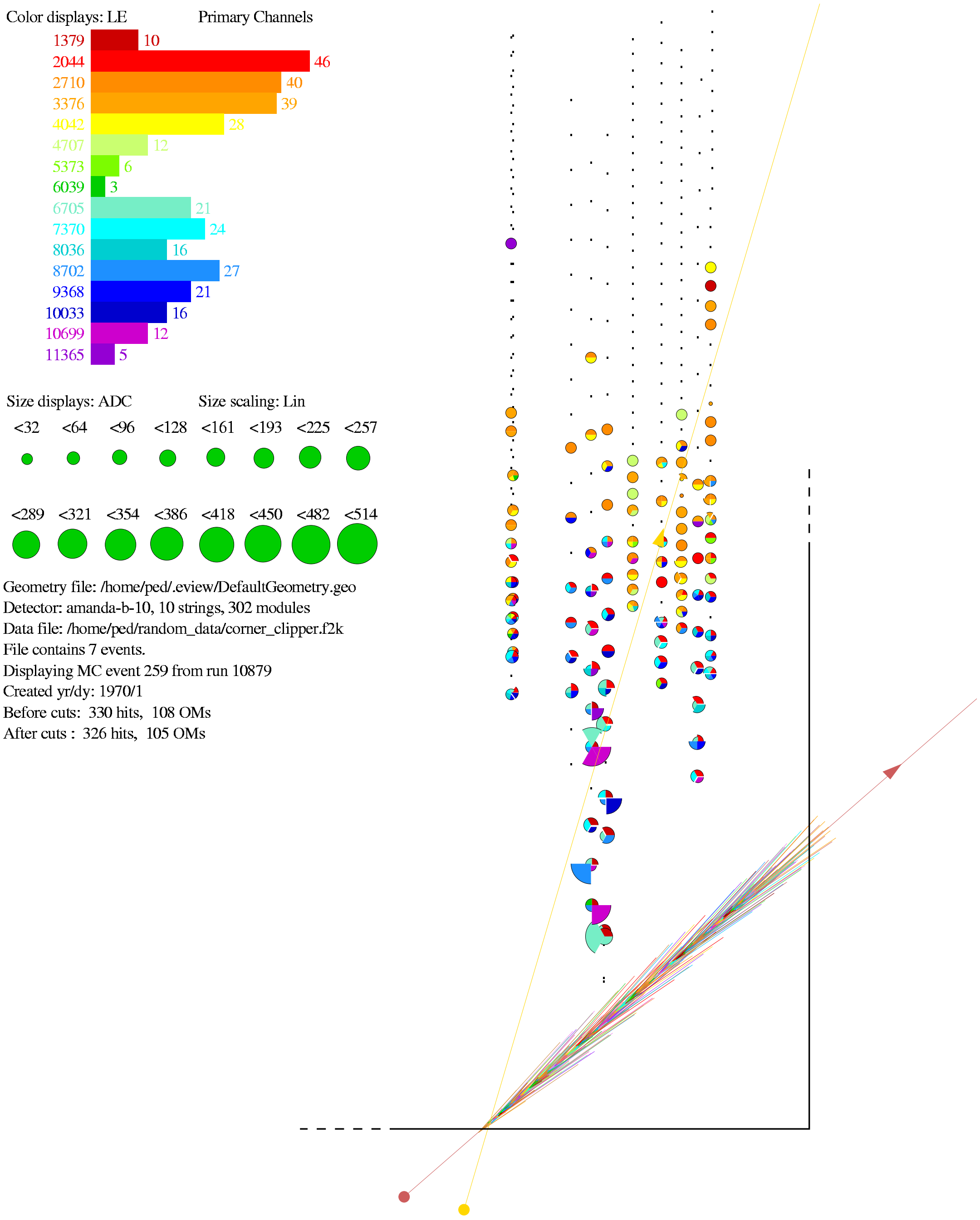

Figure 5.7: A high-energy corner clipper MC event. The true track (red) surrounded by showers is well outside AMANDA, while the reconstructed track (yellow) goes through it. Solid black lines indicate the approximate boundary of the active detector volume. Note that no showers are recorded outside the active volume.

not using the muon vertex information. It assumes that all muons have been created outside of the detector and tries to assign energy accordingly. Since there is no light emitted between the detector edge and the muon vertex, the reconstruction algorithm will find the maximum likelihood at a lower muon energy. The longer is the "missing" segment, the lower will be the reconstructed energy. Once the muon vertex reconstruction becomes available, it will be trivial to adjust the energy reconstruction algorithm to use this additional information.

In the rest of the figures presented in this section, only the through-going/stopping sample will be used and corner-clipper events will be cut away by requiring $\ln(RML) < -2.75$.

Angular dependence

The energy reconstruction quality shows almost no dependence on muon direction (Figure 5.8). The slight curvature in cosine of zenith dependence can be attributed to different lengths of AMANDA as a function zenith angle (from $\sim 120 - 600$ m at extremes). The enhancement of mean reconstructed energies near horizontal directions is most likely due to reduced sampling efficiency of the light emitted by a muon.

The excess of events with energy misreconstructed by more than three orders of magnitude can be attributed to those muons which experience a single large energy loss. Figure 5.9 shows the size of the largest shower as a fraction of the initial muon energy for events misreconstructed by more than three orders of magnitude ($\log(E_{\text{rec}}/E_{\text{gen}}) > 3$) compared with the rest of the events. Misreconstructed events show a high occurrence of large energy deposition in a single shower (Figure 5.10). Due to the shape of AMANDA, muons with trajectories closer to horizontal are more susceptible to this type of energy

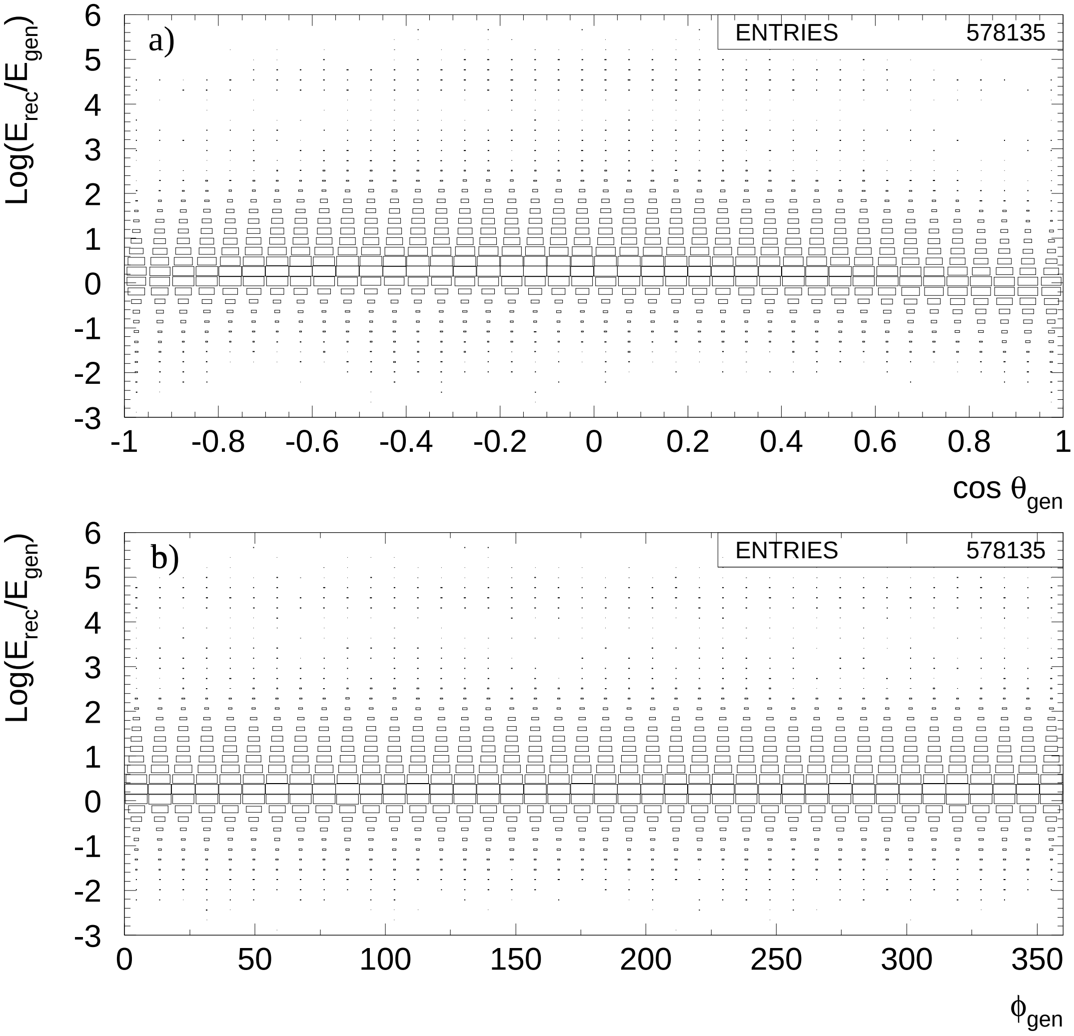

Figure 5.8: Plot (a) shows reconstructed energy spread as a function of true zenith angle of muon (negative values imply up-going), while plot (b) shows the spread as a function of azimuth angle. The excess of events with $\log(E_{\rm rec}/E_{\rm gen}) > 3$ is due to muons which suffered very large energy loss in a single shower.

misreconstruction[‡‡] since a large shower over a shorter path length through the detector can completely obscure the fact that it was generated by a lower energy muon. In essence, a muon would present itself to the detector in short lived, but successful high energy disguise.

[‡‡] In Figure 5.8(a), one can see the fewer events reconstructed with $\log(E_{\rm rec}/E_{\rm gen}) > 3$ near up and down vertical directions.

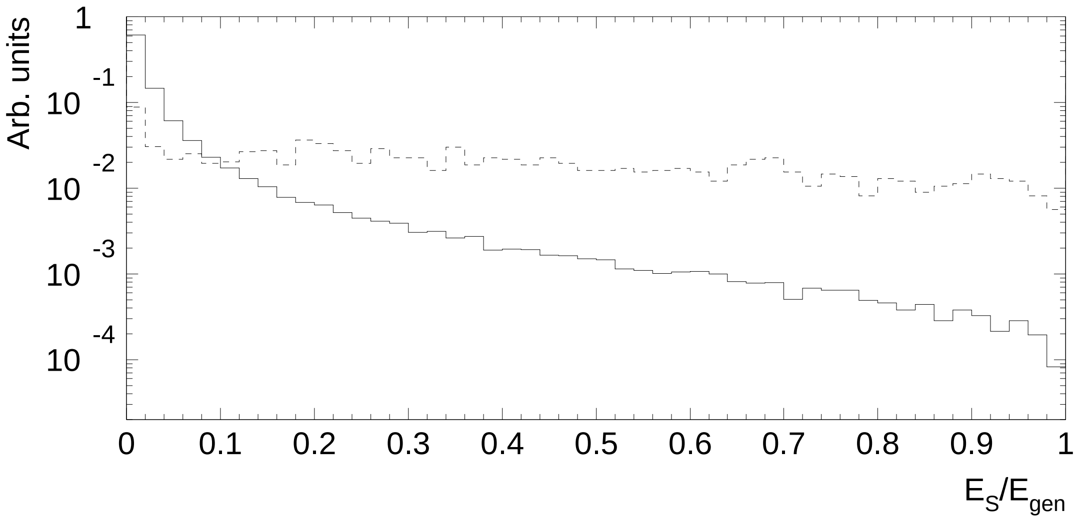

Figure 5.9: Distributions of ratios of the largest shower energy to the initial muon energy for well reconstructed events (solid) and events misreconstructed by more than three orders of magnitude higher than the true energy (dashed). The histograms are normalized to the same area.

Impact parameter and $N_{\mathrm{OM}}^{\mathrm{hit}}$ dependence

The quality of the reconstruction is independent of muon distance from the detector center (Figure 5.11a). As long as the correct trajectory is known, the reconstruction quality does not suffer from the fact that an event only samples a subsection of the detector. This should come as no surprise, since the reconstruction technique designed for through-going muon measurement inherently relies only on a fraction of the total light emitted by the muon during its lifetime to correctly reconstruct its energy.

Figure 5.11(b) shows the weak dependence of the quality of the reconstruction on the total number of hit OMs. The resolution of the reconstruction is slightly worse for events with less than 25 hit OMs. It can be safely assumed that the majority of these

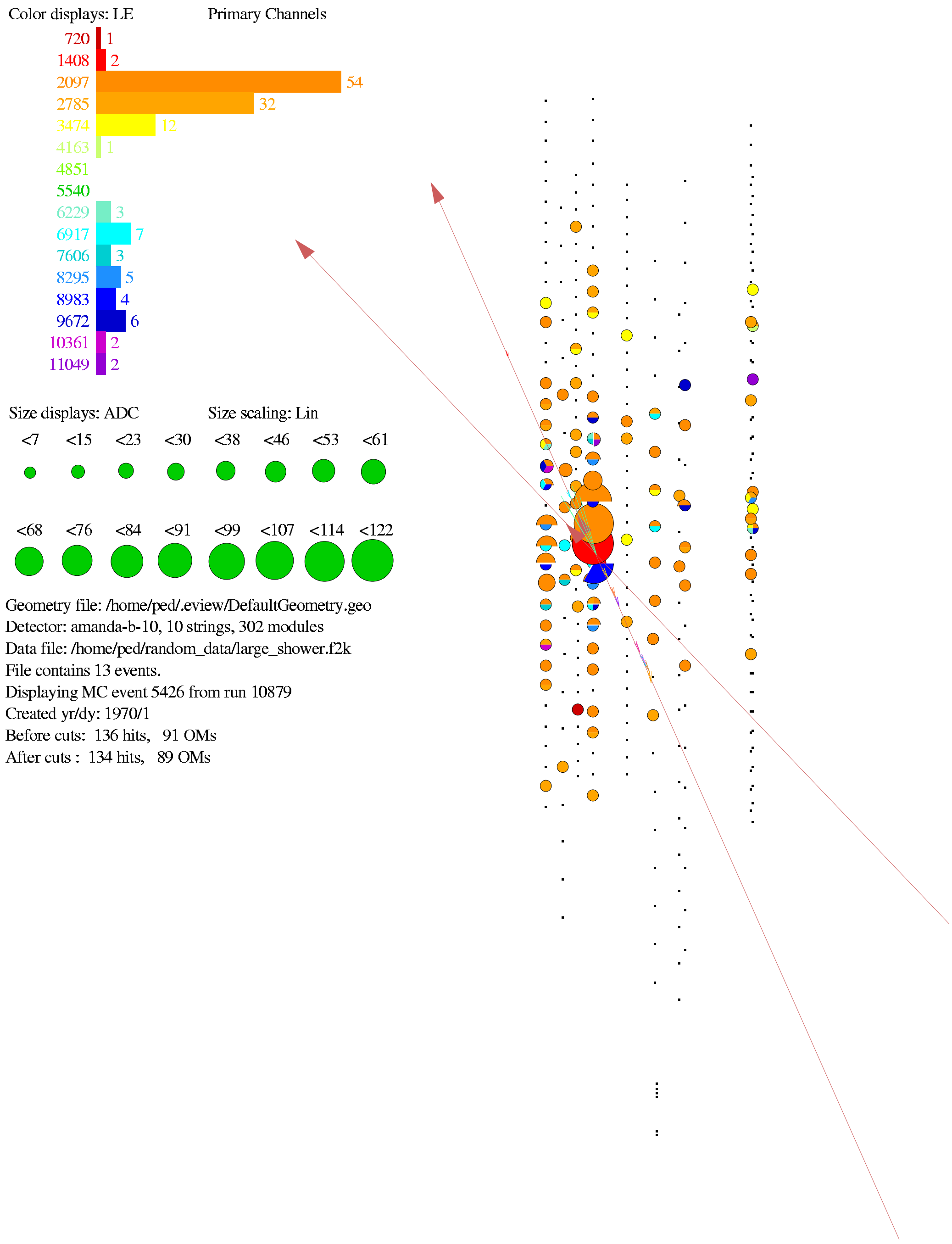

Figure 5.10: An example of a MC event with large energy loss in the center of the detector. More vertical true track experiences large shower loss (green), causing misreconstruction of both direction and energy.

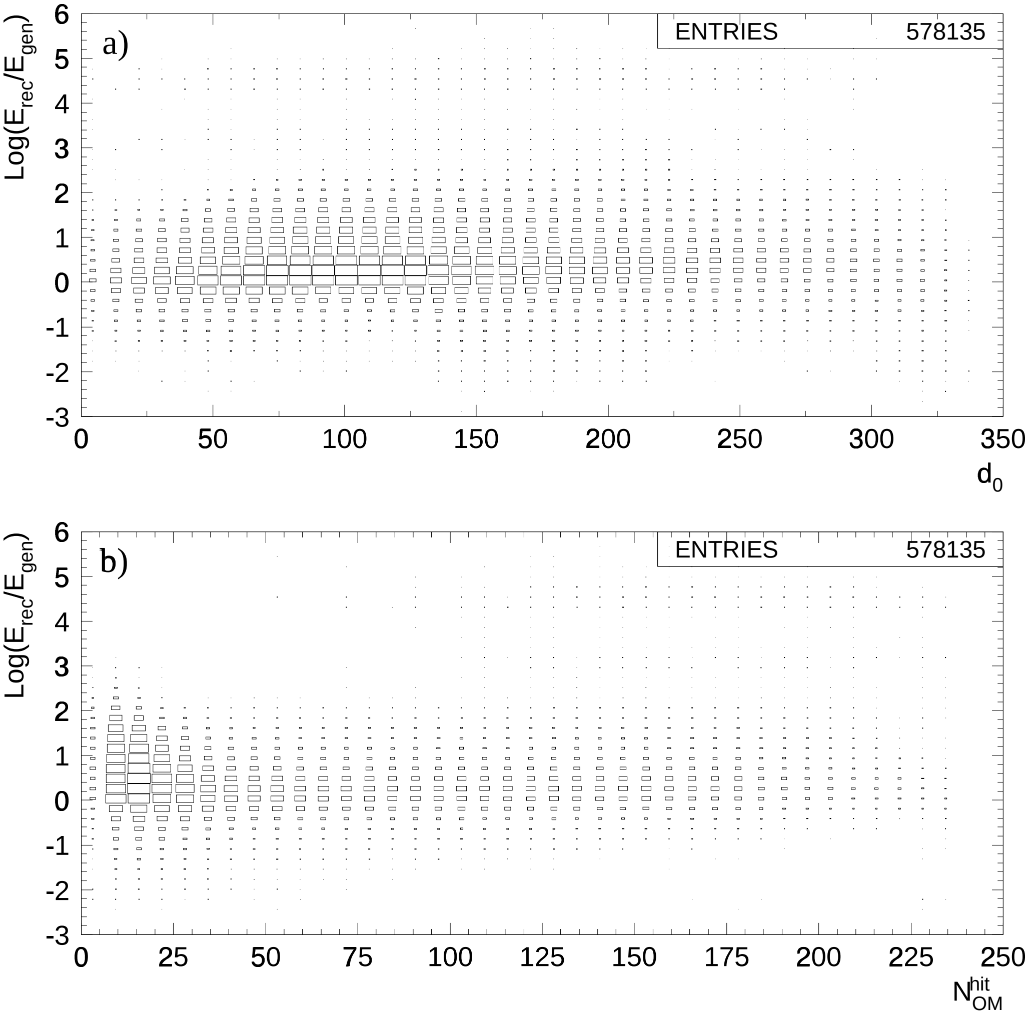

Figure 5.11: The reconstructed energy spread as a function of: a) muon impact parameter, the closest approach to the detector center; and b) the number of hit OMs.

events were generated by lower energy muons, which are expected to have worse resolution of energy reconstruction (see Figure 5.1).

5.2.3 Physical limits of the energy resolution

Before any kind of measurement of particle energy can be made, the particle in question has to transfer some or all of its energy to the detector in the form of some energy

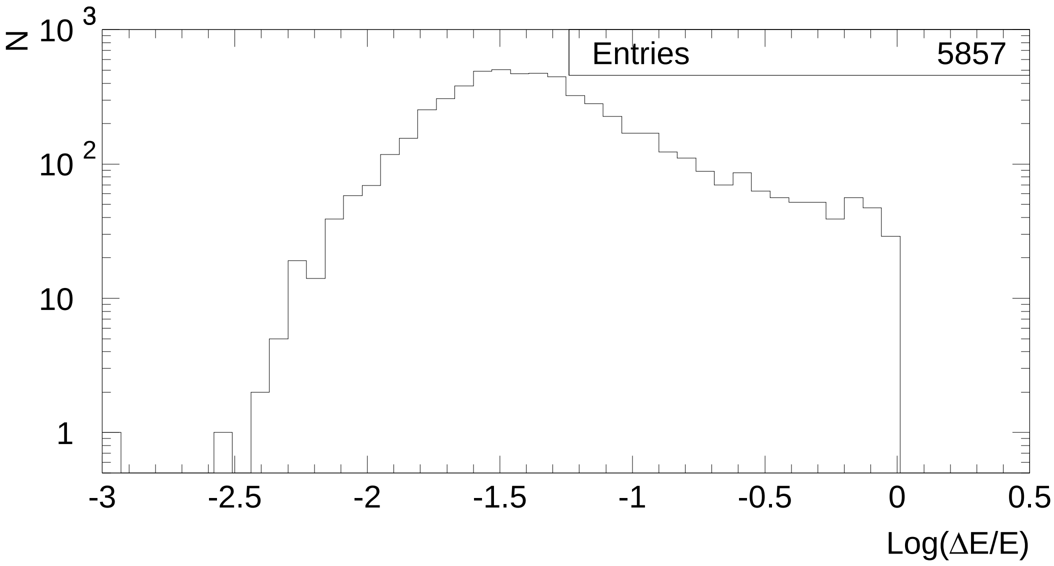

Figure 5.12: The distribution of fraction of energy lost while traveling through the active detector volume by all muons in the range 80–100 TeV. The zero value corresponds to muons that have stopped inside the detector.

proxy (e.g., charge, light, heat, etc.). In the present case, the proxy is light proportional to the amount of energy lost by the muon as it travels through the active detector volume.

Based on the fraction of the total energy lost in the detector, the muon events can be separated into two classes: stopping/contained muons and starting/through-going muons. The stopping/contained muons will deposit all of their energy inside the detector, so the limit of the energy resolution will be governed only by the instrumental and analysis precisions. Unfortunately, the effective collection volume of AMANDA-B10 for these types of events is small, and they constitute a small fraction of all detected events.

The physical limit on energy resolution for starting/through-going muons is set by the variations in energy loss as these muons propagate through the detector. Figure 5.12 shows the variation of the fraction of energy lost by 80–100 TeV muons as they pass through

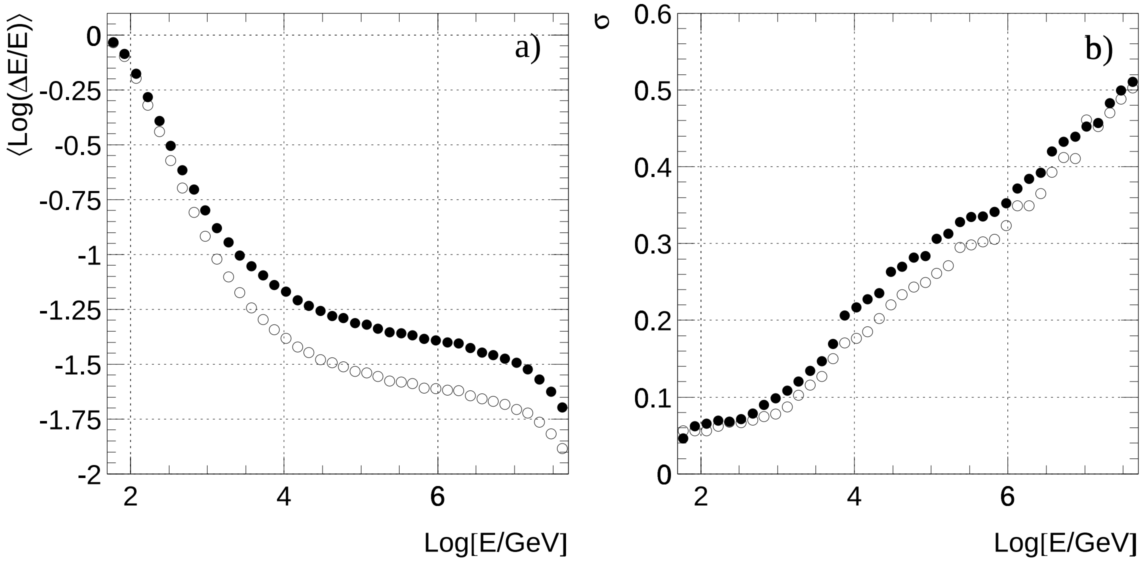

Figure 5.13: Plot a) shows the mean fraction of energy lost as a function of initial muon energy for all muons (solid) and ones which suffer no single-point loss greater than 1.5% of the initial energy (open). Plot b) shows the width of the Gaussian fitted to the peak of the energy loss distribution.

AMANDA-B10. A Gaussian fit to the distribution peak has $\sigma = 0.29$ in $\log E$. Events with very large energy losses – usually in form of a single large shower – constitute the non-Gaussian tail of the distribution.

Figure 5.13 shows the mean relative energy loss and its variation for through-going muons in AMANDA-B10 as functions of the initial muon energy. As expected, the mean energy loss is roughly constant below a few TeV, and it becomes more proportional to energy at higher initial energies (see Figure 2.5). The downturn in the mean energy loss for muons above 10 PeV is due to the photon cutoff present in the detector simulation which affects very energetic events; due to computational speed and size limitations, at most 2000 photons were recorded per OM. The mean energy loss and its variation are lower for muons which experience no large single-point losses. This fact could be used to improve the energy resolution of some experimental subsamples (see the next section).

5.2.4 Muon energy resolution

The quality of the energy reconstruction is very dependent on the true energy of a muon. Figure 5.14 compares the energy resolution and the reconstruction accuracy as functions of true muon energy for the reconstruction presented in this work (referred in the following as method A) and the one currently used by the AMANDA collaboration (method B) [43]. The figure is very rich in information and it requires a thorough discussion. The first thing that strikes the eye in plot (a) is the mean over-prediction of the true energy, especially for muons with $E < 1$ TeV. The over-prediction is attributed to differences in light tables used to generate MC data and tables used for energy reconstruction, as discussed in Section 5.2.1. This can be verified by comparing with Figure 5.4. The effect of using different tables can be accounted for by an unfolding technique which will be applied to the final muon energy spectra (see Section 5.3). The similarity in shapes between Figures 5.13(a) and 5.14(a) is provocative and should be investigated if it persists after the issue of light table difference is resolved. The origin of the downturn in the mean energy resolution at 10 PeV is a simulation artifact discussed in the previous section. The reconstruction accuracy of method B (see plot b) is strongly dependent on the true muon energy; the accuracy at $\log(E_{\text{rec}}/10\text{ TeV}) \approx 0$ has been fixed by the reconstruction algorithm [86]. Method B also uses some non-physical assumptions about light emission [87] which prevent its results from being suitable for use with the unfolding technique.

A comparison of up- and down-going samples reconstructed with method A shows that down-going events have slightly worse energy resolution (see plot c). This is due to the

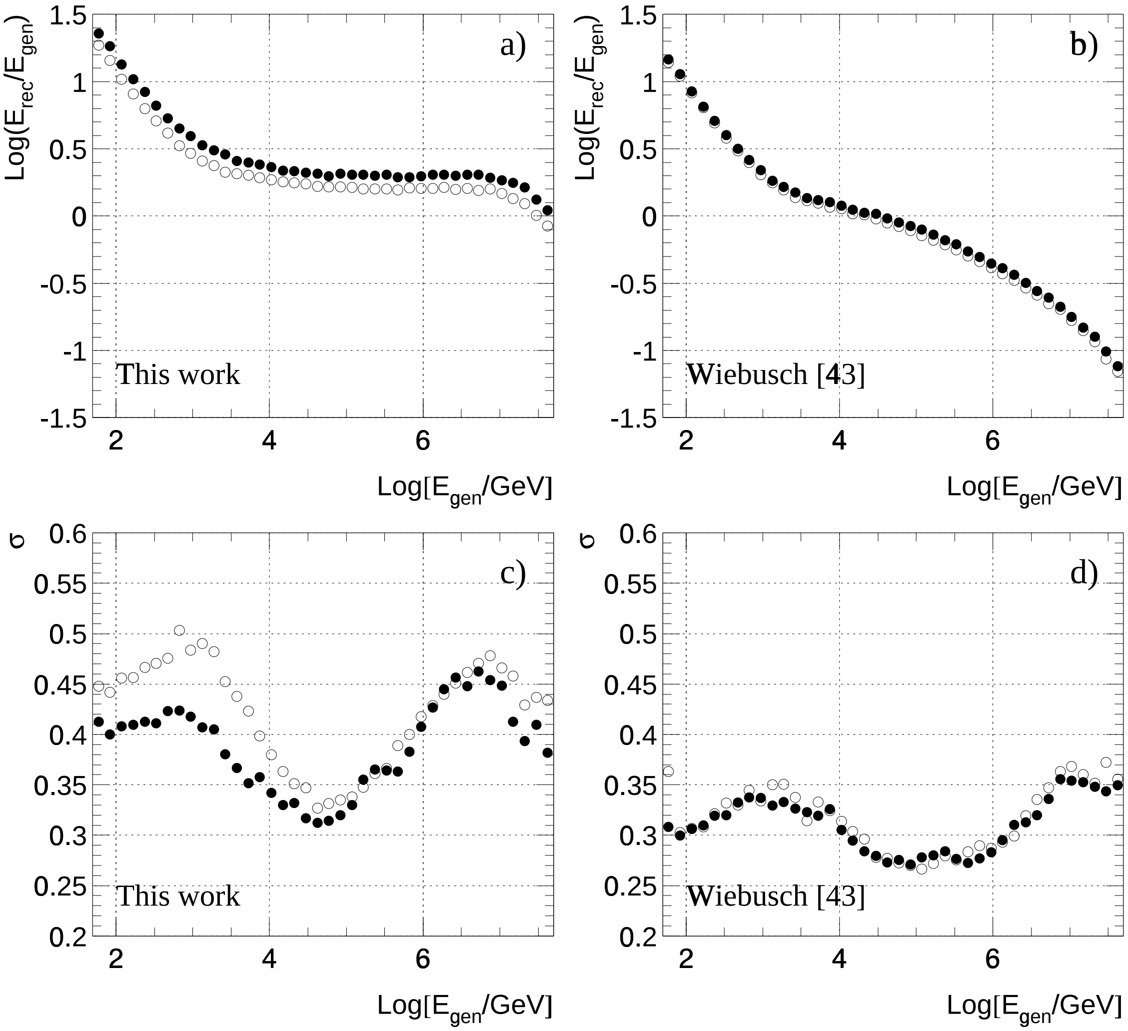

Figure 5.14: Top: The mean difference of reconstructed and true muon energies in (a) this work (method A) and (b) using technique from Wiebusch [43] (method B) as a function of true muon energy. Solid points are for up-going events and open circles for down-going events. Bottom: The energy resolution of the reconstruction using the same symbols for (c) this work and (d) Wiebusch.

fact that the majority of AMANDA OMs are down-looking, so the light collection efficiency for down-going muons, i.e., when light predominately propagates down the detector, is reduced. In turn, this causes larger variations in number of hits recorded by OMs. The up-down difference in the reconstructed energy accuracy of method A (see plot a) is also attributed to the discrepancy in light tables, particularly in the treatment of up-down asymmetry. The reconstruction method B uses a light distribution model which has been fine-tuned to approximate the light tables used in the data simulation, so there is no up-down effect in reconstruction accuracy or resolution [43, 86].

The energy resolution as function of energy in plots (c) and (d) has a complex shape which can be explained by three simple conjectures. Below 1 TeV the amount of light emitted by muons is only weakly dependent on its energy (see Figures 2.9 and 5.1), resulting in the low energy resolution. Above 1 TeV, the dependence becomes linear and the resolution improves. With increasing muon energy, the phase space available to variation in energy loss within the active detector volume also increases, raising the lower limit of resolution (see Figure 5.13b). At approximately 100 TeV, energy loss variations start to dominate the resolution. Again, the final downturn at 10 PeV is due to the simulation artifact discussed before. Comparing plots (c) and (d), the lower resolution of method A indicates that it is more sensitive to variations in the energy loss at lower muon energies. The fact that the resolution of method B (see plot d) at $E \gtrsim 100$ TeV is better than the physically allowed lower limit (see Figure 5.13(b), solid points) means that the energy response saturation for method B has occurred and only a lower limit on the muon energy can be placed.

Large shower effect

As pointed out earlier (see Section 5.2.2), large showers degrade the muon energy resolution. In the case where large showers are present, a large amount of light is generated at a single point, which makes the muon appear brighter than average. Depending on

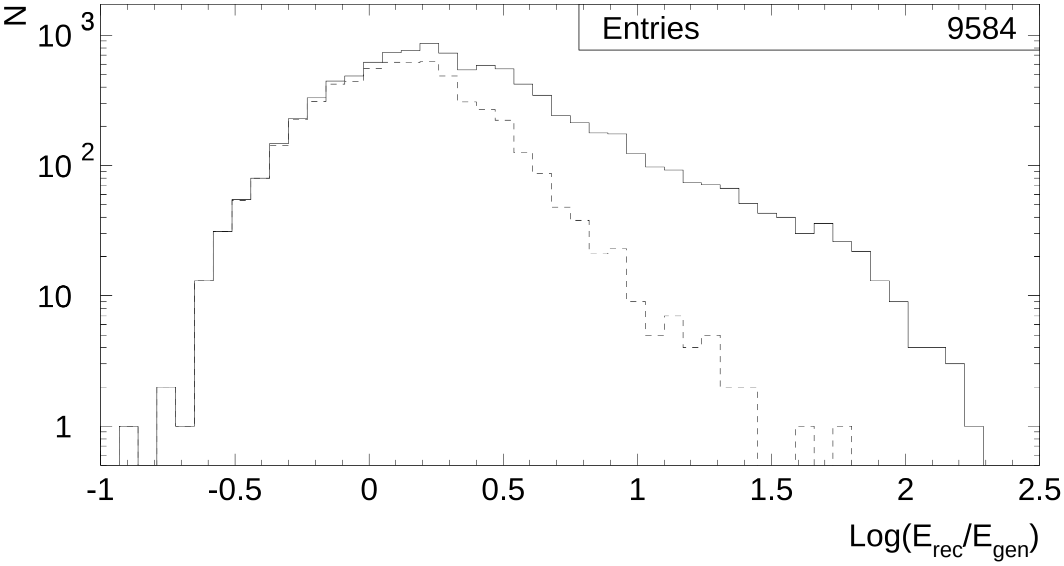

Figure 5.15: The difference in reconstructed and true energies for all muons between 80–100 TeV (solid) and those with no shower larger than 1.5% of the initial muon energy (dashed).

the exact details of event geometry, this temporary brightening can cause the event to be reconstructed with higher energy. Figure 5.15 compares the energy resolution of all events between 80–100 TeV and those in the same energy range but with no shower larger than 1.5% of the initial muon energy. The exclusion of large showers produces a Gaussian resolution with $\sigma = 0.26$, while the loss of well reconstructed events is minimal. With a larger detector, like the proposed IceCube [88], it would be possible to reject these large shower events using topological observables.

5.2.5 Effects of detector electronics and directional reconstruction

The quality of the energy reconstruction is reduced by effects of detector electronics (e.g., PMT saturation, ADC saturation, pulse overlap, etc.) and by muon track directional misreconstruction. This can be seen in Figure 5.16 where the solid histograms show reconstructed energy resolution with complete knowledge of track trajectory and amount of light detected. The dashed histograms use the reconstructed track trajectory, but the true amount of light, while the dotted histograms use light information "measured" by the detector readout simulation. The overall effect of directional misreconstruction is a systematic reduction in reconstructed energy. This can be attributed to the fact that the directional reconstruction algorithm pulls muon trajectories closer to the center of the detector and towards each individual detector string (Figure 5.17). The pattern visible in the figure cannot be attributed to the effect of the AMANDA majority trigger. The same contour plot made with the use of true muon tracks shows a radially symmetric pattern with a single peak at the exact detector center. This systematic effect will automatically result in a lower reconstructed energy, since the energy reconstruction hypothesis would require the muon to emit less light in order to achieve the recorded light intensities. A further reduction in reconstructed energy stems from detector pulse readout inefficiencies which cannot be fully accounted for by data calibration (see Section 4.2).

The large excess of muons reconstructed with too low energy (more than three orders of magnitude) in Figure 5.16(a) is due to events with large errors in reconstructed track trajectories. This is evident by comparing to Figures 5.16(b – d) which all require a direction reconstruction quality cut. The misreconstructed energy of these events is from 30–100 GeV, which is the characteristic energy of muons with a range on the order of the AMANDA length scale (several hundreds of meters). The observed light distribution surrounding an incorrectly reconstructed muon trajectory is often incompatible with the

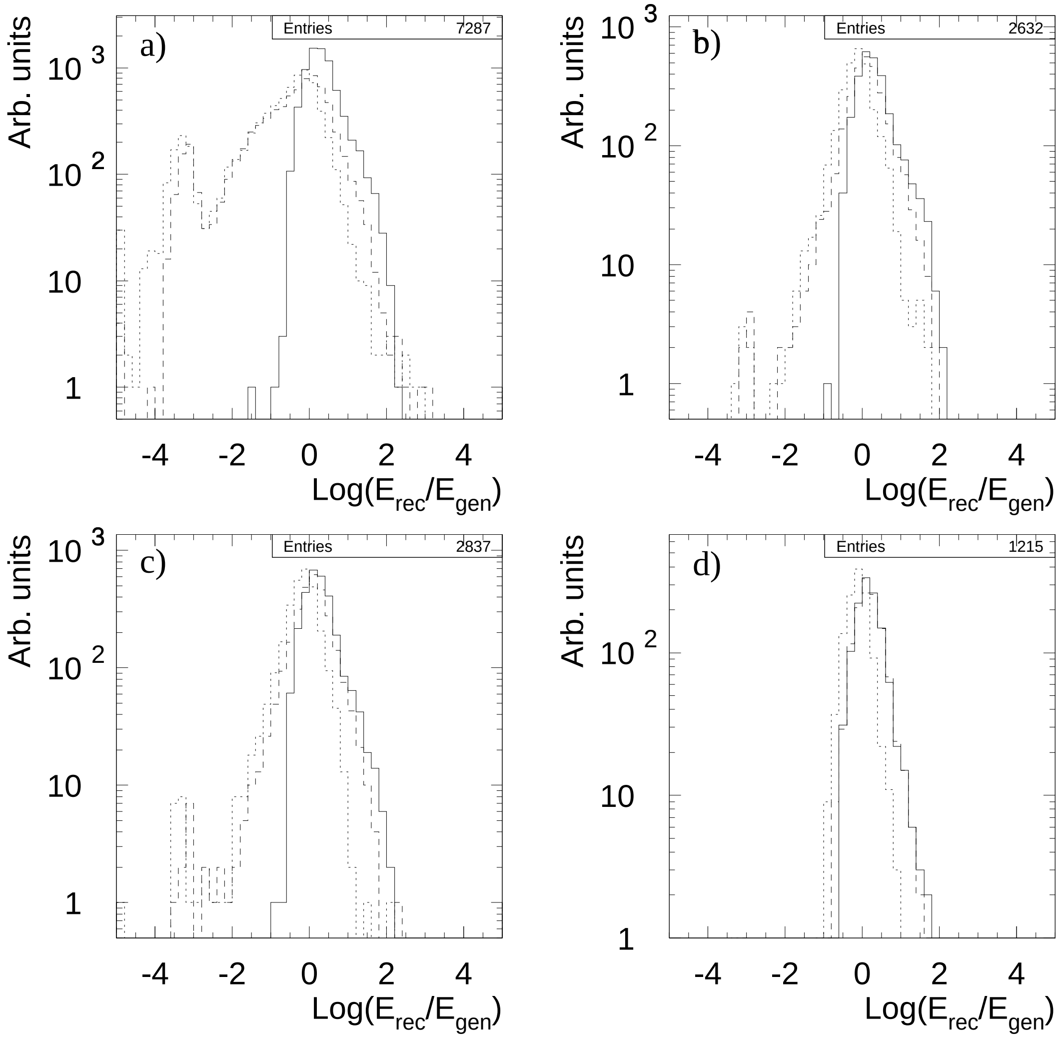

Figure 5.16: In all plots the difference between reconstructed and true muon energies is shown: when the true track trajectory and the true amount of light recorded is used (solid), the reconstructed trajectory and the true amount of light is used (dashed), and the reconstructed trajectory and the "measured" amount of light is used (dotted). Plot (a) shows energy resolution for all events in the 80–100 TeV range. In plot (b), the cut $\ln(RML) < -4.5$ is applied to the energy fit using the reconstructed trajectory. In plots (c) and (d) the requirement that the zenith and azimuth directions have been correctly reconstructed to within 30° and 5°, respectively, is imposed.

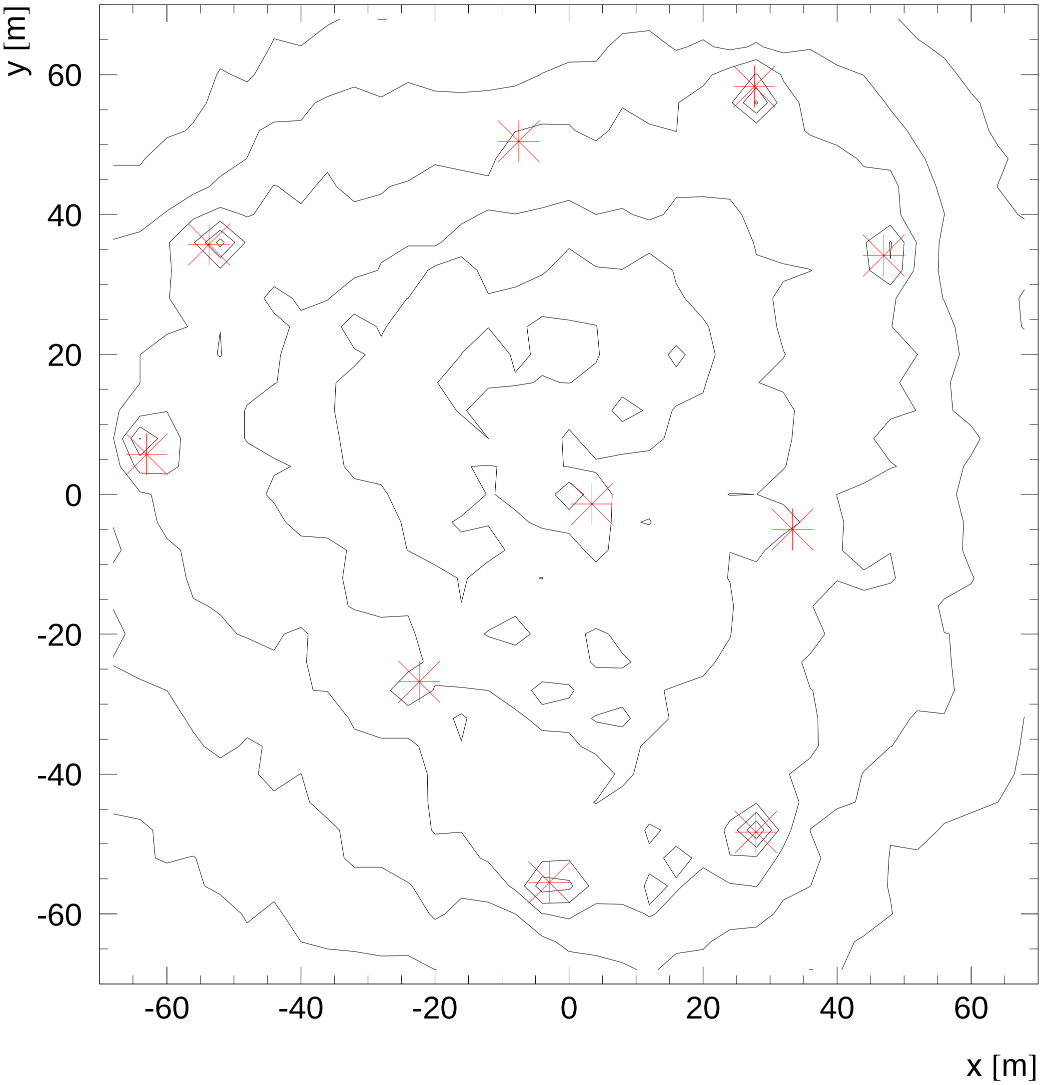

Figure 5.17: Contour plot of reconstructed muon track x and y coordinates of the closest approach point to the detector center. No event selection has been made. Positions of strings are marked by red cross-hairs. The enhancements are obvious around the detector center and most of the strings.

light distribution expected around a muon. If such misreconstructed trajectory implies that the muon should have traveled through a region of the detector where no light was observed, the energy reconstruction algorithm will assume that the muon has decayed soon after entering the detector and will assign it a low energy.

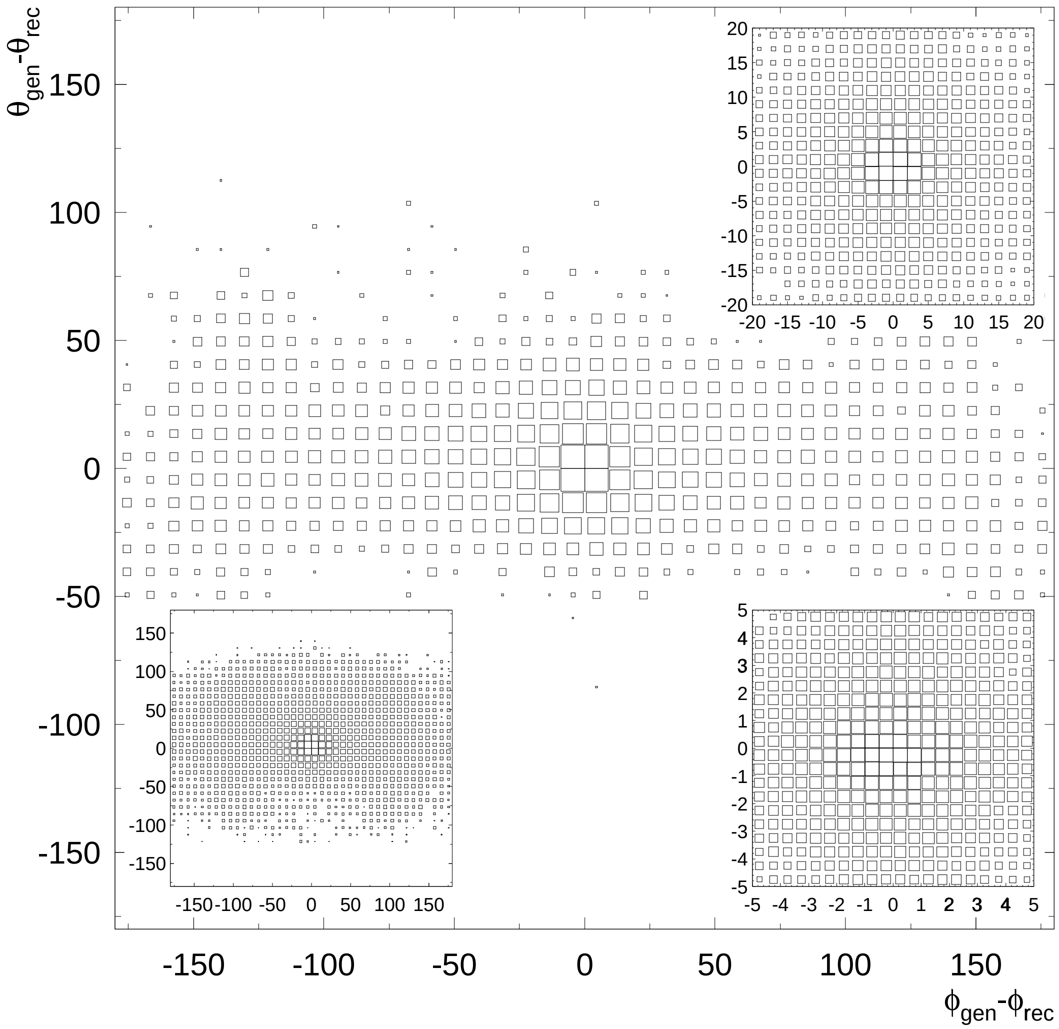

Figure 5.18: The difference between true and reconstructed zenith and azimuth directions for events satisfying $\ln(RML) < -4.5$ in the 100 GeV to 50 PeV range. Insets on the right are enlargements of the central region. The inset on the left is the same plot but with no quality cut on $\ln(RML)$.

Encouragingly, the correlation between the quality of the energy fit (through the $\ln(RML)$ parameter) and the accuracy of the directional fit (Figure 5.18) offers a possibility for the use of the energy fit as a quality parameter in muon directional analyses (for example see Figure 5.19).

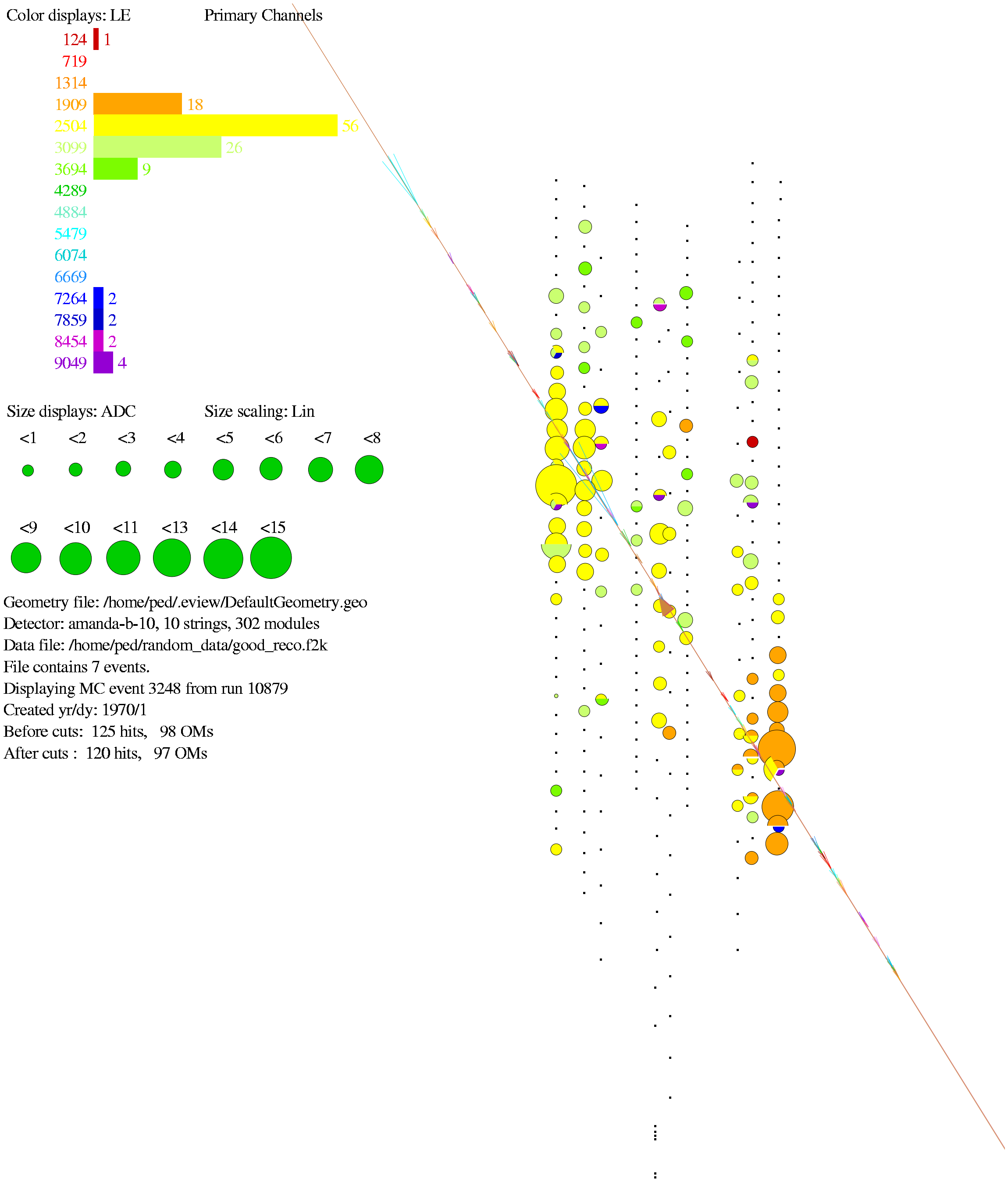

Figure 5.19: An example of a well reconstructed MC event which was selected by the energy fit quality parameter. A smooth energy loss along the track passing close to two strings ensures excellent direction and energy reconstructions. The reconstructed track perfectly overlies the true track, and the energy (6.1 TeV) was reconstructed as well as 0.02 in $\log E$.

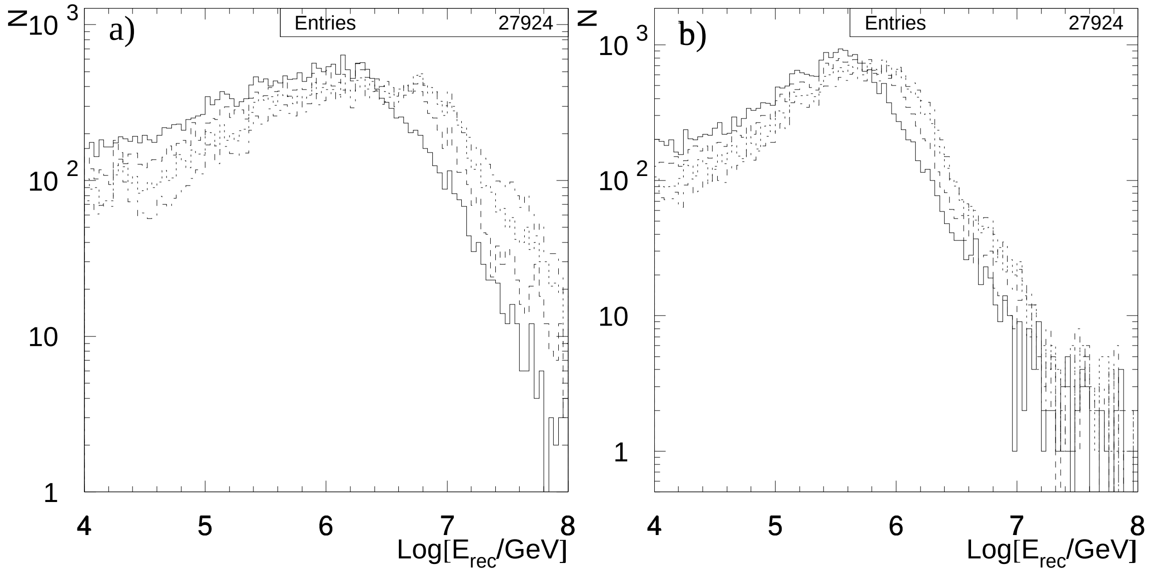

Figure 5.20: The effect of electronics saturation on the energy reconstruction. Plot a) shows muon energies reconstructed using the true amount of light detected for four true muon energy ranges, $\log(E_{\mathrm{gen}}/\mathrm{GeV})$: 6–6.4 (solid), 6.4–6.8 (dashed), 6.8–7.2 (dotted), and 7.2–7.6 (dot-dashed). Plot b) shows the same for muon energies reconstructed using the "measured" light amount. The quality cut $\ln(RML) < -4.5$ was applied to all events.

PMT and electronics saturation

The light output from the most energetic muons ($E > 1$ PeV) exceeds the dynamic range of AMANDA in terms of energy resolution. Figure 5.20 shows the reconstructed energies for muons above 1 PeV with a quality cut on directional reconstruction of $\ln(RML) < -4.5$. Comparing the two plots, the pile-up of reconstructed energies below 1 PeV is visible in plot (b). What little resolving power between histograms is visible in plot (a) is gone in plot (b).

5.3 Unfolding the energy distributions

As mentioned before, applying a probabilistic energy reconstruction model to a highly stochastic process of muon detection limits the event by event resolution of such reconstruction to the width of the distribution of the stochastic variations, primarily in the total amount of muon energy deposited in the detector. However, since the underlying physics of these stochastic processes is known, their effect on the *whole* data set can be modeled.

Similarly, the quality of muon track directional reconstruction affects the accuracy of energy reconstruction. As shown in the previous section, the directional reconstruction systematically biases the muon trajectory to certain portions of the available phase space. While this fact might not be crucial for neutrino or muon integral flux measurements, it affects the quality of muon energy reconstruction. The assumption made in this work that all muons originated outside of the AMANDA active volume further degrades the quality of the energy reconstruction. These systematic biases in trajectory and vertex location can also be modeled and corrected for.

Furthermore, as discussed in Section 4.2, there is a loss of information in the detector electronics about the true number of photons detected by the OMs. This systematic loss can also be modeled by simulating the detector response for various input photon fluxes.

A technique that can be used to correct for stochastic variations, directional bias, and information loss, and in addition to sidestep some issues arising from the application of experimental data quality criteria[†], is Bayesian unfolding [89]. Bayesian unfolding takes

---

[†] Due to issues of a technical nature, during data cleaning some information is removed from the events without the ability to successfully communicate that fact to the energy reconstruction algorithm.

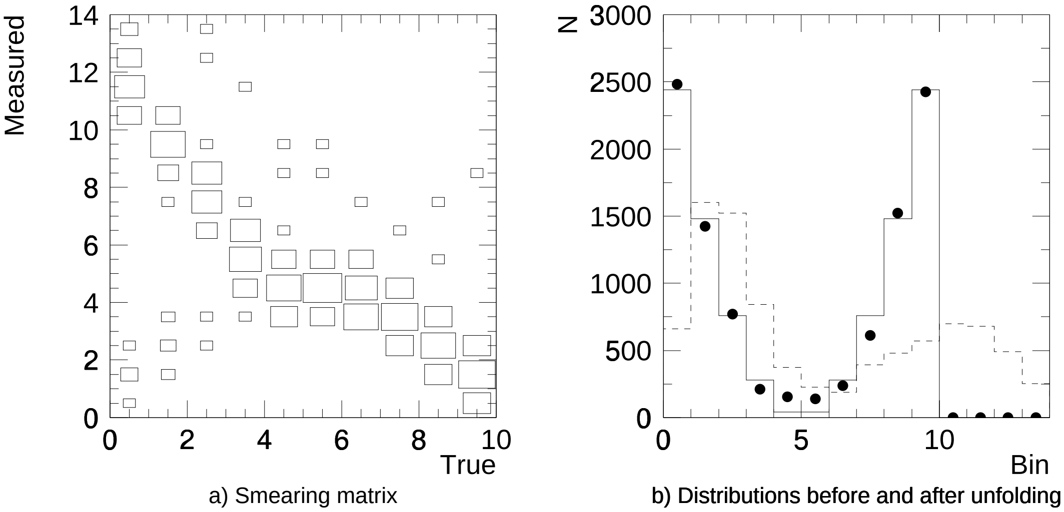

a) Smearing matrix

b) Distributions before and after unfolding

Figure 5.21: An example of Bayesian distribution unfolding. Plot (a) shows the smearing matrix between true and measured values. The smearing matrix can be either calculated analytically or determined by Monte Carlo simulation. Plot (b) shows the true (solid) and measured (dashed) distributions which are related through the smearing matrix. The unfolded distribution generated by Bayesian unfolding is overlaid as solid points. Figure adapted from [89].

some modeled relationship between true and observed values of some variable, called *the smearing matrix*, and tries to construct the true distribution out of the observed one based on that relationship (Figure 5.21). Unfolding has been a technique used in high energy particle physics for several decades [90, 91], and recently it has been used in analysis of the AMANDA atmospheric muon data [92, 93]. Since the unfolding correction is performed on distributions and not on an event by event basis, it has to be re-applied for each subset of data analyzed. Thus, to create an appropriate smearing matrix, analogous to experimental, and signal and background MC data, the data set used to generate the smearing matrix has to go through all the steps of data quality selection (see Section 6.2).

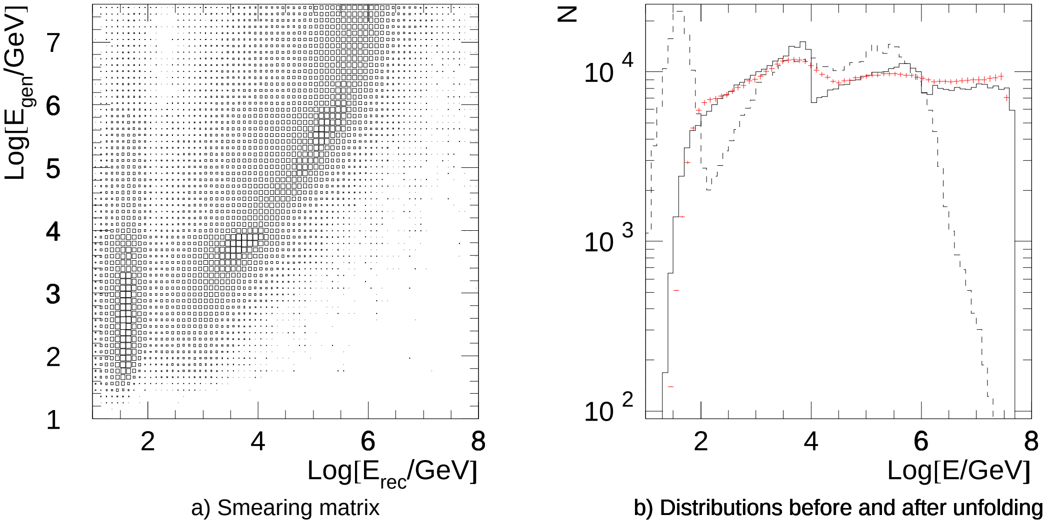

a) Smearing matrix

b) Distributions before and after unfolding

Figure 5.22: Unfolding of energy spectrum of the calibration data set. The smearing matrix (a) shows the obvious saturation effect above true muon energy of 1 PeV. In plot (b), true energy distribution is solid, reconstructed is dashed, and unfolded is given by red points. See text for discussion.

5.3.1 Unfolding the calibration set

The calibration data set will be used as a training set for the smearing matrix needed for Bayesian unfolding of energy spectra. As an example, one half of the calibration set was used to generate the smearing matrix (Figure 5.22a). The second half was then used for the reconstructed energy distribution to be unfolded (Figure 5.22b); the solid line gives the actual energy distribution of the calibration sample, the dashed line is the reconstructed energy distribution, and the red points are the unfolded energy distribution. The errors on the unfolded spectrum are only statistical and no quality cuts were made on the calibration set events in this example. As expected, the large smearing introduced by energy reconstruction causes the sharp features of the calibration set not to be accurately reproduced. However, the overall agreement is substantially better than before unfolding.

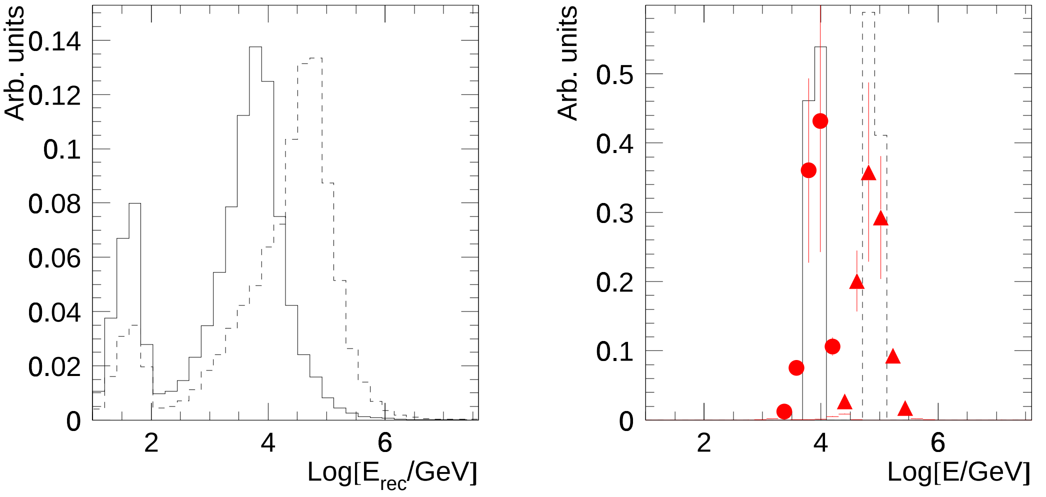

a) Reconstructed energy distributions

b) True and unfolded energy distributions

Figure 5.23: The reconstructed energy spectra (a) of two muon fluxes with narrow energy distributions (b). The unfolded distributions are shown as red points with statistical error bars. The calibration set with no quality cuts has been used for generation of the smearing matrix and all of the distributions.

5.3.2 Mono-energetic flux unfolding

Due to strong energy smearing, the most challenging distribution to unfold would be a delta function-like energy spectrum. As Figure 5.23 shows, a satisfactory unfolding can still be achieved. Two isotropic energy fluxes with FWHM of only 0.2 in $\log E$ centered at $\log E = 3.9$ GeV (solid) and $\log E = 4.9$ (dashed) were reconstructed (Figure 5.23a). The reconstructed spectra FWHMs are ~1.3 in $\log E$ in both cases. After unfolding, the agreement with the true distributions (solid and dashed histograms in Figure 5.23b) is improved. The FWHMs of the unfolded distributions are 0.4 and 0.5 in $\log E$ for the low and high energy flux, respectively.

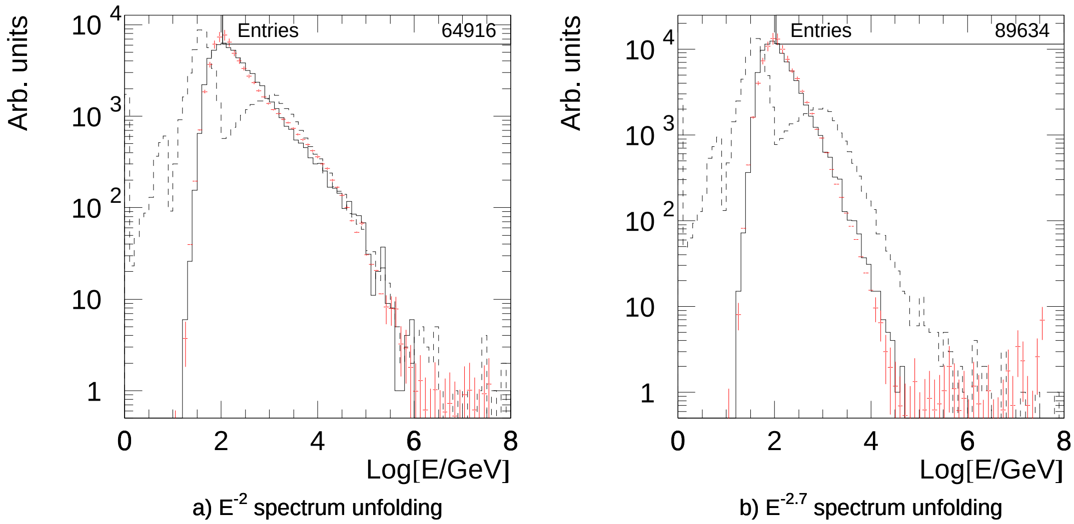

a) E^{-2} spectrum unfolding b) $E^{-2.7}$ spectrum unfolding

Figure 5.24: Examples of power law spectra unfolding. True energy distributions are solid, reconstructed are dashed, and unfolded are given by red points. Only statistical errors are shown. The up-going part of the calibration set with no quality cuts was used for generation of the smearing matrix.

5.3.3 Power law spectrum unfolding

According to theoretical models, the energy distributions of interest in AMANDA will be various power law spectra originating from terrestrial and extraterrestrial sources. The smooth shapes of such spectra present an ideal case for unfolding methods. Large samples of up-going muons with energy spectra $dN/dE \sim E^{-2}$ and $dN/dE \sim E^{-2.7}$ were generated. These events were processed and reconstructed in the same fashion as all AMANDA experimental and simulated data. After unfolding the reconstructed energy distributions, the agreements with the generated energy spectra are encouraging (Figure 5.24). The fractional deviations of the reconstructed slopes are 7.5% and 23%, respectively. Note that the unfolded spectra level off at the points where the number of counts reaches one per bin. This is an intrinsic limit of a procedure that relies on the counting of bin content.

5.4 Summary

In this chapter, the muon energy reconstruction based on the measurement of pulse amplitudes generated by the optical modules has been described. Various checks have been performed on the quality of the energy reconstruction, showing that a good understanding of this technique exists. The comparison with the energy reconstruction currently used by the AMANDA collaboration shows that the method presented here is superior, with better accuracy, resolution, and dynamic energy range.

Due to large stochastic variations in muon energy loss, and thus in light emission, the measurement of the muon energy spectrum is presented as a two step process. First, the most likely energy of each detected muon is determined. After building a distribution of most likely muon energies, it is unfolded to reveal the true underlying energy distribution. In addition to taking into account of stochastic processes, the unfolding step corrects for known systematic effects present in data collection and analysis.

Chapter 6

Results

> *"Son, this is the only time I'm ever*
> *gonna say this. It is* **not** *okay to lose."*
> Homer Simpson, *The Simpsons,*
> *"Dead Putting Society"*, **7F08**

The work presented in this dissertation up to this point was primarily focused on developing methodology and tools for the muon energy reconstruction in AMANDA. To demonstrate the potential of this reconstruction technique, it will be used in this chapter on analysis of atmospheric-neutrino and atmospheric-muon flux measurements. Only the 1997 data set will be used.

6.1 The 1997 data set

Following intense summer construction, the 1997 austral winter saw the first year of AMANDA-B10 operation. The deep 10-string detector was the first stage of AMANDA capable of indisputable neutrino detection [42]. As such, the data collected during 1997 served as the "learning sample" on which to develop different data reconstruction and analysis techniques.

The array was operated with the primary trigger in a 16-fold simple-majority mode. Additional external triggers were also used, allowing for coincident measurements with nearby cosmic ray shower detectors SPASE 1 and 2 [94, 95], and GASP [96]. The data were collected at an event rate of ~100 Hz between February and November 1997. After the removal of data gathered during periods of unreliable detector operation, the total live-time was $1.124 \cdot 10^7$ seconds, or 130.1 days [97]. Following this initial selection, data cleaning, reconstruction, and quality analysis performed here are based on the prescription set by DeYoung [85].

6.2 Atmospheric neutrinos

The 1997 atmospheric-neutrino data sample has several important roles for AMANDA. It is a proof-of-principle for neutrino detection in deep glacial ice, it provides a measure of the angle-dependent detection efficiency of the detector, and it can be used for studies of the cosmic ray flux and cosmic ray shower development in the atmosphere.

In extracting a neutrino sample from the raw data, the major obstacle is reducing an initially overwhelming atmospheric muon background. The primary tool for this is a directional reconstruction analysis, which simply rejects events that reconstruct as having a down-going direction. However, a down-going event can sometimes appear to have an up-going direction due to misreconstruction, detector artifacts, or the coincidence of two down-going events[†].

[†] A muon hits the bottom of the detector, closely followed by another muon that hits the top.

6.2.1 The neutrino sample

The initial 1997 experimental data sample, consisting mostly of down-going muon background, is reduced by six orders of magnitude by requiring that the best fit to an up-going direction is better than the best fit to a down-going direction. This is done in several steps, each computationally more taxing than the previous, leaving 4888 possible up-going atmospheric-neutrino candidates, compared to 685 ± 26 expected events. The final step in the analysis is to extract the most likely neutrino candidates from these remaining events. This is done by statistical evaluation of the space-time topology of the events and by deciding which are the most likely to have been misreconstructed.

The actual variables, description of cut levels, and measurements of sample purity used in the data reduction are described elsewhere [85][‡]. The neutrino sample is purified through data reduction levels which will be numbered from 1 through N. At higher reduction levels, a larger fraction of the remaining events are neutrino induced. The starting set of atmospheric-neutrino candidates will be referred to as level 0. The data at level 7 were used as part of the report on atmospheric neutrino observation by AMANDA [42]. The remaining 182 events at level 7 are estimated to be ~90% atmospheric-neutrino events. Figure 6.1 shows an example of two neutrino-induced events, one reconstructed at high and the other at low energy. Monte Carlo data simulating atmospheric-neutrino and atmospheric-muon background, and reconstruction calibration data set (see Section 5.2) were put through the same data reduction levels.

[‡] The small differences compared to the analysis in [85], e.g., the exact number of data events at each quality level, are due to more conservative treatment of unstable OMs in this work.

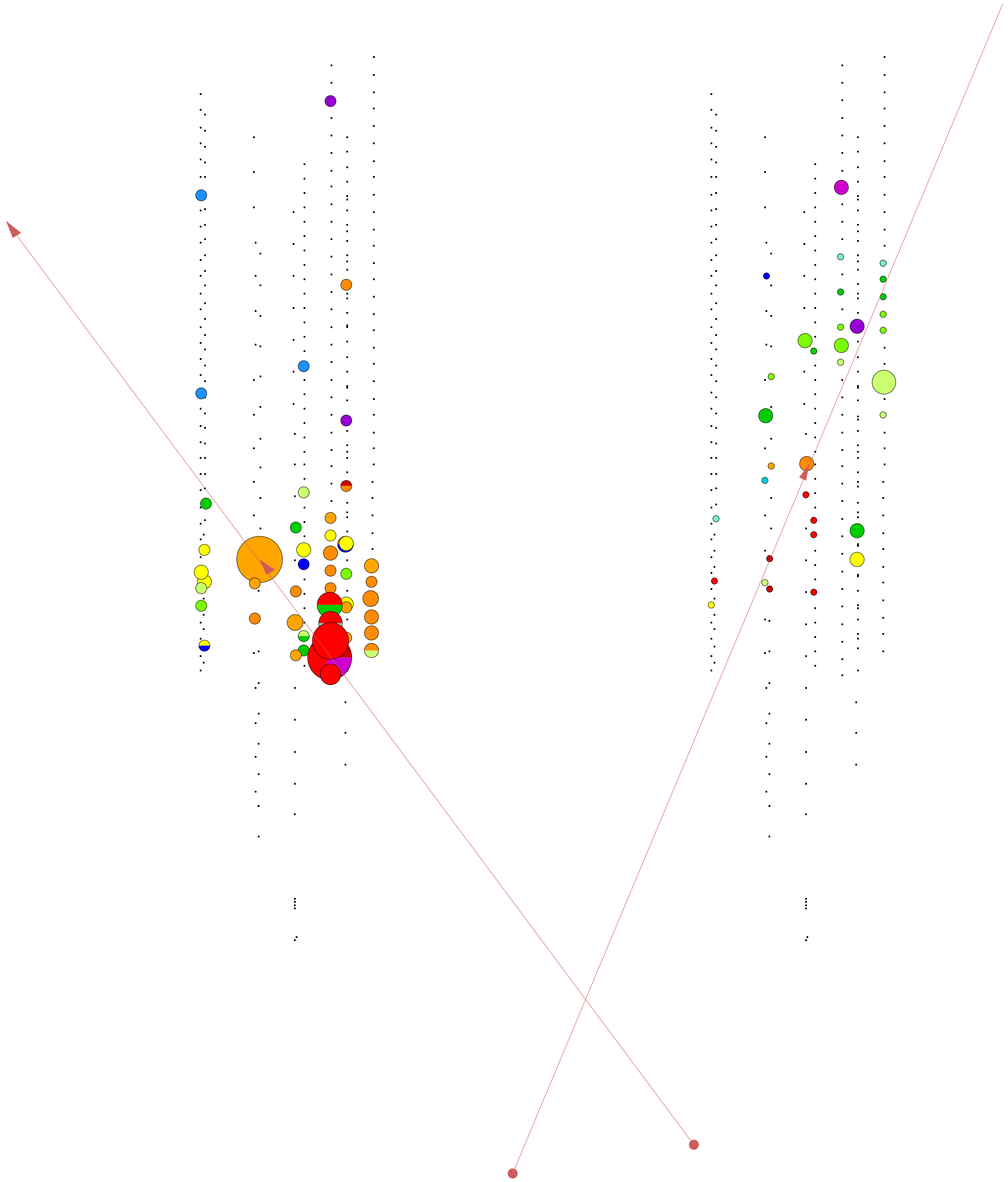

Figure 6.1: Left: Data event reconstructed at 8.3 TeV. Right: Data event reconstructed at 91 GeV. For clarity, the OM hit sizes in two pictures do not have the same size scaling. The largest hit on the left should have a diameter 4.5 times larger than the largest one on the right.

6.2.2 Energy spectrum of atmospheric neutrinos

The reconstructed differential energy spectra of atmospheric neutrinos at levels 1 through 16 have been produced using Bayesian unfolding as described in Section 5.3. The comparison with the atmospheric-neutrino simulation is shown in Figure 6.2. The errors on the data points include statistical errors and an estimate of the uncertainty from unfolding; MC errors are only statistical. The estimate of the unfolding errors was made by varying the first-guess distribution used in the unfolding process. The lower data-quality levels show substantial contamination by a higher-energy, misreconstructed muon background, while the higher levels are consistent with the atmospheric-neutrino prediction apart from overall normalization. Levels 10–12 indicate agreement similar to the one seen at level 9, while above level 12 agreement becomes worse (see Section 6.2.4).

Figure 6.3 shows the ratio of events between data and prediction as a function of quality level. Above the quality level where the majority of misreconstructed background events have been removed (level 7), it would be expected that the ratios in the integral and differential plots stay constant. Also, if only the absolute normalization was wrong, the ratios in the two plots should be the same. Neither is the case. The differential ratio plot indicates that data and prediction are not equally affected by different cut levels, so care should be taken when deciding which quality level to take as representative of the atmospheric-neutrino sample.

The difference in event rates can arise from several sources. The leading candidates are: uncertainties in atmospheric-neutrino flux predictions (∼30% [98]), systematic uncertainties in performance of AMANDA (including detector simulation, ∼15–50 % [97, 99]),

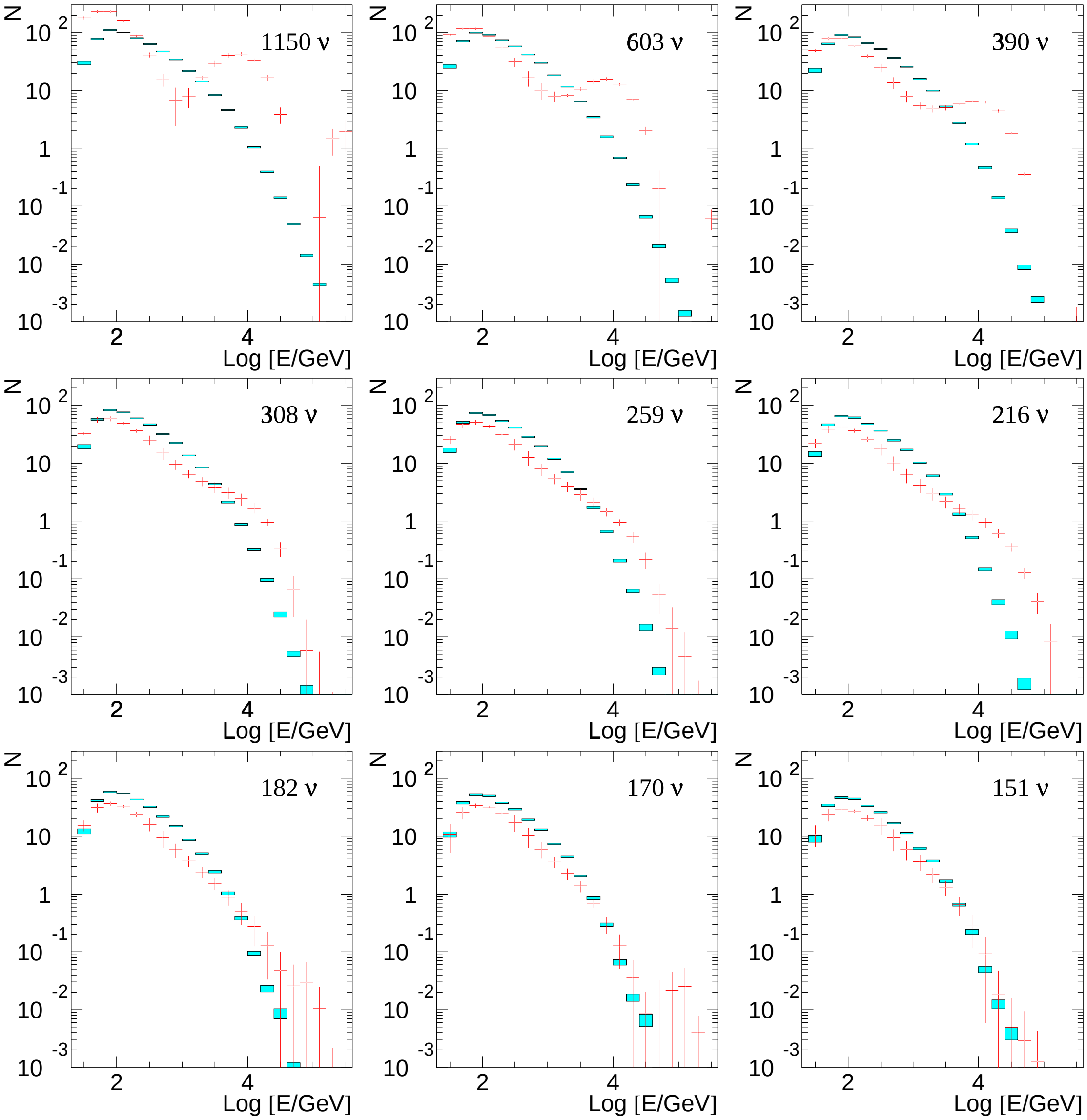

Figure 6.2: Comparison of the measured energy spectrum (red points) with the atmospheric-neutrino MC prediction (cyan boxes). The heights of the boxes correspond to the errors in the prediction. Plots correspond to data quality levels 1 through 9. Numbers indicate the total number of neutrino candidates at each level.

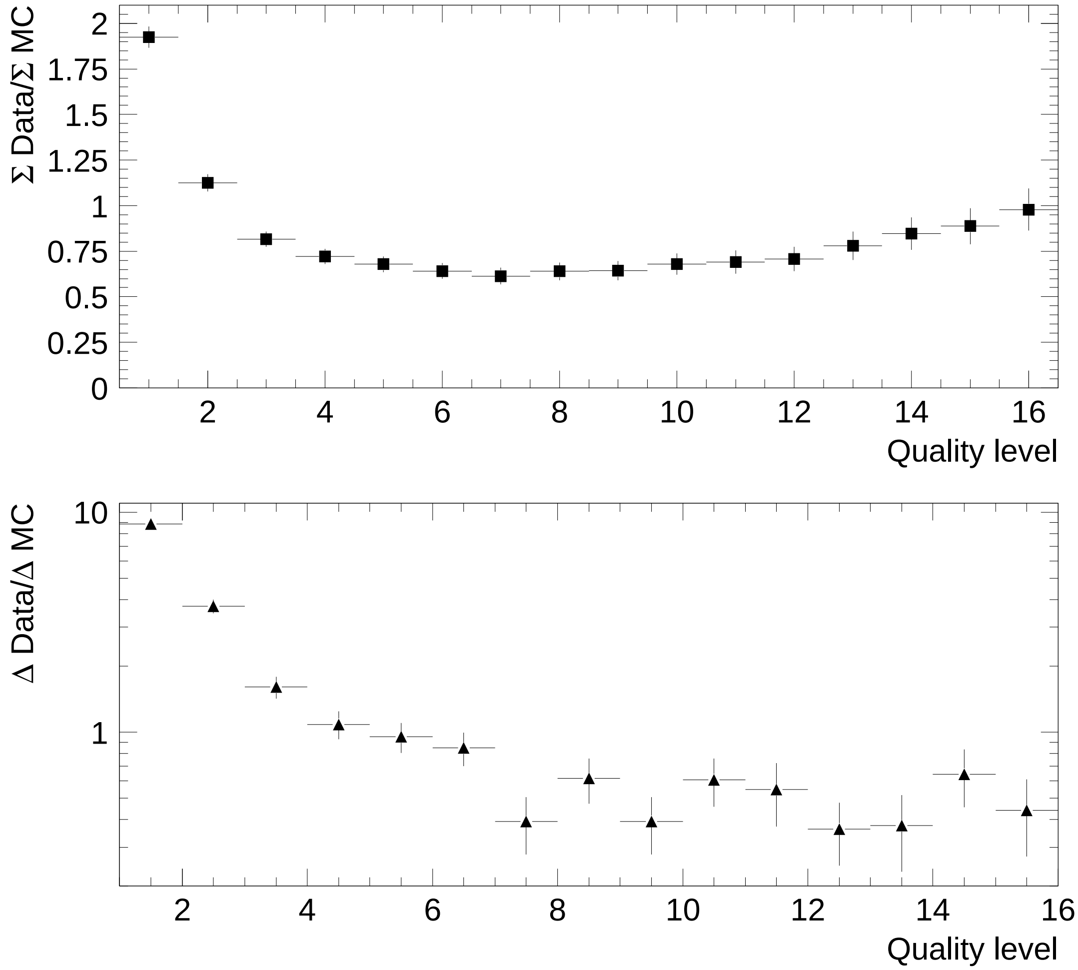

Figure 6.3: Top: Event ratio between data and atmospheric-neutrino prediction for different data quality levels. Bottom: Ratio of change in number of data and predicted events between quality levels.

and the possibility of neutrino-flavor oscillation (see below). The shapes of the energy distributions can be better compared if they are renormalized to the same area (Figure 6.4).

6.2.3 Atmospheric neutrino prediction models

Different models for prediction of atmospheric neutrino event rates observed by AMANDA can be used in Monte Carlo simulation. Several models regarding neutrino gener-

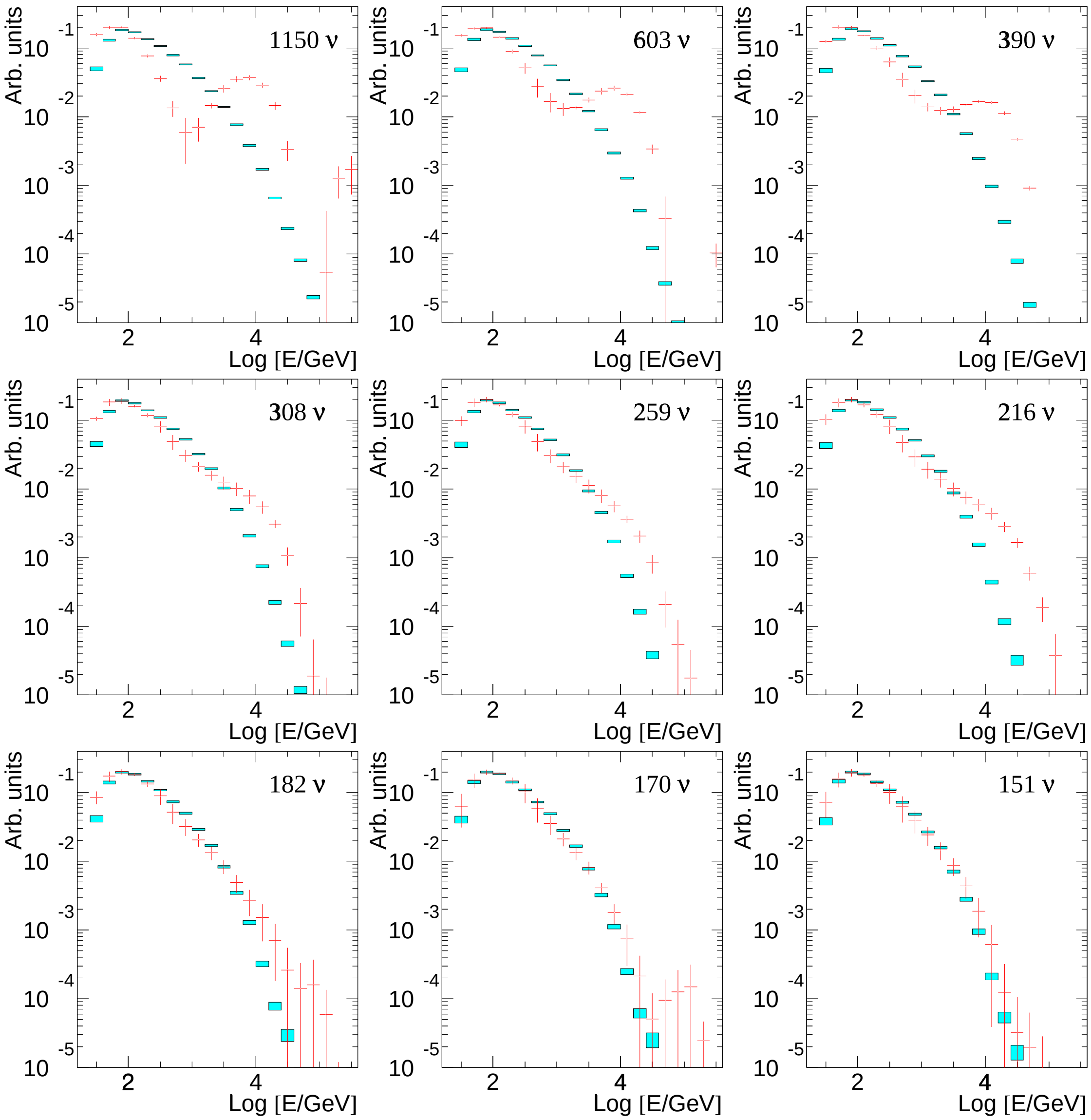

Figure 6.4: Comparison of the renormalized energy spectra of data (red points) and atmospheric-neutrino MC prediction (cyan boxes).

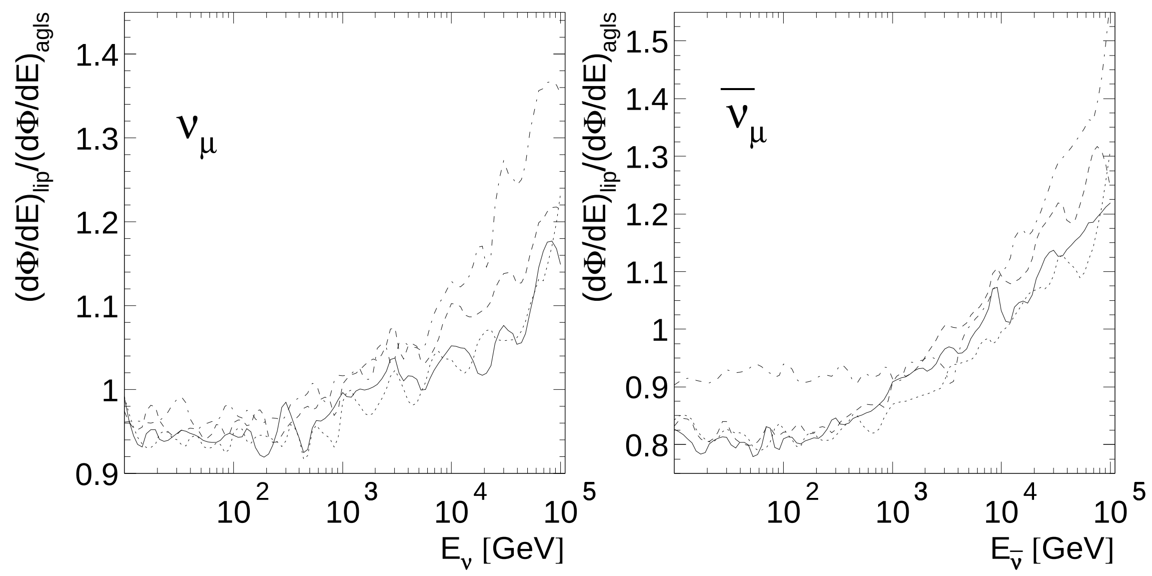

Figure 6.5: Comparison of the two neutrino flux models [100, 101]. The fluxes are compared at zenith directions of 180° (solid), 150° (dashed), 120° (dotted), 90° (dot-dashed). The short scale oscillations are artifacts of interpolation routines, and are present in MC data.

ation in the atmosphere and neutrino-flavor oscillation will be considered here.

Atmospheric flux models

The atmospheric-neutrino flux model that is usually used for the AMANDA atmospheric-neutrino event rate prediction is taken from Lipari [100]. A somewhat different atmospheric-neutrino flux model has been published more recently by Agrawal et al. [101]. The two models differ in treatment of the primary cosmic ray spectrum and development of air shower, and, thus, subsequent production of neutrinos. The atmospheric neutrino fluxes predicted by these two models will be referred to as Φ_{lip} and Φ_{agls}, respectively. Figure 6.5 compares the prediction of ν_μ and $\overline{\nu}_\mu$ fluxes between the models.

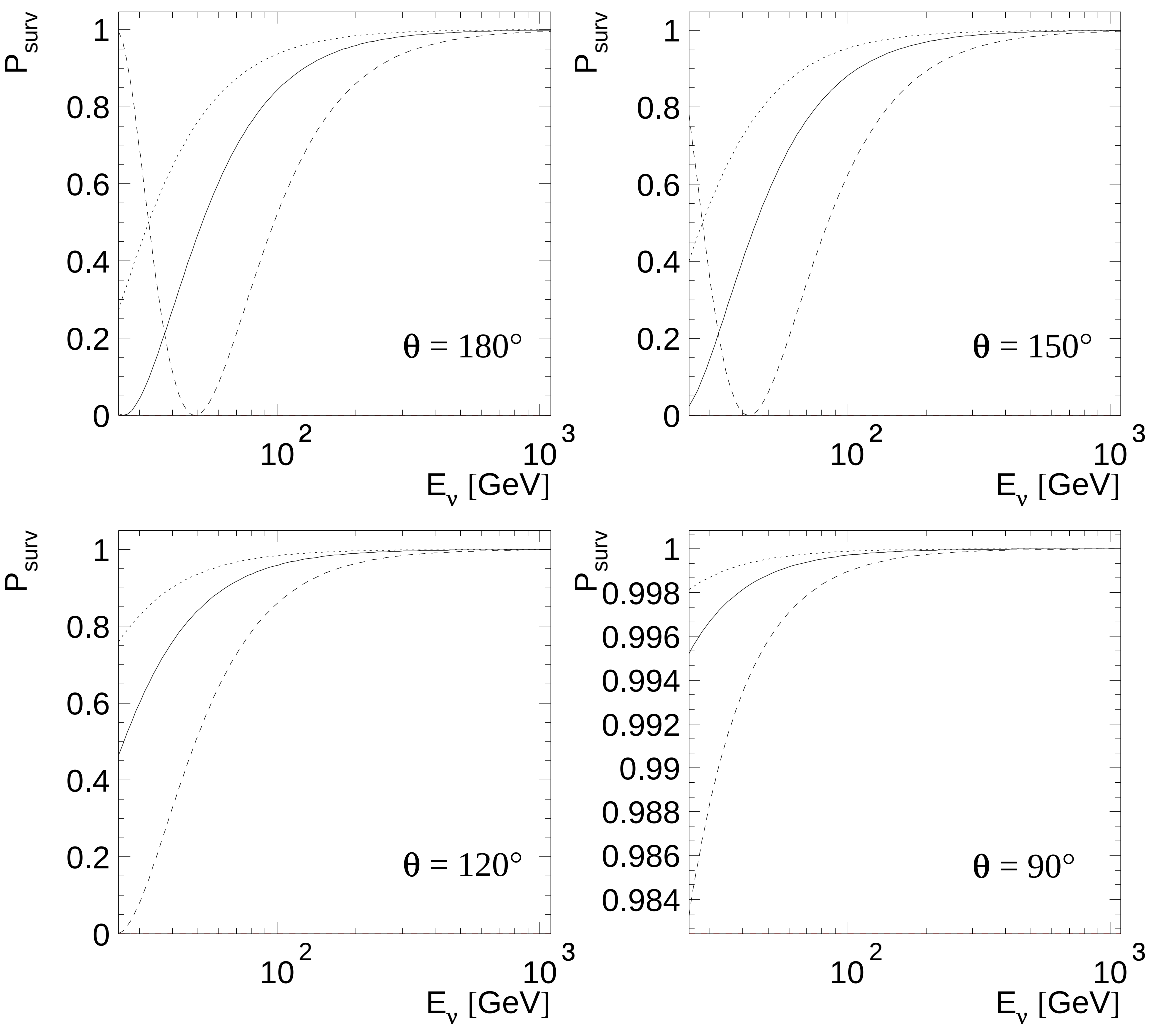

Figure 6.6: Atmospheric muon-neutrino survival probabilities at the location of AMANDA. The arrival angle in each plot is given with respect to vertical, and three Δm^2 values were used: the SK favored $3.2 \cdot 10^{-3}$ eV^2 (solid), and $2.0 \cdot 10^{-3}$ eV^2 (dotted) and $6.0 \cdot 10^{-3}$ eV^2 (dashed) from the edges of the SK 99% confidence range [102].

Neutrino oscillation models

Evidence of neutrino-flavor oscillation has recently been put forward by several experimental groups, most notably by the Super-Kamiokande collaboration [103, 104]. The atmospheric-neutrino flux prediction for AMANDA data can be modified to account for muon neutrino disappearance. In the $\nu_\mu \to \nu_\tau$ mixing case, the neutrino survival probability is given by [105, 106]

$$P_{\mathrm{surv}} = 1 - P_{\nu_\mu \nu_\tau} = \sin^2 2\theta \sin^2 \left(1.27 \cdot \frac{\Delta m^2 \cdot L}{E}\right), \tag{6.1}$$

where θ is the mixing angle, L is the distance traveled expressed in km, E is the neutrino energy expressed in GeV, and Δm^2 is the squared mass difference between the two neutrino flavors given in eV^2. Complete mixing ($\sin^2 2\theta = 1$) and Δm^2 around the Super-Kamiokande 90% confidence range ($0.001 \lesssim \Delta m^2 \lesssim 0.008$ [102]) will be used to test AMANDA data against the neutrino oscillation hypothesis. The neutrino survival probabilities for several cases are shown in Figure 6.6. Flavor oscillation should be visible only for lower neutrino energies ($E \lesssim 200$ GeV), which is just in the region where the majority of atmospheric neutrino data are found (see Figure 6.4).

6.2.4 Comparison of atmospheric neutrino models with data

The spectrum of atmospheric-neutrino induced events can be predicted using various combinations of neutrino flux and oscillation models. Muon energy distributions for different models were compared against the data using a χ^2 test. The probability that two samples are drawn from the same primary distribution is given by [107],

$$P_{\chi^2}(\chi^2, \eta) = Q\left(\frac{\chi^2}{2}, \frac{\eta}{2}\right) \equiv \frac{\Gamma\left(\frac{\chi^2}{2}, \frac{\eta}{2}\right)}{\Gamma\left(\frac{\chi^2}{2}\right)}, \tag{6.2}$$

$$\chi^2 = \sum_i \frac{(D_i - S_i)^2}{\sigma_{D_i}^2 + \sigma_{S_i}^2}, \tag{6.3}$$

where Q is the incomplete gamma function, Γ is the gamma function, η is the number of degrees of freedom, and D_i, S_i, $\sigma_{D_i}^2$, and $\sigma_{S_i}^2$ refer to data and simulation bin values with their respective variances. To avoid uncertainties arising from the absolute normalization of neutrino flux, which in turn depends on the primary cosmic-ray flux normalization, the data and simulation distributions have been renormalized to the same area. Thus, only the agreement of the shapes of the distributions will be tested.

The data can be compared with various predictions at different quality levels. Figure 6.7 compares the two flux models and several oscillation scenarios at quality levels 5 through 16. The agreement progressively improves for higher quality levels up-to level 12 (with the exception of level 10 in most cases). From the bottom panel of Figure 6.3, it can be seen that levels 10 and 13 have low differential passing ratios, which would indicate that they affect data and simulation in different ways. It appears that level 11 corrects for level 10, while above level 12 data and predictions are in poor agreement. This could indicate that there is some difference between data and simulation event topology or types of events present. Quality level 12 shows the best agreement between data and all flux scenarios, and is expected to contain ~ 1 down-going, atmospheric-muon background event [85].

Figure 6.8 compares the various models at level 12. The best agreement exists for low, nonzero values of Δm^2, although the no-oscillation scenario cannot be ruled out. Also, there is very little difference between the two atmospheric neutrino flux models for $\Delta m^2 \leq 4.5 \cdot 10^{-3}$ eV^2.

P_{χ^2} is a smooth function of Δm^2 that can be described well by a 10^{th}-order polynomial. The fit parameters for both atmospheric flux models, F_{lip} and F_{agls}, are given in Table 6.1 and the quality of the fits is shown in Figure 6.9. The fits F_{lip} and F_{agls} peak at $2.45 \cdot 10^{-3}$ eV^2 and $2.71 \cdot 10^{-3}$ eV^2, respectively; the 99% probability ranges[§] are given by

---

[§] which should not be confused with model rejection confidence levels

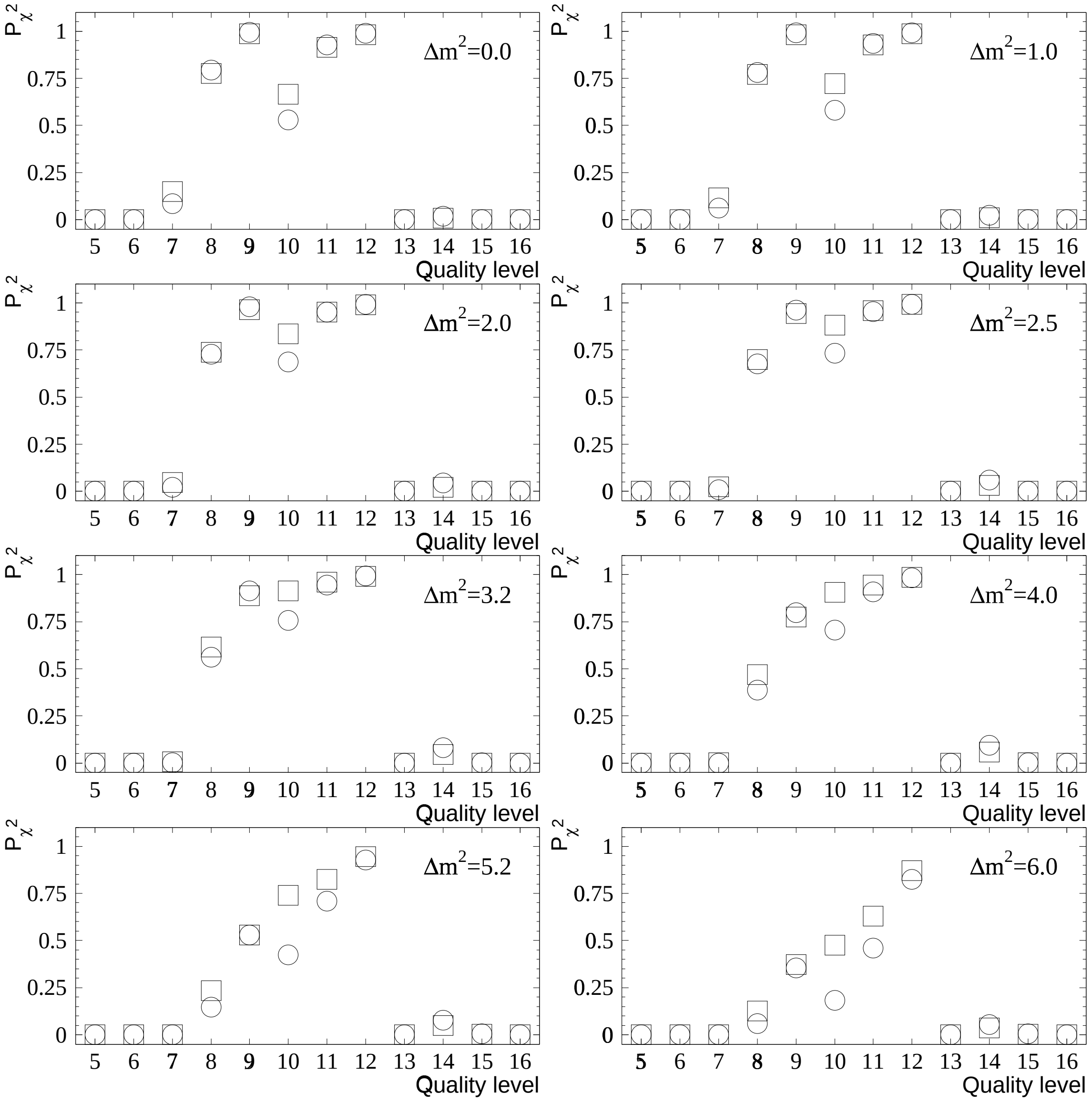

Figure 6.7: Comparison of data and various prediction distributions at different quality levels. Circles correspond to Φ_{lip} and squares to Φ_{agls}. Complete mixing is assumed and the neutrino-flavor mass difference is given in units of 10^{-3} eV^2; $\Delta m^2 = 0$ corresponds to the no-oscillation case.

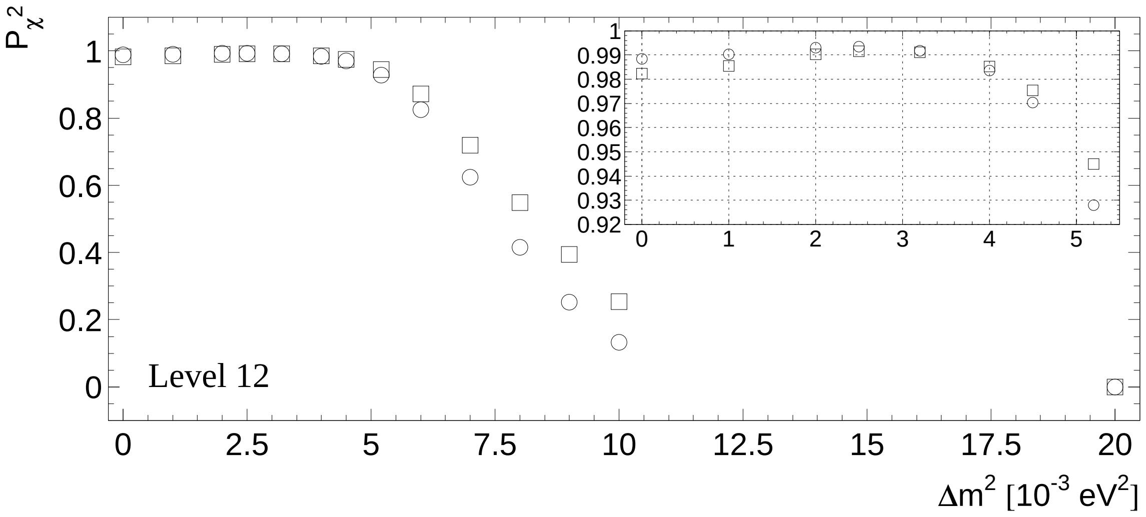

Figure 6.8: Comparison of data and various prediction distributions at level 12. The circles correspond to Φ_{lip} and squares to Φ_{agls}. The inset is an enlargement of the low mass difference range.

Table 6.1: The 10th-order polynomial coefficients for the P_{χ^2} *vs* Δm^2 fits. Values of Δm^2 in units of 10^{-3} eV^2 should be used with the coefficients given here.

	F_{lip}		F_{agls}	
a_0	0.9883999228477		0.9823013544083	
a_1	0.1414006203413	$\times 10^{-1}$	-0.2858249936253	$\times 10^{-2}$
a_2	-0.2938158810139	$\times 10^{-1}$	0.1666767336428	$\times 10^{-1}$
a_3	0.2367551438510	$\times 10^{-1}$	-0.2181405201554	$\times 10^{-1}$
a_4	-0.5817274563015	$\times 10^{-2}$	0.1785285957158	$\times 10^{-1}$
a_5	-0.1868171035312	$\times 10^{-2}$	-0.8931267075241	$\times 10^{-2}$
a_6	0.1482067513280	$\times 10^{-2}$	0.2700663404539	$\times 10^{-2}$
a_7	-0.3779469698202	$\times 10^{-3}$	-0.4922021762468	$\times 10^{-3}$
a_8	0.4766150232172	$\times 10^{-4}$	0.5227423025644	$\times 10^{-4}$
a_9	-0.2991620476678	$\times 10^{-5}$	-0.2964358827739	$\times 10^{-5}$
a_{10}	0.7461270712383	$\times 10^{-7}$	0.6923390571956	$\times 10^{-7}$

$[0.16, 3.46] \cdot 10^{-3}$ eV^2 and $[1.91, 3.45] \cdot 10^{-3}$ eV^2, respectively.

Fits to P_{χ^2} of the two flux models, constrained to favor the no-oscillation scenario, have worse χ^2 than the unconstrained polynomial fits. The F-tests [107] of P_{χ^2} deviations from the fits show that they are not consistent between constrained and unconstrained fits,

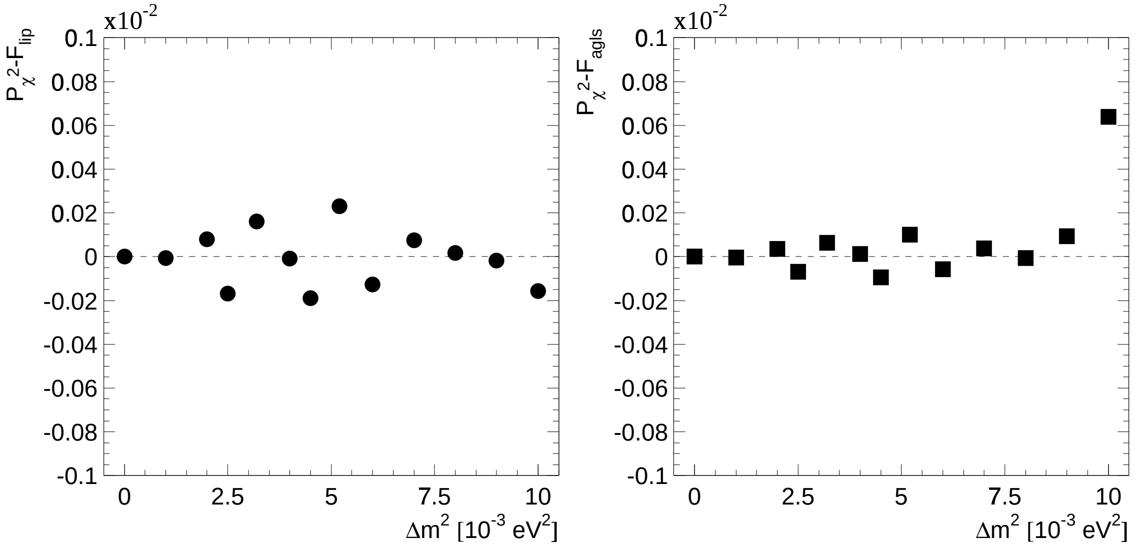

Figure 6.9: The difference between calculated P_{χ^2} and 10^{th}-order polynomial fit to P_{χ^2} for Φ_{lip} (left) and Φ_{agls} (right).

thus indicating that the peak structure in P_{χ^2} *vs* Δm^2 is not a statistical fluctuation.

Table 6.2 lists numbers of predicted events at level 12 for different scenarios. The number of observed events is 112. Since Φ_{lip} predicts fewer events than Φ_{agls}, and limiting the favored Δm^2 range to $P_{\chi^2} > 0.99$, it can be stated that the best agreement exists between data and the Φ_{lip} model with $1.6{\cdot}10^{-4}$ eV$^2 \leq \Delta m^2 \leq 3.46{\cdot}10^{-3}$ eV^2. However, with the present data statistics no oscillation or flux model can be excluded with a meaningful degree of confidence. Before an analysis like that is attempted, better understanding of the cause (or causes) of the difference in absolute normalization between data and simulation is needed. Most importantly, the systematic uncertainty in the absolute detection efficiency of AMANDA [99] has to be reduced.

Table 6.2: The expected number of events for various prediction scenarios at quality level 12. The observed number of events is 112.

Δm^2 $[10^{-3}\mathrm{eV}^2]$	N_{lip}	N_{agls}	$N_{\mathrm{lip}}/N_{\mathrm{agls}}$
0	158.4±2.7	171.2±3.0	0.925
1.0	157.2±2.7	170.0±2.7	0.925
2.0	153.8±2.6	166.2±2.8	0.925
2.5	151.5±2.5	163.6±2.7	0.926
3.2	147.8±2.4	159.5±2.6	0.927
4.0	143.2±2.3	154.4±2.5	0.927
4.5	140.2±2.2	151.0±2.4	0.928
5.2	136.0±2.1	146.4±2.3	0.929
6.0	131.4±2.1	141.3±2.2	0.930
7.0	126.2±2.0	135.6±2.1	0.931
8.0	121.8±1.9	130.9±2.1	0.930
9.0	118.4±1.8	127.1±2.0	0.932
10.0	115.0±1.8	124.1±2.0	0.932

6.3 Atmospheric muons

Due to the simple nature of the trigger logic, the vast majority of the data recorded by AMANDA consists of down-going atmospheric muons. Any contribution from an up-going neutrino signal can be safely ignored at that level. The same criteria applied for selection of up-going neutrino-induced events can be used for down-going muon selection by simple inversion of the directional requirement, i.e., events with the best fit to a down-going direction that is better than the best fit to an up-going direction are accepted. Similarly, the atmospheric-muon MC prediction and calibration data are put through the same set of inverted directional requirements.

Data used in this analysis come from run 516, recorded on April 11, 1997. The total live-time used is 7511.82 seconds, or 2.09 hours. Only events that triggered the main 16-fold trigger were selected, cleaned, and reconstructed, producing 657141 events in the sample.

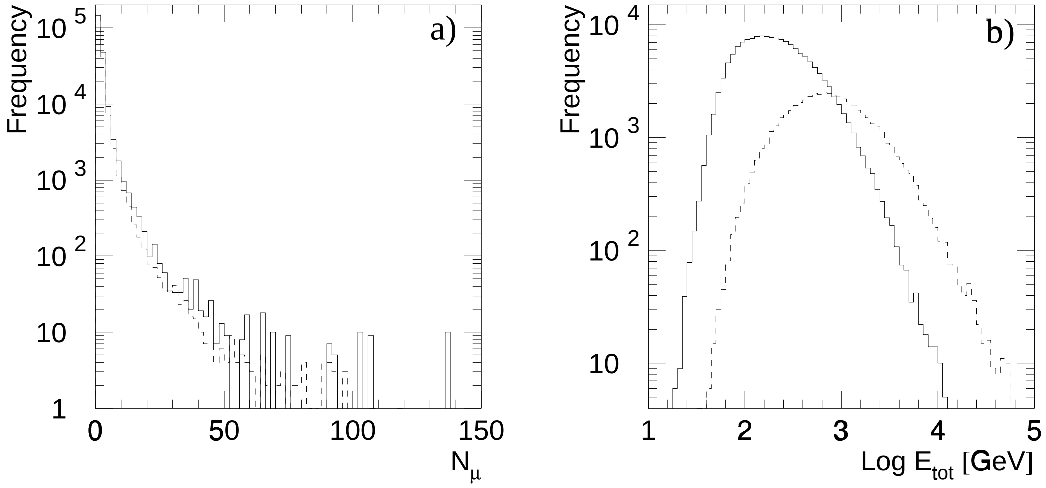

Figure 6.10: a) Number of muons generated in cosmic ray showers (solid) and number of muons reaching AMANDA (dashed). b) Energy distributions for single muons (solid) and muon bundles (dashed) predicted by atmospheric-muon simulation. The energy of all muons in a bundle has been summed up before generating the distribution.

The MC prediction data, corresponding to 2610.08 seconds of live-time, were generated with the use of CORSIKA [108] for air shower development and MMC [45] for muon propagation.

6.3.1 Muon bundles

Before comparing experimental with predicted data, the known problem of muon bundles – multiple muons in the same event (see example in Figure 6.11) – should be discussed. High-energy cosmic rays can generate air showers with high multiplicities of muons (Figure 6.10). Since a bundle is not tightly collimated¶, it produces a light signal with different spatial and temporal signatures from a single muon. At the moment, neither the muon trajectory reconstruction (see Ref. [82], Appendix B) nor the muon energy reconstruction is able to take this difference into account. Additionally, Bayesian unfolding using

---

¶The bundle radius can be up to tens of meters.

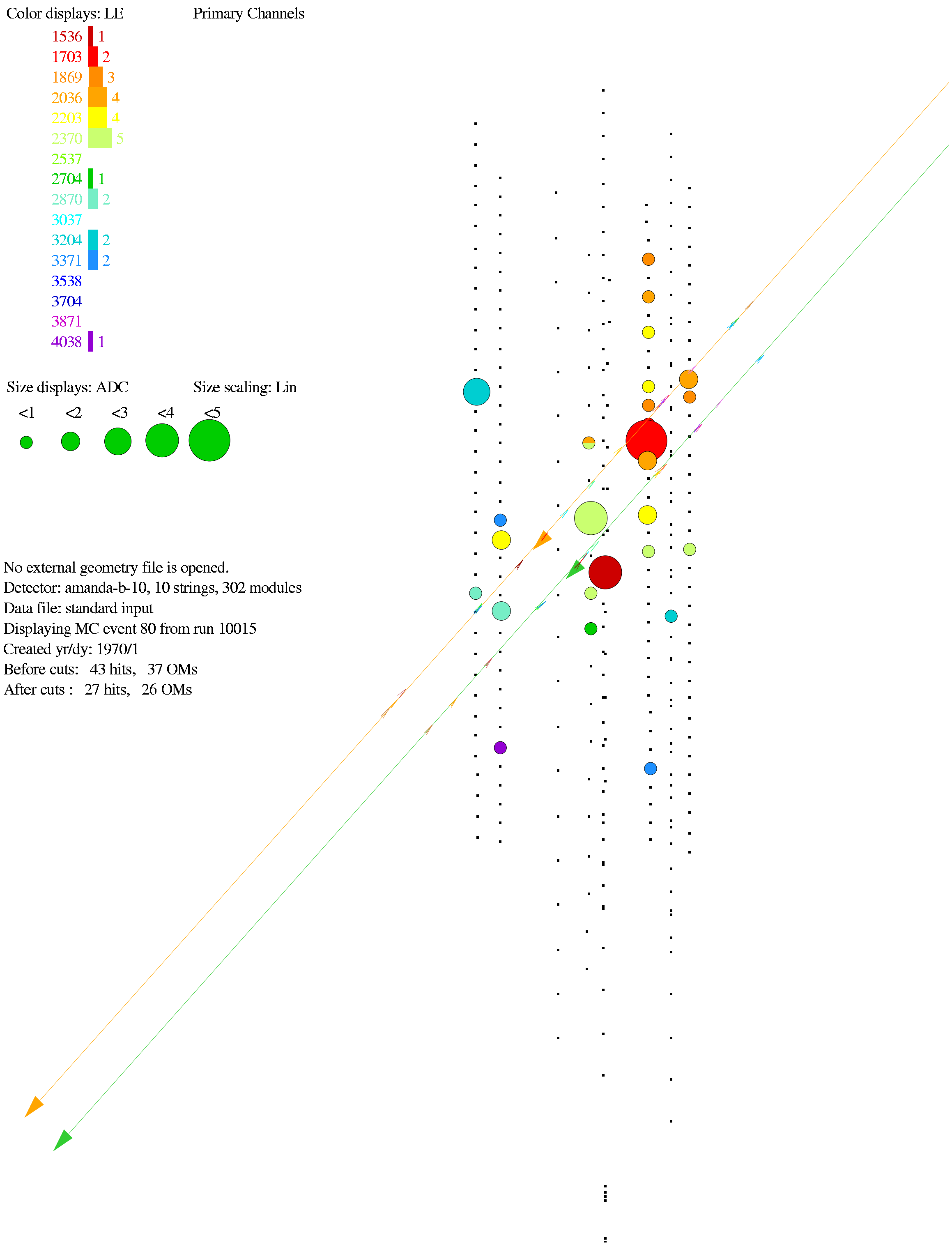

Figure 6.11: An example of a MC event generated by two coincident muons originating in the same cosmic-ray air shower.

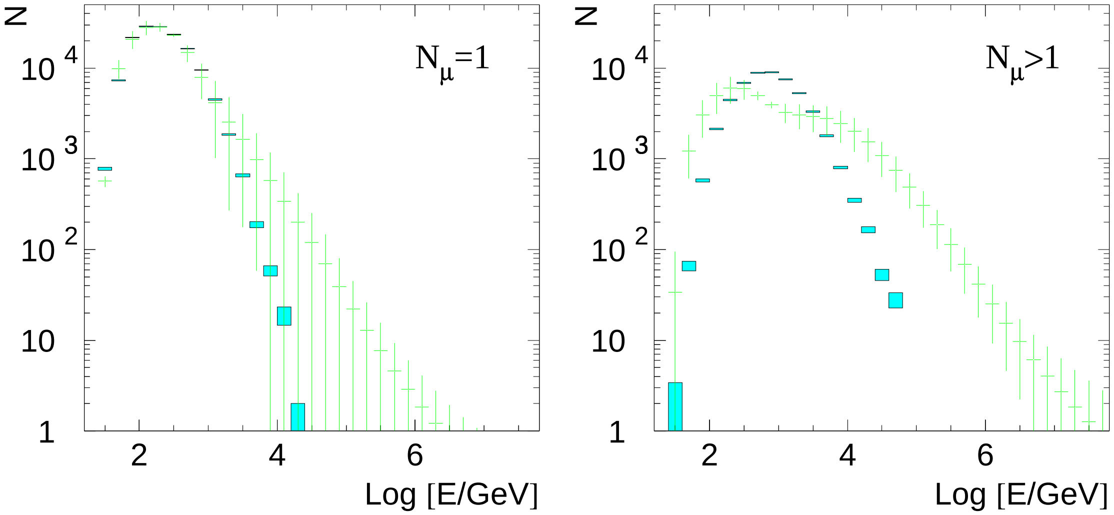

Figure 6.12: Left: Unfolded (green points) and true (cyan boxes) energy spectrum of single muon events. The large uncertainties result from low statistics for events with $E > 10$ TeV. Right: Unfolded (green points) and true (cyan boxes) energy spectrum of muon bundle events. The unfolding has been performed with the smearing matrix trained on a single-muon flux.

a smearing matrix that has been trained on the data set without muon bundles also cannot correct for the disagreement. Figure 6.12 compares unfolded energy spectra of single muon events and muon bundle events from MC data. The energy spectrum for the muon bundle data set is unfolded rather poorly, so any comparison of the experimental energy spectrum with the predicted one would be affected. To solve this problem, a smearing matrix trained on the data set with muon bundles will be used to unfold the experimental atmospheric muon sample.

6.3.2 Energy spectrum of atmospheric muons

The measured atmospheric muon spectrum shows poor agreement with the predicted atmospheric muon spectrum (Figure 6.13). χ^2 test indicates zero probability that

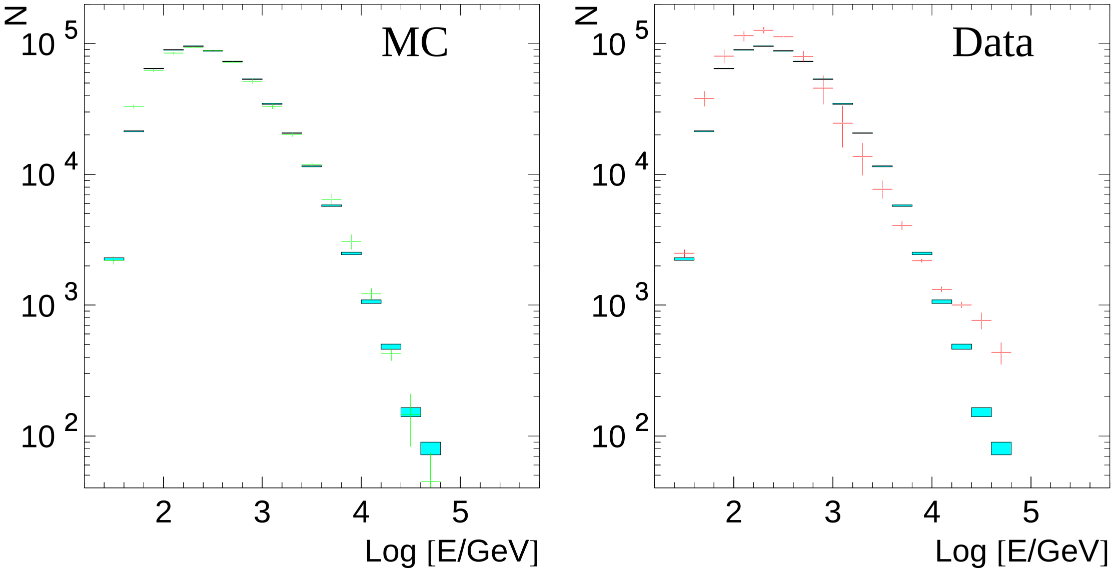

Figure 6.13: Left: Comparison of unfolded (green points) and true (cyan boxes) energy spectra for simulated atmospheric muon sample. Right: Comparison of measured (red points) and predicted (cyan boxes) atmospheric muon energy spectra. The unfolding has been performed with the smearing matrix trained on a muon flux including muon bundles.

the data and the prediction samples have been drawn from the same parent distribution. The simulation predicts only 85.8% of the observed muon event rate, but renormalizing the two distributions to the same area does not reduce the disagreement.

Another analysis of atmospheric muons detected by AMANDA [92] also reports disagreement between experimental data and prediction. Possible causes for this difference can range from cosmic ray flux to muon propagation to systematic uncertainties in AMANDA behavior (see Ref. [82], Appendices C and D).

Understanding the discrepancy between observed and predicted atmospheric-muon fluxes in AMANDA offers a rich research topic [109], touching upon various physics questions like composition and intensity of the very-high-energy ($E \gtrsim 1$ PeV) cosmic ray flux, high-energy ($E \gtrsim 1$ TeV) muon interaction cross-sections, charm production and decay in atmospheric showers, and many others. The energy reconstruction technique offers a new tool that can help to solve this puzzle.

6.4 Summary

In this chapter, two examples have been shown of how muon energy reconstruction can contribute to the analysis of AMANDA data. Other possible uses could be for improvement in neutrino candidate selection, extraction of samples of very-high-energy neutrinos, and improvement of directional reconstruction.

The measured energy spectrum of atmospheric neutrinos recorded in 1997 shows no excess of high-energy events that could be attributed to extraterrestrial neutrino sources, indicating only that the extraterrestrial flux is below the 1997 detector sensitivity. The neutrino energy spectrum shows support for $\nu_\mu \to \nu_\tau$ neutrino-flavor oscillation within the oscillation parameter region constrained by the Super-Kamiokande experiment. The SK measurements have been made on lower energy neutrinos ($E \lesssim 10$ GeV), and it is reassuring that evidence of the same oscillation trend is emerging at higher energies ($E > 25$ GeV). With the larger set including 1998 and 1999 data, it is likely that more conclusive results about oscillation parameters can be established with AMANDA-B10 data. AMANDA-II, which has a larger effective area and has been operating since 2000, is even better suited for neutrino oscillation measurements.

Previous studies of the possibility of observation of neutrino oscillation with AMANDA [110, 111] have shown that AMANDA-B10 would be inadequate to detect oscillations. This is due to the fact that it was assumed that neutrino oscillation would be observed (i) through angular dependence of neutrino flux or (ii) by energy measurements of contained muon events. In both cases, the statistics gathered by AMANDA-B10 would be insufficient to reveal evidence of oscillation.

The measured energy spectrum of atmospheric muons shows disagreement in the shape with the prediction, which adds to the set of previously discovered observables (i.e., event rate and zenith angle flux dependence) that indicates an incomplete understanding of either the detector behavior, or the physical processes behind the atmospheric muon flux, or both.

Chapter 7

Conclusions

"Kids, you tried your best, and you failed
miserably. The lesson is, never try."
Homer Simpson, *The Simpsons,*
"Burns' Heir", **1F16**

The AMANDA detector was built with the primary goal being the study of high-energy neutrino physics, astrophysics, and cosmology. A high energy-threshold (of ~50 GeV) and reasonable neutrino detection rate with good directional resolution of incoming neutrino-generated muons were primary design concerns [36]. The published analyses of the 1997 data set show that these design objectives have been met [42].

The muon energy reconstruction method presented in this work shows that with use of more detailed modeling of the physics processes occurring in the detector combined with some statistical methods one can extract additional information content from the AMANDA-B10 detector.

Applying the new energy reconstruction technique to the 1997 data set, the energy spectrum of atmospheric neutrino data recorded by AMANDA has been shown to be consistent with atmospheric-neutrino flux models [100, 101]. The atmospheric-neutrino spectrum has been checked for evidence of the neutrino-flavor oscillation hypothesis with assumption of full mixing ($\sin^2 2\theta = 1$) and within the neutrino-flavor mass difference range favored by the Super-Kamiokande collaboration [102]. The data shows best agreement with predictions using $1.6 \cdot 10^{-4}$ eV$^2 \leq \Delta m^2 \leq 3.46 \cdot 10^{-3}$ eV^2, which agrees with the SK results. At the moment, the conclusions that can be drawn about the atmospheric neutrino sample are primarily limited by the data statistics. By enlarging the experimental sample with data gathered since 1997, more stringent limits could be placed on neutrino flux and oscillation models.

The measurement of the atmospheric-muon energy spectrum shows disagreement in the shape and event rate with the predicted spectrum. Apart from the possibility that the difference is caused by instrumental effects, this indicates incomplete understanding of the physics that is used to describe the atmospheric muon flux at AMANDA depths. Other investigations of atmospheric muons detected by AMANDA have also pointed out the disagreement with the prediction. The understanding of the atmospheric muon flux is an inviting topic for future investigations, considering the wealth of experimental data available. For example, taking into account charm decay models mentioned in Section 1.2.2 could improve energy spectrum agreement at $E_\mu \gtrsim 10$ TeV.

The `photonics` software developed for use with the muon energy reconstruction has already been independently used to calculate OM active volumes as a function of OM depth for supernova search analysis performed by the AMANDA collaboration [112]. Presently, `photonics` is being implemented as the primary light table generator for the

AMANDA Monte Carlo simulation chain. This implementation will remove certain systematic effects which have been shown to exist for energy reconstruction of simulated data (see Section 5.2.1).

Previously, it has been shown that hit timing information can be used for energy reconstruction of electron-neutrino cascades recorded by AMANDA [113]. Since hit time is currently not being used in muon energy reconstruction, combining the two techniques could offer improvements in quality of the reconstruction. Other possible improvements to the technique presented here would be amplitude superposition with proper treatment of time delay between the pulses, more realistic PMT saturation modeling, and the correct treatment of hit cleaning during the maximum likelihood search.

At the time of this writing, the energy reconstruction method developed here still awaits complete integration into the AMANDA data simulation and processing chains. With minor technical modifications, the method described here can be extended for use in energy reconstruction of contained events, both electron- and muon-neutrino induced. Additionally, the muon vertex, cascade event, and concurrent energy-directional reconstructions could be developed on the same principles as the ones laid down for this energy reconstruction.

There is promise that once this integration and development are complete they will contribute greatly to future analyses of AMANDA data. This is particularly true for larger versions of the AMANDA detector: the currently operating AMANDA-II and the planned IceCube. Once this is achieved, high-energy neutrinos will have to start giving away the secrets they are so successfully guarding.

Bibliography

[1] W. C. Haxton and B. R. Holstein, Am. J. Phys. **68**, 15 (2000).

[2] DONUT Collaboration, Phys. Lett. B **504**, 218 (2001).

[3] V. F. Hess, Phys. Zeits. **13**, 1084 (1912).

[4] R. Davis, Phys. Rev. Lett. **12**, 303 (1964).

[5] A. Abramovici *et al.*, Science **256**, 325 (1992).

[6] R. Svensson and A. A. Zdziarski, Ap. J. **349**, 415 (1990).

[7] J. G. Learned and K. Mannheim, Ann. Rev. Nucl. Sci. **50**, 679 (2000).

[8] M. S. Longair, in *High Energy Astrophysics*, 2nd ed. (Cambridge U. Press, Cambridge, UK, 1997), Vol. 2, section 20.5, pp. 340–341.

[9] D. H. Perkins, in *Introduction to High Energy Physics*, 2nd ed. (Addison-Wesely, Reading, MA, 1982), chapter 7, pp. 272–273.

[10] K. Kleinknecht, in *Detectors for Particle Radiation*, 1st ed. (Cambridge U. Press, Cambridge, UK, 1986), section 8.6.2, pp. 191–192.

[11] K. Greisen, Ann. Rev. Nucl. Sci. **10**, 63 (1960).

[12] I. A. Belolaptikov *et al.*, Astrop. Phys. **7**, 263 (1997).

[13] A. Capone, in *Proceedings of the 27th International Cosmic Ray Conference*, edited by K.-H. Kampert, G. Hainzelmann, and C. Spiering (Copernicus Gesellschaft, Hamburg, Germany, 2001), pp. 1233–1235.

[14] S. Bottai, in *Proceedings of the 26th International Cosmic Ray Conference*, edited by D. Kieda, M. Salamon, and B. Dingus (IUPAP, Salt Lake City, Utah, 1999), No. 2, pp. 456–459.

[15] M. A. Markov and I. M. Zheleznykh, Nucl. Phys. **27**, 385 (1961).

[16] T. K. Gaisser, in *Cosmic rays and particle physics*, 1st ed. (Cambridge U. Press, Cambridge, UK, 1990), section 8.1, p. 106 ff.

[17] J. V. Jelley, *Čerenkov Radition; and its applications* (Pergamon, New York, 1958).

[18] I. A. Belolaptikov *et al.*, in *Proceedings of the 24th International Cosmic Ray Conference* (IUPAP, Rome, Italy, 1995), No. 1, pp. 742–745.

[19] P. C. Mock *et al.*, in *Proceedings of the 24th International Cosmic Ray Conference* (IUPAP, Rome, Italy, 1995), No. 1, pp. 758–761.

[20] A. Roberts, Rev. Mod. Phys. **64**, 259 (1992).

[21] Y. Fukuda *et al.*, Phys. Rev. Lett. **82**, 2644 (1999).

[22] A. Karle, in *Proceedings of the 26th International Cosmic Ray Conference*, edited by D. Kieda, M. Salamon, and B. Dingus (IUPAP, Salt Lake City, Utah, 1999), No. 2, pp. 221–224.

[23] J. H. Kim, in *Proceedings of the 26th International Cosmic Ray Conference*, edited by D. Kieda, M. Salamon, and B. Dingus (IUPAP, Salt Lake City, Utah, 1999), No. 2, pp. 196–199.

[24] M. Thunman, G. Ingelman, and P. Gondolo, Astrop. Phys. **5**, 309 (1996).

[25] E. V. Bugaev *et al.*, Phys. Rev. D **58**, 054001 (1998).

[26] T. S. Sinegovskaya and S. I. Sinegovsky, Phys. Rev. D **63**, 096004 (2001).

[27] A. Misaki, T. S. Sinegovskaya, S. I. Sinegovsky, and N. Takahashi, in *Proceedings of the 27th International Cosmic Ray Conference*, edited by K.-H. Kampert, G. Hainzelmann, and C. Spiering (Copernicus Gesellschaft, Hamburg, Germany, 2001), pp. 1025–1028.

[28] T. K. Gaisser, F. Halzen, and T. Stanev, Phys. Rept. **258**, 173 (1995), *Erratum*-ibid. **271**, 355 (1996).

[29] D. Lowder *et al.*, Nature **353**, 331 (1991).

[30] G. Musser, Scientific American Presents **10**, (Winter 1999), *Seven Wonders of Modern Astronomy*, http://www.sciam.com/specialissues/1299engineering/1299musser.html.

[31] A. Capone, in *Proceedings of the 26th International Cosmic Ray Conference*, edited

by D. Kieda, M. Salamon, and B. Dingus (IUPAP, Salt Lake City, Utah, 1999), No. 2, pp. 444–447.

[32] Y. D. He and P. B. Price, J. Geophys. Res. **103**, 17041 (1998).

[33] K. Woschnagg and P. B. Price, Appl. Opt. **40**, 2496 (2001).

[34] F. Halzen and J. G. Learned, in *Proceedings of the 5th International Symposium on Very High Energy Cosmic Ray Interactions* (Lodz, Poland, 1988).

[35] D. M. Lowder *et al.*, in *Proceedings of the 23th International Cosmic Ray Conference* (IUPAP, Calgary, Canada, 1993), No. 4, pp. 569–572.

[36] A. Biron *et al.*, *Proposal: Upgrade of AMANDA-B towards AMANDA-II*, submitted to the Physics Research Committee, DESY, PRC 97/05 (June 1997).

[37] G. C. Hill, in *Proceedings of the 26th International Cosmic Ray Conference*, edited by D. Kieda, M. Salamon, and B. Dingus (IUPAP, Salt Lake City, Utah, 1999), No. 2, pp. 432–435.

[38] R. W. Engstrom, *Photomultiplier Handbook*, Burle Technologies, Inc., 1980, TP-136.

[39] M. Kowalski, Diploma thesis, Humboldt U., Berlin, 1999.

[40] Amundsen-Scott South Pole Station, http://www.spole.gov.

[41] C. H. Wiebusch, in *Proceedings of the 25th International Cosmic Ray Conference*, edited by M. S. Potgieter, B. C. Raubenheimer, and D. J. van der Walt (IUPAP, Durban, South Africa, 1997), No. 7, pp. 13–16.

[42] E. Andrés *et al.*, Nature **410**, 441 (2001).

[43] C. Wiebusch, in *Simulation and Analysis Methods for Large Neutrino Telescopes*, edited by C. Spiering (DESY, Zeuthen, Germany, 1998), pp. 302–316, DESY-PROC-1999-01.

[44] O. Streicher, Ph.D. thesis, Humboldt U., Berlin, 2000.

[45] W. Rhode and D. Chirkin, in *Proceedings of the 27th International Cosmic Ray Conference*, edited by K.-H. Kampert, G. Hainzelmann, and C. Spiering (Copernicus Gesellschaft, Hamburg, Germany, 2001), pp. 1017–1020.

[46] D. Chirkin,

http://lisa.physics.berkeley.edu/~dima/work/MUONPR/muonPropagation.html.

[47] R. P. Kokoulin and A. A. Petrukhin, in *Proceedings of the 12th International Cosmic Ray Conference*, edited by A. G. Fenton and K. B. Fenton (U. of Tasmania Press, Hobart, Australia, 1971), No. 6, pp. A2436–2444.

[48] S. R. Kelner, Phys. At. Nucl. **61**, 448 (1998).

[49] `GEANT4` *Physics Reference Manual*, (2000), http://wwwinfo.cern.ch/asd/geant4/support.

[50] S. R. Kelner, R. P. Kokoulin, and A. A. Petrukhin, Phys. At. Nucl. **62**, 1894 (1999).

[51] L. B. Bezrukov and E. V. Bugaev, Sov. J. Nucl. Phys. **32**, 847 (1980).

[52] L. B. Bezrukov and E. V. Bugaev, Sov. J. Nucl. Phys. **33**, 635 (1981).

[53] W. Rhode and C. Cârloganu, in *Simulation and Analysis Methods for Large Neutrino Telescopes*, edited by C. Spiering (DESY, Zeuthen, Germany, 1998), pp. 247–261, DESY-PROC-1999-01.

[54] J. Breitweg *et al.*, Europ. Phys. J. **C7**, 609 (1999).

[55] Yu. M. Andreev, L. B. Bezrukov, and E. V. Bugaev, Phys. At. Nucl. **57**, 2066 (1994).

[56] S. R. Kelner, R. P. Kokoulin, and A. A. Petrukhin, Phys. At. Nucl. **60**, 576 (1997).

[57] I. A. Sokalski, E. V. Bugaev, and S. I. Klimushin, hep-ph/0010322 (2000).

[58] J. D. Jackson, in *Classical Electrodynamics*, 3rd ed. (Wiley, New York, 1998), chapter 13, p. 624 ff.

[59] R. M. Sternheimer, M. J. Berger, and S. M. Seltzer, Atomic Data and Nuclear Data Tables **30**, 261 (1984).

[60] P. Miočinović (unpublished).

[61] C. H. Wiebusch, Ph.D. thesis, Physikalische Institute, RWTH Aachen, 1995.

[62] R. Porrata, in *Proceedings of the 25th International Cosmic Ray Conference*, edited by M. S. Potgieter, B. C. Raubenheimer, and D. J. van der Walt (IUPAP, Durban, South Africa, 1997), No. 7, pp. 9–12.

[63] P. Askebjer *et al.*, Science **267**, 1147 (1995).

[64] P. Askebjer *et al.*, Geophys. Res. Lett. **24**, 1355 (1997).

[65] K. Woschnagg, in *Proceedings of the 26^{th} International Cosmic Ray Conference*, edited by D. Kieda, M. Salamon, and B. Dingus (IUPAP, Salt Lake City, Utah, 1999), No. 2, pp. 200–203.

[66] The AMANDA Collaboration, in preparation (unpublished).

[67] The AMANDA Collaboration, Appl. Opt. **36**, 4168 (1997).

[68] P. B. Price and L. Bergström, Appl. Opt. **36**, 4181 (1997).

[69] F. Urbach, Phys. Rev. **92**, 1324 (1953).

[70] L. A. Kuzmichev, hep-ex/0005036 (2000).

[71] P. B. Price and K. Woschnagg, Astrop. Phys. **15**, 97 (2001).

[72] P. Miočinović, ftp://grimm.berkeley.edu/ftp/pub/amasoft/photonics.

[73] K. W. Woschnagg, private communication.

[74] PTD software package, http://alizarin.physics.wisc.edu/karle/ptd/.

[75] P. B. Price, Science **267**, 1802 (1995).

[76] T. Uchida *et al.*, Appl. Opt. **34**, 5746 (1995).

[77] A. Karle and K. Woschnagg, http://alizarin.physics.wisc.edu/karle/hole-ice/.

[78] P. Olbrechts and C. Wiebusch, *On the Angular Sensitivity of Optical Modules in Ice*, AIR–20010102 (Jan. 2001).

[79] C. H. Wiebusch, *Preliminary Results on the Angular Response of the AMANDA Optical Module*, AIR–19960301 (Mar. 1996).

[80] J. R. Reitz, F. J. Milford, and R. W. Christy, in *Foundations of Electromagnetic Theory*, 3rd ed. (Addison-Wesley, Reading, MA, 1979), section 18-2, p. 385 ff.

[81] I. R. Liubarsky, Ph.D. thesis, U. of Wisconsin, Madison, 1997.

[82] K. Rawlins, Ph.D. thesis, U. of Wisconsin, Madison, 2001.

[83] J. Öhrmalm, Diploma thesis, Institutionen för strålningsvetenskap, Uppsala U., 1997, preprint TSL/ISV-97-0174.

[84] AMASIM software package, http://www.ps.uci.edu/~hundert/amanda/amasim/amasim.html.

[85] T. R. DeYoung, Ph.D. thesis, U. of Wisconsin, Madison, 2001.

[86] C. Wiebusch, *Hit probability and Energy reconstruction in AMANDA*, talk given at AMANDA meeting, Berkeley, 15-19 October 1997.

[87] T. DeYoung, private communication.

[88] The IceCube NSF proposal, http://pheno.physics.wisc.edu/icecube.

[89] G. D'Agostini, NIM A **362**, 487 (1995).

[90] OPAL Collaboration, Z. Phys. C **59**, 1 (1993).

[91] ALEPH Collaboration, Phys. Lett. B **307**, 209 (1993).

[92] P. Desiati and W. Rhode, in *Proceedings of the 27th International Cosmic Ray Conference*, edited by K.-H. Kampert, G. Hainzelmann, and C. Spiering (Copernicus Gesellschaft, Hamburg, Germany, 2001), pp. 985–988.

[93] S. Hundertmark, Ph.D. thesis, Humboldt U., Berlin, 1999.

[94] N. J. T. Smith *et al.*, NIM A **276**, 622 (1989).

[95] J. E. Dickinson *et al.*, NIM A **440**, 95 (2000).

[96] G. Barbagli *et al.*, in *Towards a Major Atmospheric Cerenkov Detector II; Calgary, Canada*, edited by R. C. Lamb (Iowa State U., Ames, Iowa, 1993).

[97] A. Biron, M. Leuthold, C. H. Wiebusch, and R. P. Wischnewski, *Analysis of atmospheric neutrinos in 97 data*, AIR–20010501 (May 2001).

[98] T. K. Gaisser, *Uncertainty in flux of Atmospheric Neutrinos: Implications for Upward Muons in Amanda B10*, AIR–20001201 (Dec. 2000).

[99] J. Ahrens *et al.*, *Observation of Atmospheric Neutrinos of 0.05 to 5 TeV energy with the Antarctic Muon and Neutrino Detector Array*, submitted Dec. 2001.

[100] P. Lipari, Astrop. Phys. **1**, 195 (1993).

[101] V. Agrawal, T. K. Gaisser, P. Lipari, and T. Stanev, Phys. Rev. D **53**, 1314 (1996).

[102] S. Fukuda *et al.*, Phys. Rev. Lett. **85**, 3999 (2000).

[103] Y. Fukuda *et al.*, Phys. Rev. Lett. **81**, 1562 (1998).

[104] The MACRO Collaboration, Phys. Lett. B **517**, 59 (2001).

[105] L. Wolfenstein, Phys. Rev. D **17**, 2369 (1978).

[106] V. Berger, K. Whisnant, S. Pakvasa, and R. J. N. Phillips, Phys. Rev. D **22**, 2718 (1980).

[107] W. H. Press, B. P. Flannery, S. A. Teukolsky, and W. T. Vetterling, in *Numerical Recipes in C; The Art of Scientific Computing*, 1st ed. (Cambridge U. Press, Cambridge, UK, 1988), chapters 6 and 13, p. 166 ff. and 471 ff.

[108] D. Chirkin and W. Rhode, in *Proceedings of the 26th International Cosmic Ray Conference*, edited by D. Kieda, M. Salamon, and B. Dingus (IUPAP, Salt Lake City, Utah, 1999), No. 2, pp. 16–19.

[109] D. Chirkin, Ph.D. thesis, in preparation.

[110] O. Botner, J. Conrad, A. Hallgren, and C. Pérez de los Heros, *On The Possibility of Measuring Neutrino Oscillations With AMANDA-II Using Contained Events*, AIR–19990301 (Mar 1999).

[111] O. Botner, J. Conrad, A. Hallgren, and C. Pérez de los Heros, *On the Sensitivity of AMANDA II and B10 to oscillation parameters using zenith angle distribution*, AIR–20000402 (Apr 2000).

[112] J. Ahrens *et al.*, Astrop. Phys. **16**, 345 (2002).

[113] R. A. Porrata, Ph.D. thesis, U. of California, Irvine, 1997.

[114] P. Sudhoff, *Transmission measurements with Amanda Glass and Evaluation for IceCube*, AIR–20010701 (July 2001).

[115] SiEGMuND software package,
http://www-zeuthen.desy.de/nuastro/software/siegmund/siegmund.html.

[116] CVS repository module `ekit`, hpbai1.ifh.de:/home/elrond/baikal/src/CVS.

Appendix A

`Photonics` user manual

`Photonics` software package has been developed for tracking of photons in non-uniform media. It is intended for use with water- or ice-based Čerenkov neutrino detectors. It is written in C, with technical support provided in form of exhaustive comments embedded in the source code. PAW histograms are used for visual display of tables.

The tables generated by `photonics` are 6 dimensional: 3 spatial, 2 directional, and 1 temporal. For optimal storage and ability of direct access, the data tables are stored in binary format.

A.1 `Photonics` overview

The package consists of the core library, various executables for creation and manipulation of data, scripts for automation of mass production, and miscellaneous configuration files. A separate submodule provides a custom interface for `amasim` [84].

All physics and crucial computational issues are handled by the `libphotonics` library. The executables provided are just simple interfaces to the library;

`photomc`	Implementation of a photon tracking MC
`photoid`	Displays a photon table header for easy identification
`photoadd`	Adds two tables with the same headers
`photoint`	Integrates a table over specified dimension
`photonorm`	Applies various normalization and weights to a table
`photobook`	Generates PAW histograms of subtables
`photoreader`	Quick table query tool
`photo2amasim`	Generates tables for use with `amasim`

A.2 Input parameters

All parameters describing a table and controlling execution are given to `photomc` at the start time. This can be done either interactively or with a driver file. The following options are available:

`Verbosity`	Diagnostic and progress output during MC run: 0 off, 1 on
`Long run`	To prevent loss of data during a long run due to computer crash or similar malfunction, the current table state can be saved to disk after each 1% of the total run time: 0 off, 1 on
`Statistical errors`	Track and record statistical errors for future analyses: 0 off, 1 on

`Step size/Run mode`	Selection of photon tracking mode used = 0, surface crossing method (fastest) < 0, volume density method with given value representing the step size (most accurate) > 0, hybrid method
`Runtime efficiency`	Which photon weights to be calculated during MC run. The following values are additive: 0 – Each photon weighted only by absorption 1 – Add directional acceptance weight of an OM 2 – Add weight as if OM were emitting light (EXPERTS ONLY! Can't be combined with 1) 4 – Add wavelength weight for OM, including dynode efficiency
`Source type`	1 – Isotropic emitter 2 – Čerenkov cone emitter 3 – Beamed emitter 4 – Cosine theta weighed emitter 5 – Electromagnetic shower 6 – Hadronic shower
`Extended source`	For showers, the source can be simulated as point-like or extended: 0 point-like, 1 extended
`Shower energy`	Applied if extended source is used, given in GeV

`Source radius`	If > 0, each photon emission point is randomly scattered within sphere of given radius (in meters) centered at the default source location. All other source parameters are unaffected.
`Axis angle`	Inclination of source z-axis with respect to vertical, given in degrees, rotated CCW about y-axis
`Radial offset`	Radial source location offset with respect to origin of tracking volume
`Vertical offset`	Vertical source location offset with respect to tracking volume origin
`Geometry type`	Spatial geometry type used 1 Spherical – Shells (r), slices (phi), and cones (theta) 2 Cylindrical – Cylinders (rho), slices (phi), and levels (z) 3 Cubic – (x), (y), and (z) planes
`Dimension definitions`	These define tracking[*] and active[†] volumes. Each dimension is defined by 5 numbers: • Number of bins in a dimension • Lower limit of active volume • Upper limit of active volume • Lower limit of tracking volume

---

[*] Volume within which photons are tracked

[†] Volume within which photon densities are recorded; thus the active volume must be a subset of the tracking volume

- Upper limit of tracking volume

Dimensions used are the following:

1. Radial (either shells or cylinders) or x levels [meters]
2. Azimuthal slices or y levels[‡] [degrees or meters]
3. Zenith cones or z levels [degrees or meters]
4. Emission zenith angle of a photon [degrees]
5. Detection zenith angle of a photon [degrees]
6. Delay time [nanoseconds]

`Tracking volume offset` Vertical offset of the tracking volume origin with respect to the global origin specified by a description of medium (see section A.3)

`Distance scaling`[§] 1 – linear binning; all metric bins have equal size scaling

2 – quadratic binning; all metric bins have quadratic size scaling around the origin

`Time scaling` 1 – linear binning; time bin sizes are equal

2 – quadratic binning; time bin sizes scale as square of the delay time

---

[‡] **NB:** y levels must always be ≥ 0 since symmetry around x-z plane is utilized to double the statistics. No checks on input are made, though!

[§] **NB:** All zenith dimensions are binned linear in cosine. All azimuthal dimensions are binned linear in degrees. Always.

`Photon wavelength`	> 0, monochromatic light of given wavelength (in nanometers) is used. Only 300–600 nm range is supported. -1, Čerenkov spectrum in 300–600 nm range is simulated
`Number of photons`	Number of photons to simulate
`Medium file`	Specifies file from which to read a description of medium (see A.3)
`Efficiency file`	Specifies file from which to take various efficiency options (see A.4)
`Output file`	Output file name

A.3 Medium description

The scattering, absorption, and other light propagation properties of a medium used for photon tracking are described in a *medium file.* The file format rules are the following:

- Comment lines must start with `#`. Blank lines are ignored.
- File header consists of:

  ```
  NLAYER <number of layers specified in the file>
  NWVL <wavelength bins> <lowest wavelength> <wavelength step>
  ```

- After the header comes the list of layers. Each layer starts with

  ```
  LAYER <lower edge> <upper edge>
  ```

  where upper and lower edges (in meters) are with respect to some arbitrary global origin

- Within a layer section, accepted commands are:

  `ABS <list of absorption coefficients per wavelength bin>`

  `SCAT <list of effective scattering coefficients per wavelength bin>`

  `COS <list of mean cosine of scattering angle per wavelength bin>`

  `N_GROUP <list of group indices of refraction per wavelength bin>`

  `N_PHASE <list of phase indices of refraction per wavelength bin>`

  Each list has to have the correct number of entries. Absorption and scattering coefficients are given in m^{-1}.

- Layer description is considered complete when a new `LAYER` line is encountered.

- Layers don't have to come or be described in any specific order.

A.4 Efficiency definitions

Various wavelength-dependent efficiencies are included in the `libphotonics` library. An efficiency file is used to select which tables should be used to weight the data. The efficiency file has the following format:

- Comment lines must start with `#`. Blank lines are ignored.

- Any number of selection lines can follow

  `<TAG> <VALUE>`

If some value is not specified in the efficiency file, the default selection is used. The following tag/value options are available (default values are bold):

`GLASS_N`	**1 – Borosilicate glass index of refraction, measured by P. Sudhoff** [114] 2 – Borosilicate glass index of refraction, from Benthos spec sheet 3 – Borosilicate glass index of refraction, from Igor's thesis [81]
`GEL_N`	1 – RTV6156 GE Silicones gel, from company spec sheet 2 – "Standard gel" from `dada_attn.f` [115] 3 – Gel index of refraction, from Igor's thesis **4 – RTV6156 GE Silicones gel, measured by P. Sudhoff, July 2001**
`QE`	**1 – Hamamatsu 8" PMT used in Amanda (R5912), curve 400K from Hamamatsu catalog OCT/98** 2 – Hamamatsu PMT, taken from `dada_attn.f`[¶] 3 – EMI PMT used by Amanda, taken from `data_attn.f`
`GLASS`	1 – Benthos housing, measured by A. Goobar (`dada_attn.f`) **2 – Benthos housing, measured by P. Sudhoff** 3 – Billings housing, measured by A. Goobar (`dada_attn.f`) 4 – Billings housing, measured by P. Sudhoff 5 – Nautilus housing, measured by P. Sudhoff 6 – Rasotherm housing, measured by P. Sudhoff
`GEL`	1 – "Standard gel" from `data_attn.f`

[¶] allegedly from a Hamamatsu catalog

	2 – Conjecture from Igor's thesis **3 – 10mm thick RTV6156 GE Silicones gel, measured by P. Sudhoff, July 2001**
`SENS`	Optional "–" selects for up-looking OM [–]**1 – OM angular sensitivity measurement by C. Wiebusch, Poisson method** [79] [–]2 – Uniform isotropic acceptance [–]3 – PTD parametrization of Ref. [79], taken from `scatter.c` [74]
`HOLE`	**0 – No bubbles, (h0 in PTD)** 1 – 100 cm bubble model (h1 in PTD) 2 – 50 cm bubble model (h2 in PTD) 3 – 30 cm bubble model (h3 in PTD) 4 – 10 cm bubble model (h4 in PTD) 5 – Model 5 from Ref. [78] (h5 in PTD) 6 – Model 6 from Ref. [78] (h6 in PTD)
`OM_CORR`	0 – No correction for OM curvature **1 – Standard correction for 13" Benthos-like housing** 2 – Standard correction for 12" Billings-like housing
`DYNODE`	Efficiency of 1st PMT dynode expressed as a fraction (**0.7884**)
`PMT`	PMT effective collection area in m^2 (**0.0284**)

Appendix B

Optical properties tables

Various physical values that are used by `photonics` are given here for the reference. All numbers are tabulated according to the efficiency file enumeration (see A.4). Angles between the ones given in the tables are linearly interpolated, and wavelengths are rounded to the nearest values.

Indices of refraction

Glass and gel indices of refraction (Table B.1) which are used to determine OM Fresnel transmittance probability.

Transparencies

Optical transparencies of glass (Table B.2) and gel (Table B.3) which are used to calculate probability for a photon not to be absorbed by various OM components.

Efficiencies

The quantum efficiency (Table B.4) and the OM angular acceptance (Table B.5) which both add to probability of photon detection. The quantum efficiencies provided here incorporate PMT glass absorption and Fresnel reflection in air.

Other tables

Two additional table sets used by `photonics` are hole ice corrections (Table B.6, see section 3.2.3) and OM curvature corrections (Table B.7, see section 4.1). The OM curvature correction tables are calculated for the two most common types of AMANDA OMs, 8" Hamamatsu PMT in either Benthos or Billings housing, using default values for relevant parameters.

Table B.1: Glass and gel indices of refraction.

Wvl [nm]	GLASS_N 1	GLASS_N 2	GLASS_N 3	GEL_N 1	GEL_N 2	GEL_N 3	GEL_N 4
305	1.744730	1.5	1.48	1.43	1.41	1.35	2.315840
315	1.589290	1.499	1.48	1.43	1.41	1.349	2.092180
325	1.534790	1.498	1.48	1.43	1.41	1.348	1.942220
335	1.515530	1.497	1.48	1.43	1.41	1.347	1.839150
345	1.507370	1.496	1.48	1.43	1.41	1.346	1.773940
355	1.501260	1.495	1.48	1.43	1.41	1.345	1.715500
365	1.495390	1.494	1.48	1.43	1.41	1.344	1.673260
375	1.490530	1.492	1.48	1.43	1.41	1.343	1.631180
385	1.494500	1.491	1.48	1.43	1.41	1.342	1.605290
395	1.494430	1.490	1.48	1.43	1.41	1.341	1.581310
405	1.491160	1.489	1.48	1.43	1.41	1.34	1.563480
415	1.488970	1.488	1.48	1.43	1.41	1.339	1.554280
425	1.487790	1.487	1.48	1.43	1.41	1.338	1.536860
435	1.486530	1.486	1.48	1.43	1.41	1.337	1.529060
445	1.486670	1.485	1.48	1.43	1.41	1.336	1.516110
455	1.485050	1.483	1.48	1.43	1.41	1.335	1.4974
465	1.482180	1.482	1.48	1.43	1.41	1.334	1.4857
475	1.480570	1.481	1.48	1.43	1.41	1.333	1.47558
485	1.480430	1.48	1.48	1.43	1.41	1.332	1.4672
495	1.483210	1.479	1.48	1.43	1.41	1.331	1.46057
505	1.479630	1.478	1.48	1.43	1.41	1.33	1.45556
515	1.477190	1.477	1.48	1.43	1.41	1.329	1.45193
525	1.475460	1.477	1.48	1.43	1.41	1.329	1.447250
535	1.476180	1.476	1.48	1.43	1.41	1.328	1.446450
545	1.474010	1.476	1.48	1.43	1.41	1.328	1.440800
555	1.472820	1.476	1.48	1.43	1.41	1.328	1.441180
565	1.474570	1.475	1.48	1.43	1.41	1.327	1.442670
575	1.472140	1.475	1.48	1.43	1.41	1.327	1.443800
585	1.472030	1.474	1.48	1.43	1.41	1.326	1.437320
595	1.471890	1.474	1.48	1.43	1.41	1.326	1.435090

Table B.2: Glass pressure housing probability of transmittance.

Wvl [nm]	GLASS 1	GLASS 2	GLASS 3	GLASS 4	GLASS 5	GLASS 6
305	0.	0.0112939	0.	0.0003765	0.0342255	0.0012610
315	0.	0.1042010	0.	0.0001739	0.1851400	0.0271668
325	0.153348	0.3319370	0.	0.0016904	0.4413050	0.1582090
335	0.41405	0.5832130	0.	0.0210386	0.6697710	0.3838220
345	0.576222	0.7635180	0.0947125	0.1056670	0.8163550	0.5920350
355	0.683824	0.8659730	0.262248	0.2779620	0.8952840	0.7288610
365	0.650244	0.9169690	0.483826	0.4834210	0.9339230	0.8025130
375	0.573643	0.9214480	0.611086	0.6421160	0.9370570	0.8104860
385	0.780108	0.9322730	0.694288	0.7547160	0.9446980	0.8303880
395	0.812597	0.9578120	0.756068	0.8459960	0.9612080	0.8688140
405	0.801069	0.9622680	0.797543	0.8937440	0.9619900	0.8749860
415	0.789786	0.9608580	0.80234	0.9149210	0.9591310	0.8727310
425	0.832803	0.9618210	0.812758	0.9281600	0.9582410	0.8755290
435	0.832527	0.9621350	0.828591	0.9355160	0.9571420	0.8782140
445	0.821745	0.9619110	0.833924	0.9395100	0.9570990	0.8821840
455	0.810587	0.9665100	0.848566	0.9476200	0.9606110	0.8927640
465	0.831576	0.9694110	0.85853	0.9549200	0.9635580	0.9012070
475	0.842021	0.9714570	0.88087	0.9592130	0.9667430	0.9071020
485	0.84199	0.9723970	0.860232	0.9614440	0.9687220	0.9120690
495	0.842603	0.9734950	0.857705	0.9640450	0.9709390	0.9174400
505	0.841814	0.9749000	0.866979	0.9658600	0.9730180	0.9224070
515	0.873634	0.9756480	0.89591	0.9676350	0.9747830	0.9270510
525	0.884021	0.9763080	0.891344	0.9688180	0.9758580	0.9301170
535	0.89497	0.9773750	0.891785	0.9697340	0.9776230	0.9327040
545	0.894464	0.9778710	0.882992	0.9691790	0.9783370	0.9336650
555	0.894188	0.9774870	0.88597	0.9676960	0.9782630	0.9348010
565	0.894595	0.9774810	0.886791	0.9658920	0.9779340	0.9363230
575	0.89403	0.9774590	0.879379	0.9636470	0.9774870	0.9357280
585	0.883233	0.9773840	0.877733	0.9624640	0.9769640	0.9352210
595	0.850889	0.9775440	0.87675	0.9617540	0.9764630	0.9350170

Table B.3: Optical gel probability of transmittance.

Wvl [nm]	GEL 1	GEL 2	GEL 3
305	1.0	0.95	0.735964
315	1.0	0.95	0.832648
325	1.0	0.95	0.881214
335	1.0	0.95	0.906408
345	1.0	0.95	0.922277
355	1.0	0.95	0.931897
365	1.0	0.95	0.940694
375	1.0	0.95	0.94709
385	1.0	0.95	0.953028
395	1.0	0.95	0.956769
405	1.0	0.95	0.960276
415	1.0	0.95	0.964450
425	1.0	0.95	0.96624
435	1.0	0.95	0.969458
445	1.0	0.95	0.971219
455	1.0	0.95	0.972116
465	1.0	0.95	0.973770
475	1.0	0.95	0.975316
485	1.0	0.95	0.976777
495	1.0	0.95	0.978169
505	1.0	0.95	0.979505
515	1.0	0.95	0.98079
525	1.0	0.95	0.981627
535	1.0	0.95	0.983156
545	1.0	0.95	0.983678
555	1.0	0.95	0.98521
565	1.0	0.95	0.986864
575	1.0	0.95	0.988455
585	1.0	0.95	0.988593
595	1.0	0.95	0.989049

Table B.4: PMT quantum photon-conversion efficiency.

Wvl [nm]	QE 1	QE 2	QE 3	Wvl [nm]	QE 1	QE 2	QE 3
265	0.0	0.001	0.001	485	0.1795	0.18	0.2
275	0.02	0.004	0.004	495	0.164	0.166	0.18
285	0.07	0.013	0.013	505	0.1465	0.157	0.16
295	0.1285	0.03	0.03	515	0.128	0.137	0.14
305	0.1725	0.117	0.010	525	0.1095	0.115	0.12
315	0.2035	0.16	0.22	535	0.09375	0.095	0.095
325	0.2345	0.2	0.265	545	0.08125	0.08	0.08
335	0.2565	0.22	0.29	555	0.06875	0.07	0.065
345	0.269	0.23	0.295	565	0.05625	0.065	0.05
355	0.2775	0.23	0.30	575	0.046	0.06	0.035
365	0.2825	0.23	0.3	585	0.0375	0.05	0.03
375	0.2865	0.24	0.3	595	0.029	0.04	0.02
385	0.2885	0.245	0.295	605	0.022	0.03	0.015
395	0.287	0.245	0.290	615	0.016	0.025	0.0
405	0.2825	0.245	0.285	625	0.0105	0.018	0.0
415	0.2775	0.24	0.275	635	0.00675	0.011	0.0
425	0.269	0.24	0.270	645	0.00475	0.006	0.0
435	0.2565	0.232	0.260	655	0.00325	0.003	0.0
445	0.242	0.23	0.25	665	0.002	0.002	0.0
455	0.226	0.227	0.24	675	0.0011	0.001	0.0
465	0.2105	0.22	0.225	685	0.0004	0.0	0.0
475	0.195	0.2	0.215				

Table B.5: OM angular acceptance normalized to forward direction.

Angle [°]	SENS 1	SENS 2	SENS 3
0	1.000000	1.0	0.994
5	0.994289	1.0	0.993133
10	0.988577	1.0	0.989637
15	0.978011	1.0	0.98154
20	0.967444	1.0	0.967439
25	0.949212	1.0	0.947866
30	0.930980	1.0	0.925321
35	0.905411	1.0	0.902793
40	0.879841	1.0	0.881634
45	0.858259	1.0	0.860185
50	0.844232	1.0	0.834179
55	0.800623	1.0	0.798882
60	0.749084	1.0	0.75185
65	0.688845	1.0	0.694712
70	0.634235	1.0	0.6329
75	0.581196	1.0	0.573369
80	0.521599	1.0	0.521482
85	0.488193	1.0	0.478682
90	0.425871	1.0	0.4421
95	0.413451	1.0	0.406233
100	0.365635	1.0	0.365713
105	0.318262	1.0	0.317787
110	0.267043	1.0	0.263379
115	0.209881	1.0	0.206472
120	0.146948	1.0	0.152332
125	0.108593	1.0	0.105568
130	0.070238	1.0	0.0688333
135	0.047919	1.0	0.0425399
140	0.025600	1.0	0.0253719
145	0.017173	1.0	0.0151544
150	0.008745	1.0	0.00963048
155	0.007309	1.0	0.00692966
160	0.005872	1.0	0.00572801
165	0.005350	1.0	0.00521401
170	0.004827	1.0	0.00497177
175	0.004468	1.0	0.00484354
180	0.004109	1.0	0.0048

Table B.6: OM angular acceptance correction due to presence of hole ice.

Angle [°]	HOLE 0	HOLE 1	HOLE 2	HOLE 3	HOLE 4	HOLE 5	HOLE 6
0	1.0	0.404343	0.193259	0.092813	0.005	0.1454	0.2025
5	1.0	0.420571	0.212933	0.111132	0.01	0.161657	0.211821
10	1.0	0.467357	0.269687	0.164288	0.0367462	0.207379	0.239752
15	1.0	0.539322	0.357108	0.247177	0.111869	0.274384	0.285721
20	1.0	0.628481	0.465741	0.352239	0.204963	0.351861	0.347505
25	1.0	0.725522	0.584671	0.470666	0.30745	0.429459	0.420209
30	1.0	0.821242	0.703286	0.593735	0.412298	0.499843	0.496167
35	1.0	0.907883	0.812863	0.713993	0.515517	0.559899	0.566229
40	1.0	0.98012	0.907668	0.826068	0.616786	0.610416	0.622243
45	1.0	1.03554	0.985393	0.926959	0.719019	0.65468	0.659936
50	1.0	1.07455	1.04685	1.0158	0.826938	0.696769	0.680974
55	1.0	1.09976	1.09505	1.09317	0.945011	0.740268	0.693201
60	1.0	1.11504	1.13393	1.16024	1.07532	0.787693	0.708596
65	1.0	1.12441	1.16697	1.2179	1.21597	0.840477	0.739417
70	1.0	1.13109	1.19623	1.26628	1.36072	0.899055	0.793784
75	1.0	1.13693	1.22188	1.3048	1.50014	0.962704	0.872337
80	1.0	1.14231	1.24253	1.33275	1.62437	1.02916	0.967391
85	1.0	1.14662	1.25631	1.35054	1.72722	1.09451	1.06522
90	1.0	1.1491	1.2625	1.3612	1.8109	1.154	1.151
95	1.0	1.15007	1.26336	1.37188	1.89038	1.20418	1.21497
100	1.0	1.15201	1.26572	1.39495	1.99639	1.24611	1.25771
105	1.0	1.16035	1.28192	1.44834	2.17603	1.2885	1.29275
110	1.0	1.18374	1.3297	1.55474	2.49035	1.34933	1.34521
115	1.0	1.23351	1.4309	1.73969	3.00873	1.45448	1.44679
120	1.0	1.32241	1.60893	2.02854	3.80036	1.63275	1.62811
125	1.0	1.46273	1.88533	2.4427	4.92376	1.90841	1.9107
130	1.0	1.66406	2.27585	2.99559	6.41579	2.2931	2.30092
135	1.0	1.93101	2.78673	3.68895	8.28178	2.78	2.7873
140	1.0	2.26139	3.41174	4.51026	10.4884	3.34258	3.34225
145	1.0	2.64514	4.13066	5.4315	12.9608	3.93888	3.92737
150	1.0	3.06426	4.90949	6.41006	15.5849	4.52021	4.50085
155	1.0	3.49397	5.7027	7.39141	18.2148	5.04182	5.02481
160	1.0	3.90489	6.45716	8.31373	20.6852	5.47182	5.47072
165	1.0	4.26605	7.11754	9.11376	22.8273	5.79553	5.82158
170	1.0	4.54841	7.63224	9.73329	24.4856	6.014	6.07076
175	1.0	4.72822	7.95937	10.1254	25.5349	6.13755	6.21849
180	1.0	4.78996	8.07158	10.2596	25.8941	6.1772	6.2673

Table B.7: Efficiency corrections due to OM curvature.

Wvl [nm]	OM_CORR 1	OM_CORR 2	OM_CORR 3
305	1.0	0.624462	0.509572
315	1.0	0.734092	0.463045
325	1.0	0.822933	0.532123
335	1.0	0.879081	0.651848
345	1.0	0.911915	0.757835
355	1.0	0.930156	0.835524
365	1.0	0.942225	0.887722
375	1.0	0.948235	0.917835
385	1.0	0.954443	0.937728
395	1.0	0.959908	0.951536
405	1.0	0.963204	0.959377
415	1.0	0.966523	0.964657
425	1.0	0.96812	0.967352
435	1.0	0.970813	0.970441
445	1.0	0.972259	0.972113
455	1.0	0.973348	0.973539
465	1.0	0.97492	0.975448
475	1.0	0.976332	0.976967
485	1.0	0.977582	0.978218
495	1.0	0.978789	0.979468
505	1.0	0.980006	0.98061
515	1.0	0.981137	0.981727
525	1.0	0.981866	0.982436
535	1.0	0.983254	0.983671
545	1.0	0.983691	0.983949
555	1.0	0.984979	0.984944
565	1.0	0.986401	0.985997
575	1.0	0.987783	0.986955
585	1.0	0.987829	0.986873
595	1.0	0.988211	0.987117

Appendix C

Energy reconstruction tables and programs

All probabilities necessary for calculation of energy reconstruction likelihood have to be calculated in advance. Due to the large geometrical parameter space, this is a very time-consuming step. For all parameters, the tables have been generated and linear interpolation is used to readout values between the bins. The majority of programs needed for table generation and manipulation have been custom-written [116].

Muon energy loss profiles

The muon energy loss as a function of the initial muon energy can be either calculated from muon interaction cross sections or simulated. Numerical integration turns out to be more time-consuming than propagation of a large set of muons, so the energy loss profiles (see Figure 2.6) have been simulated. Mono-energetic beams of muons were generated by `muo0` [115] and then propagated in full stochastic mode by `MUM`*. The muon data are then tabulated by `muon_profile` [116] with options specified in Table C.1.

Table C.1: Options used for `muon_profile` program.

Parameter	Value	Flag
Start of muon energy loss	vertex	`-m 0`
End of muon energy loss	600 m from vertex	`-n 600`
Stepping distance	0.5 m	`-s 0.5`
Minimum shower energy	0.5 GeV	`-E 0.5`
EM and hadronic shower separation	yes	`-S`

Light intensity tables

To generate muon-induced photon flux tables, different light sources at different depths simulated by `photonics` need to be combined. In this work, the Homogeneous Ice Model was used (see section 3.2.3) for ice description in simulation of the light distribution. Tables were generated for muon Čerenkov light and for electromagnetic and hadronic shower light. Only 1 GeV point-like showers were generated. For different shower energies, the light output was scaled linearly with energy as done in `amasim`. The light table parametrizations are given in Table C.2. Full efficiency normalization was used, so photon flux values provided by the tables were given in PE units.

Muon light tables

Muon light tables are used by minimizer to generate maximum likelihood distributions. They are generated by combining muon energy loss profiles with light intensity tables for all muon energies and geometries of trajectory with respect to the detector. The

---

*`MMC` would have been preferred, but it was unavailable at the time.

Table C.2: Binning used for photon density tables generated with `photonics`. The source depth is relative to AMANDA coordinate system origin which is at the nominal depth of 1730 m. Cubic geometry with quadratic binning was used for tracking volume description.

Variable	Unit	low bin	high bin	step
Depth	m	-350	350	20
Active volume side (x,y,z)	m	-250	250	$51^\dagger$
Delay timing window	ns	0	6000	6000

Table C.3: Binning used for generation of muon-generated photon flux tables in the detector. The depths are relative to the origin of the AMANDA coordinate system and the zenith angle is given as a direction from which a muon is arriving.

Variable	Unit	low bin	high bin	step
Energy	$\log_{10}$ GeV	1	8	0.125
Zenith angle	°	0	180	10
Depth	m	-350	350	20

tables are generated by `muon_light` program [116] which groups them into files by zenith angle. Table C.3 describes the tabulation steps used in this work.

Detector response profiles

To translate the photon flux (or equivalently $\langle NPE \rangle$ flux once OM efficiencies are applied) into an OM pulse, the table of OM responses is needed. For each given $\langle NPE \rangle$, values of $P_{\text{pulse}}(A; \langle NPE \rangle)$ are calculated by `amp_response` program [116]. The command line options used with `amp_response` are given in Table C.4.

The probabilities that a pulse will not be recorded due to the discriminator threshold, $P^i_{\text{th}}(\langle NPE \rangle)$, were calculated by `threshold_loss` program. The command line options used with `threshold_loss` are given in Table C.5.

[†] Number of bins with variable quadratic bin size distribution centered on origin.

Table C.4: Options for amplitude probability generation used with `amp_response` program.

Parameter	Value	Flag
For true photon information		
Minimum $\langle NPE \rangle$ level	10^{-5}	`-p -5`
Maximum $\langle NPE \rangle$ level	10^{5}	`-P 5`
$\langle NPE \rangle$ step	0.1 in $\log\langle NPE \rangle$	`-s 0.1`
Amplitude generation function	Measured distribution	`-a`
Probability renormalization	Peak amplitude	`-r 1`
PE saturation	No saturation	No flags (default)
Output file		`amp.asc`

For calibrated photon information		
Minimum $\langle NPE \rangle$ level	10^{-5}	`-p -5`
Maximum $\langle NPE \rangle$ level	10^{5}	`-P 5`
$\langle NPE \rangle$ step	0.1 in $\log\langle NPE \rangle$	`-s 0.1`
Amplitude generation function	Measured distribution	`-a`
Probability renormalization	Peak amplitude	`-r 1`
PE saturation	100 PE	`-S 100`
Output file		`amp_sat100.asc`

Table C.5: Options for threshold-cutoff probability generation used with `threshold_loss` program.

Parameter	Value	Flag
For calibrated photon information		
Minimum $\langle NPE \rangle$ level	10^{-5}	`-p -5`
Maximum $\langle NPE \rangle$ level	10^{5}	`-P 5`
$\langle NPE \rangle$ step	0.1 in $\log\langle NPE \rangle$	`-s 0.1`
PE saturation	100 PE	`-S 100`
Output file		`th_loss_sat100.asc`

Reconstruction minimizer options

The standard AMANDA reconstruction program `recoos` [115] was modified to act as minimizer for energy reconstruction. The major technical difference to standard AMANDA data processing that had to be applied was to remove rejected channels with `'deff -r [OM]'` before reconstruction[‡] instead of ignoring them with `'recoos -y N=[OM]'`. Table C.6 describes `recoos` command line options needed to use it for energy reconstruction. For MC data, `amasim` was used with `'DOWRPE 1'` option to provide the true photon detection information.

The muon light tables are loaded into `recoos` through a driver file which has the following format:

- Comment lines must start with `'!'`. Blank lines are ignored.
- First non-comment line must be:

  `N <number of muon light files>`
- The remaining lines must look like:

  `<muon track zenith angle> <file name>`

  The file list should come in the increasing zenith angle order. The zenith angle value given for each file corresponds to the lower edge of zenith angle bin for which the file is valid.

NB: Make sure that the computer running `recoos` has sufficient memory to load all muon light tables.

[‡] At the moment, this is the only way to mark an OM as inactive during the analysis.

Table C.6: Energy reconstruction options used with `recoos`.

Parameter	Value	Flag
True track and true photon information used		
Reconstruction type	Single muon minimization	`-r m`
Starting hypothesis	Generated track	`-p g=1`
Vertex shift	None	`-X s=n`
Minimizer	Brent's	`-m b`
Function minimized	Ped's amplitude likelihood	`-z a_pedamp`
Parametrization	Logarithmic energy	`-l logE`
Free parameters	Logarithmic energy	`-x logE`
Noise rate	300 Hz over 7μs	`-p n=300:7000`
Time window	7 μs	`-y R=-500.:6500.`
Amplitude response	No PMT saturation	`-p A=amp.asc`
Threshold effect	None	no flags (default)
Muon light tables	Standard	`-p P=<driver file>`
Detector active volume	620×135 m cylinder	`-p C=240:-240:65:70`
PE information	True, no PMT saturation	`-p N=100000`
Muon active volume	Out to 2nd most distant hit	`-p r=-2`

Reconstructed track and calibrated photon information used		
Reconstruction type	Single muon minimization	`-r m`
Starting hypothesis	Reconstructed track	`-p f=2`
Vertex shift	None	`-X s=n`
Minimizer	Brent's	`-m b`
Function minimized	Ped's amplitude likelihood	`-z a_pedamp`
Parametrization	Logarithmic energy	`-l logE`
Free parameters	Logarithmic energy	`-x logE`
Noise rate	1000 Hz over 4.5 μs	`-p n=1000:4500`
Time window	7 μs	`-y R=-500.:6500.`
Amplitude response	100 PE PMT saturation	`-p A=amp_sat100.asc`
Threshold effect	100 PE PMT saturation	`-p T=th_loss_sat100.asc`
Muon light tables	Standard	`-p P=<driver file>`
Detector active volume	620×135 m cylinder	`-p C=240:-240:65:70`
PE information	Calibrated PE	no flags (default)
Muon active volume	Out to 2nd most distant hit	`-p r=-2`